



**HAL**  
open science

# Tailoring magneto-optical properties of magnetoplasmonic systems through nanostructuring

Xiaokun Ding

► **To cite this version:**

Xiaokun Ding. Tailoring magneto-optical properties of magnetoplasmonic systems through nanostructuring. Optics / Photonics. Ecole Centrale de Lille, 2017. English. NNT : 2017ECLI0001 . tel-01688346

**HAL Id: tel-01688346**

**<https://theses.hal.science/tel-01688346>**

Submitted on 19 Jan 2018

**HAL** is a multi-disciplinary open access archive for the deposit and dissemination of scientific research documents, whether they are published or not. The documents may come from teaching and research institutions in France or abroad, or from public or private research centers.

L'archive ouverte pluridisciplinaire **HAL**, est destinée au dépôt et à la diffusion de documents scientifiques de niveau recherche, publiés ou non, émanant des établissements d'enseignement et de recherche français ou étrangers, des laboratoires publics ou privés.

N° d'ordre : 314

CENTRALE LILLE

## THESE

Présentée en vue d'obtenir le grade de

## DOCTEUR

En

**Spécialité : Micro et Nanotechnologies, Acoustique et  
Télécommunications**

Par

**Xiaokun DING**

DOCTORAT DELIVRE PAR CENTRALE LILLE

Titre de la thèse :

**Contrôle des propriétés magnéto-optiques de  
systèmes magnétoplasmoniques grâce à la nanostructuration**

**Tailoring magneto-optical properties of  
magnetoplasmonic systems through nanostructuration**

Soutenue le 24 Janvier 2017 devant le jury d'examen :

<b>Président</b>	Me. Sabine SZUNERITS	Professeur à l'Université de Lille
<b>Rapporteur</b>	Me. Nora DEMPSEY	Directrice de Recherche, Institut Louis Néel
<b>Rapporteur</b>	M. Jérôme PLAIN	Professeur à l'Université de Technologie de Troyes
<b>Examineur</b>	M. Serge RAVAINÉ	Professeur à l'Université de Bordeaux
<b>Examineur</b>	M. Jean JURASZEK	Maître de Conférences-HDR, Université de Rouen
<b>Examineur</b>	M. Yujun SONG	Professeur à USTB University
<b>Encadrant</b>	M. Nicolas TIERCELIN	Chargé de Recherche, CNRS-IEMN
<b>Directeur de thèse</b>	M. Philippe PERNOD	Professeur à Centrale Lille
<b>Invité</b>	M. Vladimir PREOBRAZHENSKY	Professeur Emérite

Thèse préparée au Laboratoire International Associé LICS/LEMAC  
Institut d'Electronique de Microélectronique et de Nanotechnologies  
(IEMN, UMR CNRS 8520, France)

Ecole Doctorale SPI 072 (Lille I, Lille III, Artois, ULCO, UVHC, Centrale Lille)





# Acknowledgments

This thesis was written as a part of my doctoral studies and researches in the AIMAN-FILMS group at the Institut d'Electronique, de Microélectronique et de Nanotechnologie (IEMN). This work is supported by a collaboration between Centrale Lille and the China Scholarship Council (CSC), and financed by CSC.

I would like first to give my sincere thanks to my supervisor Philippe PERNOD. Thank you for offering me this wonderful opportunity to work in such a great laboratory, and providing the instructions to help me grow. Also, my special thanks to Nicolas TIERCELIN for always finding time to give me guidance, sharing the ideas with me, helping me with the experiments and everything. Thank you for not giving me up and leading me to where I am.

I am also genuinely grateful to all the committee members who have accepted to evaluate my work: Nora DEMPSEY, Jérôme PLAIN, Sabine SZUNERITS, Serge RAVAINÉ, Jean JURASZEK, Yujun SONG and Vladimir PREOBRAZHENSKY.

Many thanks to the people who taught me and helped me a lot during my research and study: Jean-Claude GERBEDOEN for helping me with the SEM, 3D-printing and clean room skills, Alexey KLIMOV for the Kerr effects, Yves DEBLOCK and Elizabeth GALOPIN for the ellipsometry, Annie FATTORINI and Marc DEWITTE for the metalization, François VAURETTE for the E-beam lithography, David GUERIN for the UV-vis spectrometer, Yannick DUSCH for the ideas and suggestions; also deep sense of gratitude towards Patrik ASPERMAIR for the MOSPR measurements, Alexandre BARRAS for the RfS measurements, Yannick COFFINIER for the gold nanoparticles.

And heartfelt thanks to my families who have always been incredibly supportive to me and believed in me.



# Contents

Acknowledgments . . . . .	i
Contents . . . . .	iii
<b>Résumé en français</b>	<b>1</b>
<b>Introduction</b>	<b>7</b>
<b>1 Plasmonic, magnetoplasmonic and nanoporous structures for biosensing applications</b>	<b>9</b>
1.1 Fundamentals of plasmonics and applications for biosensing . . . . .	9
1.1.1 Introduction to surface plasmons . . . . .	9
1.1.2 SPPs at metal-dielectric interface . . . . .	10
1.1.3 LSPs in nanoparticles . . . . .	17
1.2 Magnetoplasmonic structures to enhance the sensing . . . . .	23
1.2.1 Magneto-optical Kerr effect (MOKE) . . . . .	24
1.2.2 MOSPR sensors based on magnetoplasmonic thin films . . . . .	25
1.2.3 MOLSPR sensors based on magnetoplasmonic nanodots . . . . .	31
1.3 RfS in nanoporous structures . . . . .	35
1.4 Conclusion . . . . .	37
<b>2 Thin-film magnetoplasmonic sensors with tailored magnetic properties</b>	<b>39</b>
2.1 Nanostructured magnetic layers . . . . .	40
2.1.1 Introduction . . . . .	40
2.1.2 Multilayers with controlled uni-axial anisotropy . . . . .	40
2.2 Magnetoplasmonic sensors . . . . .	40
2.2.1 Calculations for thicknesses of individual layers . . . . .	42
2.2.2 Sample realization . . . . .	43
2.2.3 Magnetic characterization . . . . .	45
2.2.4 Magneto-optical SPR (MOSPR) measurements . . . . .	47

2.2.4.1	Co sensor . . . . .	48
2.2.4.2	Multi-3 sensor . . . . .	51
2.2.4.3	Multi-5 sensor . . . . .	53
2.2.4.4	Discussion . . . . .	53
2.3	Conclusion . . . . .	59
<b>3</b>	<b>Plasmonic gold nanoparticles combined with continuous magnetic thin films</b>	<b>61</b>
3.1	Fabrication of Au nanoparticles . . . . .	62
3.2	Plasmonic properties of Au nanoparticles . . . . .	62
3.3	Magnetoplasmonic structures based on Au NPs . . . . .	64
3.3.1	Protection test . . . . .	64
3.3.2	Direct deposition of magnetic layers . . . . .	65
3.3.3	Dielectric spacer . . . . .	66
3.3.4	Thickness effects of magnetic layers . . . . .	68
3.4	Conclusion . . . . .	69
<b>4</b>	<b>Nanoporous alumina matrix coated by magnetoplasmonic layers</b>	<b>71</b>
4.1	Introduction . . . . .	71
4.2	Fabrication and structures . . . . .	72
4.3	Characterization of samples . . . . .	73
4.3.1	VSM measurements . . . . .	73
4.3.2	Reflectivity measurements . . . . .	75
4.3.3	Kerr effect measurements . . . . .	79
4.4	Conclusion . . . . .	82
	<b>Conclusion</b>	<b>85</b>
	<b>Bibliography</b>	<b>87</b>

# Résumé en français

Ce travail de thèse porte sur le contrôle des propriétés de trois systèmes magnéto-plasmoniques faisant intervenir différents types de nanostructuration. Ces structures sont basées respectivement sur la Propagation de Plasmons de Surface (SPP), les Plasmons de Surface Localisés (LSP) et la spectroscopie d'interférences en réflexion (RfS). La manipulation des propriétés magnéto-optiques (MO) pour une utilisation dans les biocapteurs et pour l'amélioration de la sensibilité est discutée.

## I - Introduction

Les plasmons de surface (SPs) ont fasciné les humains depuis des siècles. Les couleurs merveilleuses et brillantes des fenêtres des cathédrales médiévales ont été obtenues par des colloïdes de petites particules métalliques. Cela peut être expliqué par la science moderne: L'excitation des modes d'oscillation plasmon dans les nanoparticules de métal crée des bandes d'absorption et produit des couleurs uniques dans la lumière transmise. Plus précisément, les SPs sont des ondes électromagnétiques couplées aux oscillations collectives des charges libres superficielles dans une interface entre deux milieux possédant des perméabilités de signe opposé, typiquement un diélectrique et un métal. Les plasmons de surface peuvent confiner le champ électromagnétique dans des structures nanométriques telles que des films minces, des nanoparticules, des cylindres, ce qui les rend aptes au développement de dispositifs nanophotoniques. Les dispositifs de détection optique sans marqueurs ont largement utilisé des plasmons de surface en raison de leur grande sensibilité à l'indice de réfraction du milieu diélectrique. Le magnétisme a ensuite été introduit dans des structures plasmoniques non seulement pour contrôler activement les propriétés des plasmons, mais également pour permettre la modification de la réponse magnéto-optique. Ainsi, le champ de la magnéto-plasmonique a émergé pour traiter la combinaison de la résonance plasmonique et des propriétés magnétiques. Dans les structures magnéto-plasmoniques constituées de métaux nobles et de matériaux ferromagnétiques, les propriétés plasmoniques et magnétiques sont couplées, ce qui permet d'une part, de moduler les propriétés plasmoniques par l'application d'un champ magnétique ou d'autre part, d'amplifier l'activité magnéto-optique par l'excitation de plasmon. De nombreux types de systèmes magnéto-

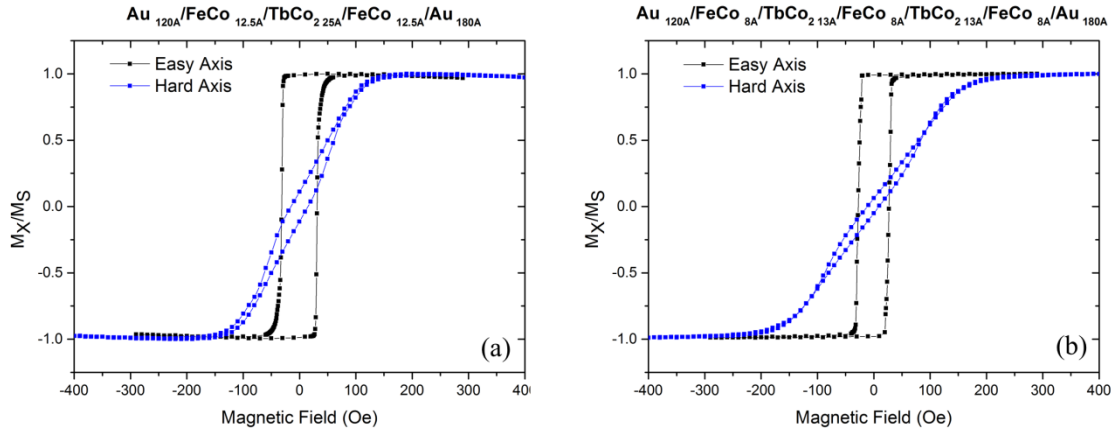


Figure 1: Aimantation des structures magnéto-plasmoniques avec couches magnétiques nanostructurées FeCo-TbCo<sub>2</sub>-FeCo et FeCo-TbCo<sub>2</sub>-FeCo-TbCo<sub>2</sub>-FeCo.

plasmoniques basés sur ces effets ont été proposés afin par exemple, de surpasser la sensibilité des capteurs à base de SP, mais les possibilités sont encore vastes. Dans une autre approche, les structures de type RIFS basées sur l'oxyde d'aluminium anodisé (AAO) sont également très sensibles au changement des conditions environnantes et sont utilisées comme bio-capteurs. Dans ce contexte général, j'ai étudié dans le cadre de cette thèse trois systèmes magnéto-plasmoniques différents basés sur les SPP, LSP et RIFS respectivement, avec de nouveaux types de matériaux nanostructurés. Leurs propriétés magnéto-plasmoniques ont été caractérisées leurs applications dans le domaine de la bio-détection ont été discutées.

## II - Capteurs magnéto-plasmoniques SPP avec propriétés magnétiques contrôlées.

Dans cette structure magnéto-plasmoniques, on utilise des couches magnétiques nanostructurées pour remplacer la couche de Co dans un système tri-couche classique Au/Co/Au. Les couches magnétiques nanostructurées sont initialement développées dans le groupe AIMAN-FILMS à l'IEMN. Ces matériaux sont composés d'un empilement de couches de FeCo et TbCo<sub>2</sub>. Les multicouches sont déposées par pulvérisation sous champ magnétique, induisant une anisotropie uni-axiale magnétique contrôlée. Dans les deux structures magnéto-plasmoniques réalisées (Au / FeCo-TbCo<sub>2</sub>-FeCo / Au et Au / FeCo-TbCo<sub>2</sub>-FeCo-TbCo<sub>2</sub>-FeCo / Au), l'anisotropie uni-axiale magnétique est présente, comme le montre la Fig. 1

Dans ces structures, une résonance de plasmon de surface (SPR) est clairement observée dans les courbes d'absorption de l'intensité lumineuse d'un faisceau laser dans une configuration de type kretschmann. Ensuite, les effets du champ magnétique sur les propriétés SPR sont clairement démontrés dans les courbes de suivi de l'angle du minimum d'absorption, représentées sur la Fig. 2. Le

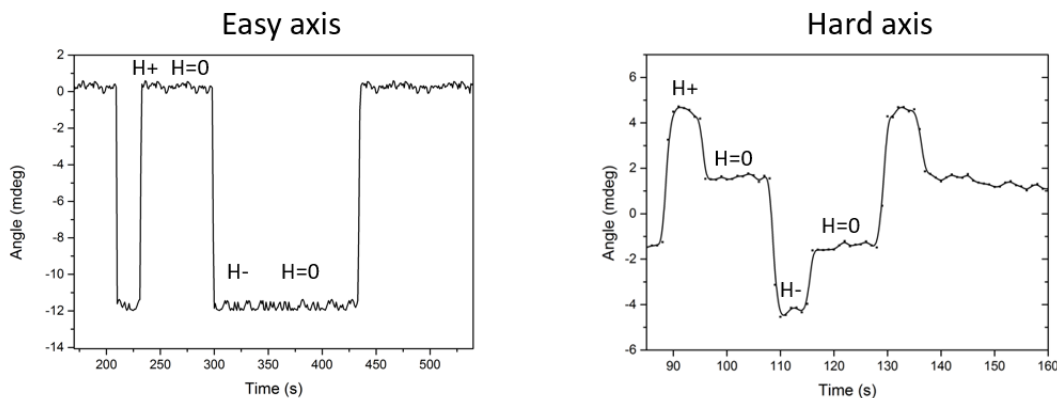


Figure 2: Evolution de l'angle d'absorption maximum pour différentes valeurs de champ magnétique appliqué dans le système Au / FeCo-TbCo<sub>2</sub>-FeCo / Au.

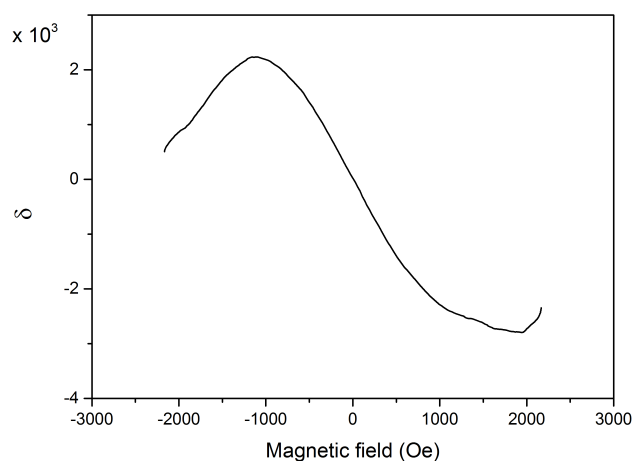


Figure 3: Courbe  $\delta$  pour le système Au / FeCo-TbCo<sub>2</sub>-FeCo / Au.

long de l'axe facile, lorsque le champ magnétique change, il y a deux valeurs d'angle SPR en raison des deux directions possibles d'aimantation. En revanche, le long de l'axe difficile il y a plusieurs valeurs d'angles SPR supplémentaires qui reflètent l'aimantation rémanente lorsque le champ magnétique est enlevé. Les propriétés anisotropes uni-axiales des multicouches magnétiques se retrouvent donc bien dans les propriétés plasmoniques sous un champ magnétique externe. En tirant parti de la formule

$$\delta = \frac{R(H+) - R(H-)}{R(H=0)} \quad (1)$$

la courbe  $\delta$  est obtenue (Fig. 3) et peut être utilisée pour améliorer la sensibilité.

Une situation similaire existe pour la structure '5-couches' Au/FeCo-TbCo<sub>2</sub>-FeCo-TbCo<sub>2</sub>-FeCo/Au.

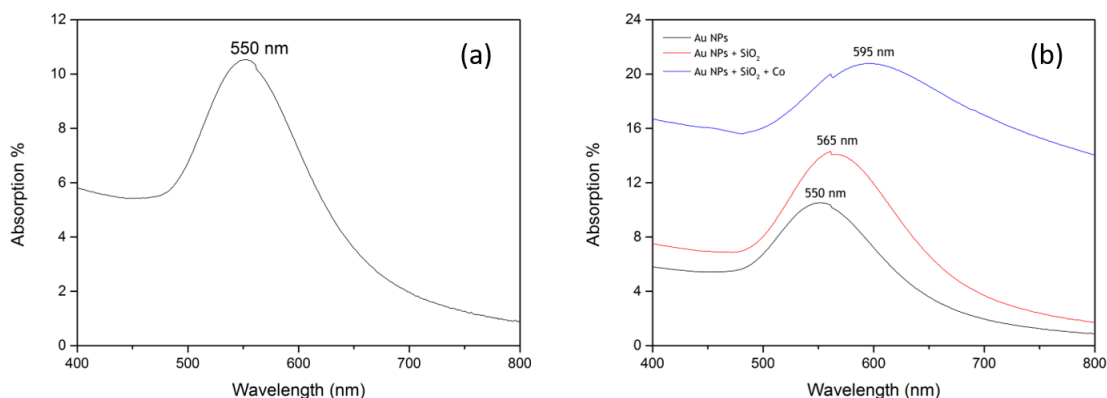


Figure 4: Spectres d'absorption UV-Vis : (a) Nanoparticules d'or seules. (b) nanoparticules Au (NPsAu), NPsAu avec SiO<sub>2</sub>, NPsAu avec SiO<sub>2</sub> et couche de cobalt.

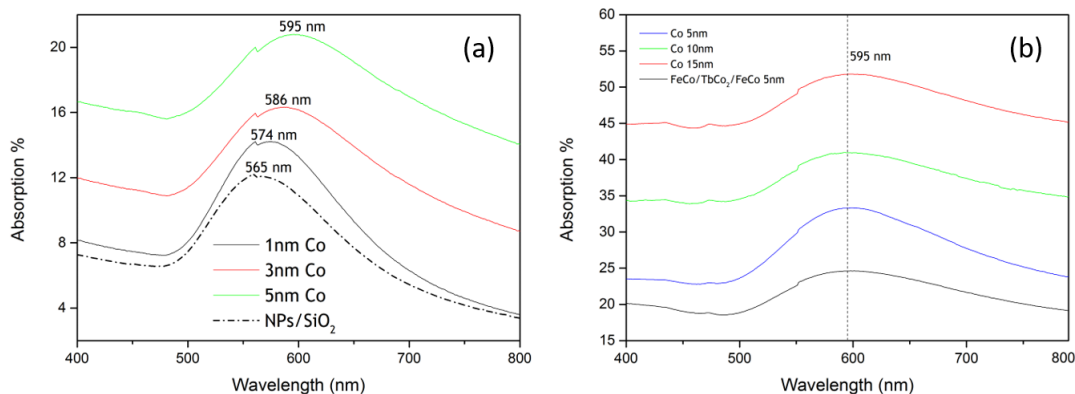


Figure 5: Spectres d'absorption UV-Vis : (a) NPsAu + Couche de Co d'épaisseur 1, 3 et 5 nm. (b) NPsAu + Couche de Co d'épaisseur 5, 10 et 15 nm.

### III - Nanoparticules d'or plasmoniques LSP combinées avec des films minces magnétiques continus

Il s'agit d'un type de structure magnéto-plasmonique qui est facile et bon marché à fabriquer, par rapport aux réseaux de nanodisques Ni ou Au/Co/Au existants. Les nanoparticules d'Or sont obtenues en effectuant un recuit thermique rapide sur le film mince d'Or. La résonance LSP des nanoparticules d'Or est illustrée sur la Fig. 4(a). Les films magnétiques sont ensuite déposés par pulvérisation cathodique sur ces nanoparticules. Avant le dépôt de films magnétiques, une couche tampon isolante de SiO<sub>2</sub> s'avère nécessaire pour maintenir le LSPR (Fig. 4(b)). Les propriétés LSPR des structures dépendent de l'épaisseur des films magnétiques (Fig. 5).

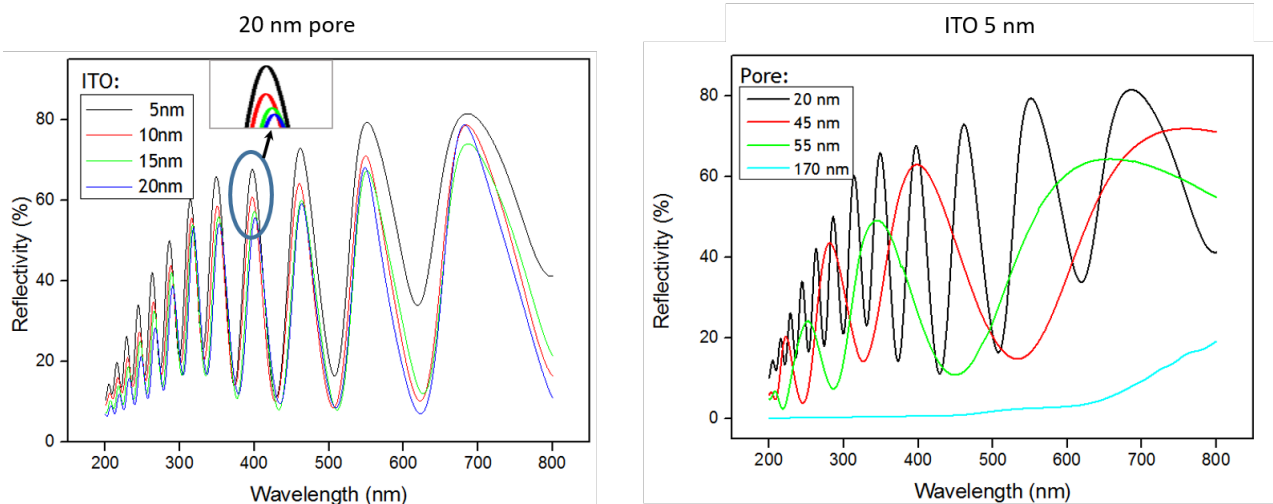


Figure 6: Signaux RfS: (a) Taille de pores constante avec épaisseur de couche ITO variable. (b) Epaisseur d'ITO constante et taille de pores variable.

#### IV - Matrice d'alumine nanoporeuse recouverte de couches magnéto-plasmoniques (type RfS)

Cette structure est fabriquée en déposant des multicouches magnéto-plasmoniques sur un substrat AAO (Anodic Aluminium Oxide) nanoporeux. Des échantillons avec des diamètres de pores différents sont préparés. On étudie les propriétés magnétiques apportées par la couche de CoFeB dans cette structure et on montre que la structure est ferromagnétique et que le ferromagnétisme diminue lentement avec le temps. Les propriétés optiques sont caractérisées par la mesure des spectres de réflectivité (signal RfS). Les profils (nombre et décalage des franges) du signal RfS dépendent de la géométrie (longueur et diamètre) des pores (Fig. 6). Cela permet d'accorder la structure pour produire des signaux RfS optimaux avec des franges de haute intensité et d'espacement approprié, ce qui est utile pour améliorer les performances en détection. Des mesures par effet Kerr magnéto-optique (MOKE) ont également été effectuées, et il existe une inversion du signe des boucles Kerr (Fig. 7). L'inversion, qui est analogue à celle observée dans des nano-plots magnétiques structurellement complémentaires, est déterminée par la taille des nanopores. Cet effet pourra servir à la conception de dispositifs de détection avec une grande sensibilité et une valeur très haute de leur figure de mérite.

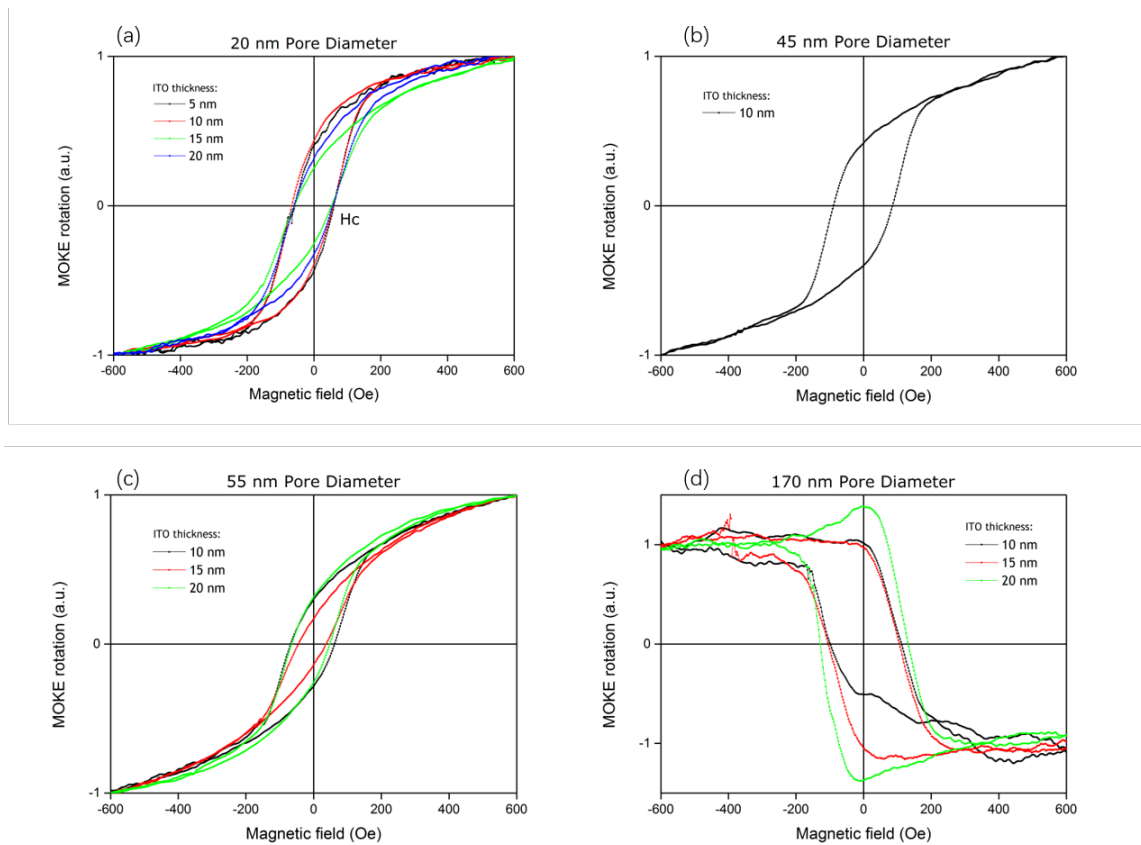


Figure 7: Cycles d'aimantation mesurés par effet Kerr Magnéto-optique des échantillons nanoporeux Ag / ITO / CoFeB / ITO / Ag, pour différents diamètres de pores et épaisseurs d'ITO de la couche magnétoplasmonique.

# Introduction

Surface plasmons (SPs) have fascinated humans for centuries. The wonderful brilliant colors on the windows of medieval cathedrals were achieved by the colloids of gold particles. This can be explained by modern science that the excitation of plasmon oscillation modes in metal nanoparticles creates absorption bands and produces unique colors in the transmitted light. To be specific, SPs are electromagnetic waves coupled to the collective oscillations of the surface free charges in an interface between two media with permittivities with opposite sign, typically a dielectric and a metal [1]. Surface plasmons can confine the electromagnetic field in nanoscale structures, such as thin films, nanoparticles, cylinders, which makes them suitable for the development of nanophotonic devices

Label-free optical sensing devices have widely employed surface plasmons due to their high sensitivity to the refractive index of the dielectric surroundings. Magnetism has later been introduced into plasmonic structures not only to actively control plasmon properties, but also to allow the modification of magneto-optical response. Thus the field of magnetoplasmonics emerged to deal with the combination of plasmonic resonance and magnetic properties. In magnetoplasmonic structures consisting of noble metals and ferromagnets, plasmonic and magnetic properties are intertwined, allowing plasmonic properties to be modulated by the application of a magnetic field, or magneto-optical activity to be largely enhanced by plasmon excitation. Many kinds of magnetoplasmonic systems based on these effects have been proposed to find their potentials for sensing applications in order to surpass the sensitivity of SPs-based sensors, but the possibilities are vast. Motivated by this, we will study in this thesis three different magnetoplasmonic systems with pioneering nanostructuring to investigate their interactive magnetic-plasmonic properties, and explore their applications for sensing. Therefore this dissertation will be organized as follows:

In the first chapter we will first present three physical principles of fundamental techniques that are used in refractive index sensing:

- SPPs: Surface Plasmon Polaritons (SPPs)

- LSPs: Localized Surface Plasmons (LSPs)
- RIfS: Reflective Interference Spectroscopy (RIfS)

Then we will see how magnetic materials were introduced in various magnetoplasmonic structures to enhance their magneto-optical activity, and how it can be exploited to define new mechanism to improve their sensing performance. This analysis will serve as a basis to see how targeted magnetic materials and structures could lead to further improvement. The following chapters will then describe the structures that were studied for the three categories (SPPs, LSPs, and RIfS).

In the second chapter, a SPP magnetoplasmonic thin-film structure of noble metal/magnetic layer/noble metal will be investigated. It is a structure with propagating plasmons, which can be tuned by an applied magnetic field. In this particular device, the conventional Cobalt used as the magnetic layer will be replaced by a nanostructured multilayer exhibiting uni-axial anisotropy. Two kinds of multilayers will be compared, also with a Cobalt based device serving as a reference. The effects of the magnetic uni-axial anisotropy of the nanostructured magnetic layers on the plasmonic properties will be investigated and discussed.

In the third chapter, a LSP magnetoplasmonic structure is proposed by mixing noble metal nanoparticles and continuous magnetic layers, which is a structure with localized plasmons. We will study the importance of a dielectric spacer in between the two components, and the effect of magnetic layers on the plasmonic resonance will also be investigated.

In the fourth chapter, we will study a hybrid RIfS structure by depositing magnetoplasmonic multilayers onto nanoporous anodic aluminum oxide substrates. Samples will be prepared on substrates with different pore diameters. We will investigate the magnetic properties of the structure. Optical properties will be assessed by measuring the reflectivity spectra that can be controlled by the pore structure. Magneto-optical properties will also be studied to see how the pore size and plasmonic resonance can have an effect on the magneto-optical response, and how this can be exploited for sensing applications.

## **Chapter 1**

# **Plasmonic, magnetoplasmonic and nanoporous structures for biosensing applications**

In this chapter, I will first present three kinds of principles that are widely used in sensing the changes in refractive index, namely the surface plasmon polaritons (SPPs), localized surface plasmons (LSPs) and reflective interference spectroscopy (RIS). The physical origins of the three phenomena and their sensing mechanisms will be explained in details. Then we will see how magnetic materials or effects can be introduced to enhance their magneto-optical properties and sensing performance. At the end of this chapter, I will introduce the work that has been done in this dissertation on three nanostructured magnetoplasmonic devices with non-conventional magnetic materials and layers : thin-film SPP-based structure with nanostructured magnetic layers, nanodots LSP-based structure with nanostructured magnetic layers, and magnetoplasmonic multilayers on top of nanoporous substrates.

### **1.1 Fundamentals of plasmonics and applications for biosensing**

#### **1.1.1 Introduction to surface plasmons**

Ever since the 1957 when Rufus Ritchie [2] first predicted the existence of coherent electron oscillations bound to the surface of a conductor, i.e., surface plasmons (SPs), extensive efforts have been devoted to the study of this phenomenon . Surface plasmons are electromagnetic waves interacting with collective electron oscillations that exist at the interface between two materials with permittivity

of opposite signs across the interface, usually a metal-dielectric interface [3]. They are strongly localized at the interface and exist in various metallic structures, such as nanoparticles, nanowires, thin films, etc. The surface plasmons can be categorized into two main types: surface plasmon polaritons (SPPs) or propagating surface plasmons for planar interfaces; and localized surface plasmons (LSPs) for structures whose dimensions are on the order of or smaller than the excitation wavelength.

Similar to photonics, information transfer in nanoscale structures by means of surface plasmons is referred to surface plasmon-based photonics, or *plasmonics*. The plasmonics play a remarkable role in the optical response of nanoscale metallic structures, usually noble metals. Especially until strong recent development of nanotechnology, we are more capable of controlling electromagnetic fields in these nanoscale structures. This particular light-matter interaction has enabled various applications including nanoscale optical devices such as waveguides, modulators and isolators [4], surfaced-enhanced spectroscopies [5–7], optical storage, and plasmonic nanolithography [8–10]. Among all the applications, biological and chemical sensing [11] is one of the most developed and still being intensely investigated due to its advantage of label-free, reduced interference and real-time monitoring performance [12]. In this section, introductory physics on the main two types of plasmonics as well as their corresponding sensing principles will be presented.

### 1.1.2 SPPs at metal-dielectric interface

Surface plasmon polaritons are visible or infrared frequency electromagnetic waves propagating along a conductor-dielectric interface in much the same way that light is guided by an optical fiber. These surface waves are a result of the coupling of incident electromagnetic field to oscillations of the conductor's electron plasma bound to the material surface. SPPs have shorter wavelength than the incident light (photons), and are strongly localized to the surface. Along the interface SPPs propagate until its energy runs out due to the absorption of the metal, while perpendicular to the interface they exponentially decay away from the interface.

#### Dispersion relation

The most basic model sustaining SPPs consists of a planar interface at  $z = 0$  (Fig. 1.1) between two semi-infinite nonmagnetic media: a dielectric half space ( $z > 0$ ) with positive real dielectric constant  $\epsilon_1$  and a metallic half space ( $z < 0$ ) described by a dielectric function  $\epsilon_2$  (frequency-dependent). The requirement of metallic character implies that  $\text{Re}[\epsilon_2] < 0$ , which is met at frequencies below the bulk plasmon frequency  $\omega_p$ . We will try to find the propagating wave solutions confined to the interface, i.e. with evanescent decay in the perpendicular  $z$ -direction.

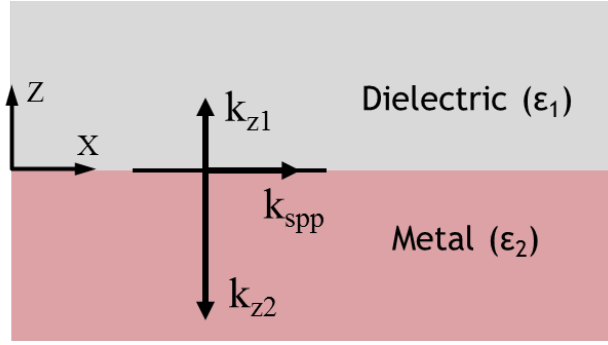


Figure 1.1: Geometry for SPP propagation at a single interface between a metal and a dielectric.

The full set of Maxwell's equations in the absence of external charge and current densities can be expressed as follows:

$$\begin{aligned} \nabla \times \mathbf{H}_j &= \epsilon_j \frac{1}{c} \frac{\partial}{\partial t} \mathbf{E}_j & \nabla \cdot \mathbf{H}_j &= 0 \\ \nabla \times \mathbf{E}_j &= -\frac{1}{c} \frac{\partial}{\partial t} \mathbf{H}_j & \nabla \cdot (\epsilon_j \mathbf{E}_j) &= 0 \end{aligned} \quad (1.1)$$

where the subscript  $j$  is used to denote field in the media:  $j = 1$  at  $z > 0$ , and  $j = 2$  at  $z < 0$ . Solutions of Eq. (1.1) can generally be categorized into TE and TM electromagnetic modes, being the electric field  $\mathbf{E}$  and the magnetic field  $\mathbf{H}$  parallel to the interface, respectively. It is noteworthy that if an electromagnetic wave is formed propagating along an ideal interface, there must necessarily be a component of the electric field perpendicular to the surface. Thus, surface modes of TE polarization (whose electric field  $\mathbf{E}$  is parallel to the interface) do not exist [13]. Therefore, we explore the conditions under which the TM mode may propagate along the interface ( $z = 0$ ), with the electric field decaying into dielectric space and metallic space. Supposing the  $x$ -axis is the propagating direction, we write:

$$\mathbf{E}_j = (E_{j_x}, 0, E_{j_z}) e^{-\kappa_j |z|} e^{i(k_j x - \omega t)} \quad (1.2)$$

and

$$\mathbf{H}_j = (0, E_{j_y}, 0) e^{-\kappa_j |z|} e^{i(k_j x - \omega t)} \quad (1.3)$$

where  $k_j$  represents the magnitude of a wave vector parallel to the surface, i.e.,  $k_j = k_{spp}$ , while  $\kappa_j = k_{zj}$  ( $j = 1, 2$ ) is the component of the wave vector perpendicular to the interface (Fig. 1.1). Putting equations (1.2) and (1.3) into equation (1.1), we obtain:

$$\begin{aligned} i\kappa_1 H_{1_y} &= -\frac{\omega}{c} \epsilon_1 E_{1_x} \\ i\kappa_2 H_{2_y} &= +\frac{\omega}{c} \epsilon_2 E_{2_x} \end{aligned} \quad (1.4)$$

and

$$\kappa_j = \sqrt{k_j^2 - \epsilon_j \frac{\omega^2}{c^2}} \quad (1.5)$$

The continuity of  $H_{j_y}$  and  $E_{j_x}$  (component of the electric and magnetic fields parallel to the surface) is required by the boundary conditions. Solving equations (1.4) and (1.5), one will get:

$$\begin{aligned} \frac{\kappa_1}{\varepsilon_1} H_{1_y} + \frac{\kappa_2}{\varepsilon_2} H_{2_y} &= 0 \\ H_{1_y} - H_{2_y} &= 0 \end{aligned} \quad (1.6)$$

The solution of the equation (1.6) is

$$\frac{\varepsilon_1}{\kappa_1} + \frac{\varepsilon_2}{\kappa_2} = 0 \quad (1.7)$$

which is the surface plasmon condition. The boundary conditions also follow the continuity of the 2D wave vector  $\mathbf{k}$  entering equation (1.5), i.e.  $k_1 = k_2 = k_{spp}$ . Hence, combining the equations (1.5) and (1.7), we arrive at the central result of this section, the dispersion relation of SPPs propagating at the interface between the two half spaces:

$$k_{spp} = k_0 \sqrt{\frac{\varepsilon_1 \varepsilon_2}{\varepsilon_1 + \varepsilon_2}} \quad (1.8)$$

where  $k_0 = \omega/c$  is the wave vector of light propagating in free space. This dispersion relation is valid for both real and complex  $\varepsilon_2$ , i.e. for metals without and with attenuation.

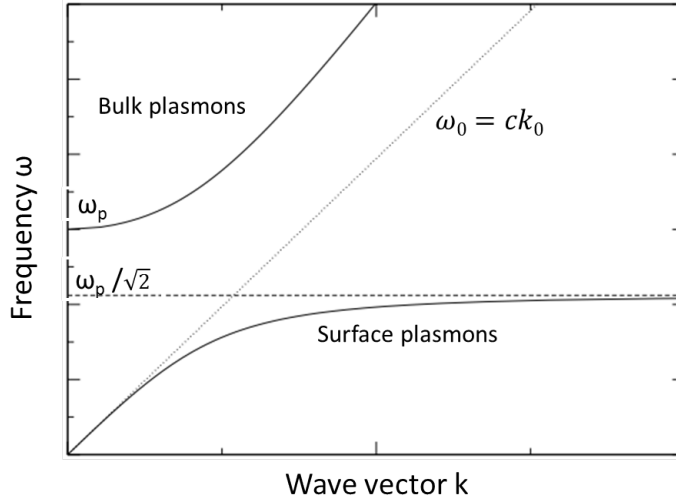


Figure 1.2: Dispersion relation of bulk plasmons (upper solid line) and SPPs (lower solid line), together with the light line in air (dotted line). The asymptote represents the surface plasma frequency  $\omega_{sp}$ .

The properties of SPPs can now be examined by taking a closer look at this dispersion relation which is plotted in Fig. 1.2, along with those of bulk plasmons and free space. The dispersion relation curve of SPPs is shown for an interface of air ( $\varepsilon_1 = 1$ ) and undamped metal whose dielectric function is described by Drude model of free electron plasma:

$$\varepsilon(\omega) = 1 - \frac{\omega_p^2}{\omega^2} \quad (1.9)$$

where  $\omega_p^2 = \frac{ne^2}{\epsilon_0 m}$  is the plasma frequency of the free electron gas. Due to their bound nature, the SPPs curve lies to the right of the light line  $\omega_0 = ck_0$ . At small wave vectors corresponding to low frequencies, the SPPs behave like a photon; in the regime of large wave vectors, the frequency of the SPPs reach an asymptotic limit called *surface plasmon frequency*

$$\omega_{sp} = \frac{\omega_p}{\sqrt{1 + \epsilon_1}} \quad (1.10)$$

In the case of air, it simplifies to  $\omega_{sp} = \omega_p / \sqrt{2}$

The discussions above of Fig. 1.2 are based on the assumption of an ideal conductor with  $\text{Im}[\epsilon_2(\omega)] = 0$ . That means the wave vector  $k_{spp}$  goes to infinity as the frequency gets close to  $\omega_{sp}$ . Excitations of the conduction electrons of real metals, however, experience damping due to both free-electron and interband transitions. Therefore,  $\epsilon_2(\omega)$  becomes complex, and also the SPP wave vector. The propagating SPPs are damped with an energy loss to the metal due to absorption, characterized by a propagation length  $L = (2\text{Im}[k_{spp}])^{-1}$ , typically between  $10\mu\text{m}$  and  $100\mu\text{m}$  in the visible spectrum, depending on the metal/dielectric configuration in question.

Likewise, the electric tails away evanescently perpendicular to the surface. At low frequencies SPP decay depth into metal can be approximated by the skin depth formula. The field falls off much more slowly in the dielectric. The amount of mode confinement perpendicular to the interface, i.e., the decay depth in two media can be expressed as [14]:

$$z_j = \frac{\lambda}{2\pi} \sqrt{\frac{\epsilon_1 + |\text{Re}[\epsilon_2]|}{\epsilon_j^2}} \quad (1.11)$$

Taking a silver/air interface as an example, when illuminated by a light at  $\lambda = 1.5\mu\text{m}$ , the SPPs have  $L \approx 1080\mu\text{m}$  and  $z_1 \approx 2.6\mu\text{m}$ . At  $\lambda = 450\text{nm}$ , however, they have  $L \approx 16\mu\text{m}$  and  $z_1 \approx 180\text{nm}$  [3]. The localization in  $z$ -direction gets smaller as the propagation length becomes shorter. Thus there is a characteristic trade-off between mode size and propagation loss in plasmonic geometries [4]. Moreover, SPPs are highly sensitive to the slight change of the surrounding environment, which renders them as quality sensors to probe inhomogeneities of the surface.

### Configurations to excite SPPs

When Powell and Swan [16, 17] first experimentally verified the existence of SPPs in 1959, high energy electrons were used to bombard a thin metallic film and launch surface plasmons. As the electrons scatter, energy is transferred into the bulk plasma. The component of the scattering vector parallel to the surface gives rise to the formation of SPPs. By tuning the energy and angle of incidence of the electrons, the wave-vector can be tuned and surface plasmons of a whole range of wavelengths

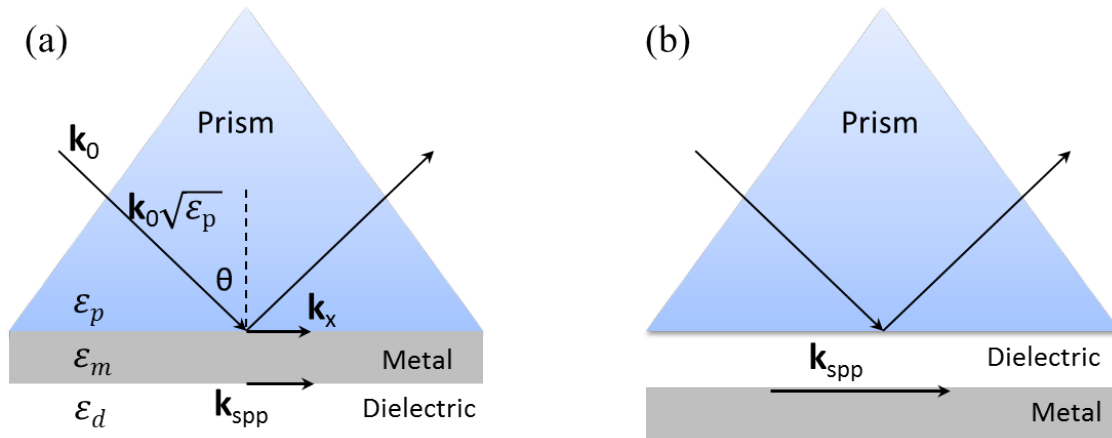


Figure 1.3: Prism coupling: Kretschmann configuration (a) and Otto configuration (b) of an attenuated total reflection (ATR) setup to excite SPPs. In both cases, the surface plasmons propagate along the metal/dielectric interface.

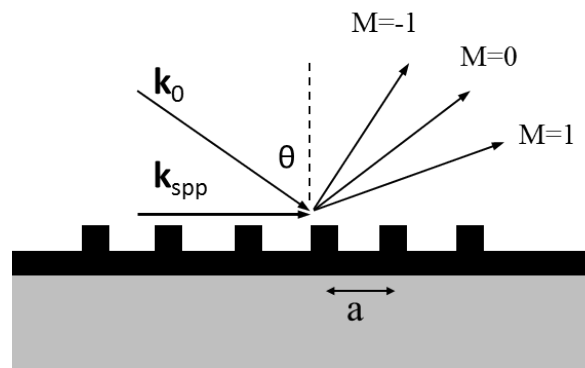


Figure 1.4: Grating coupler for excitation of SPPs. The wave vector is increased by the spatial frequency.

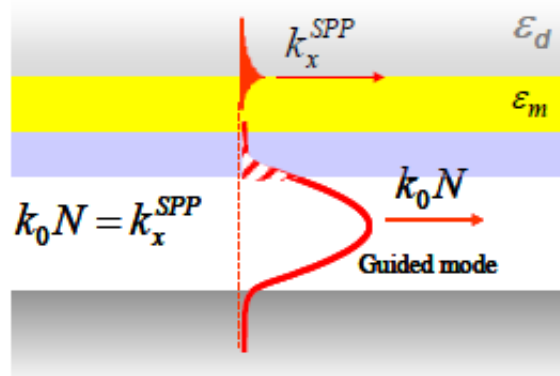


Figure 1.5: Guided light in optical fibers and waveguides. Taken from [15]

can be excited. However, due to the high energy of the electrons, they have a very large momentum and it is difficult to precisely control the coupling: even a slight spread in energy or angle will result in a very broad range of surface plasmon wavelengths being excited.

A more controllable approach to launch the SPPs is through photons. However, direct excitation of surface plasmons by free-space photons is not achievable because  $k_{spp}$  is always greater than  $k_0$  ( $k_0 < k_{spp}$ ), where  $k_0$  is the wave vector in free-space. Therefore, the projection along the interface of the momentum  $k_x = k_0 \sin\theta$  of photons striking with an angle  $\theta$  is further smaller than  $k_{spp}$  ( $k_x < k_{spp}$ ). This also can be seen from the Fig. 1.2, with the fact that the surface plasmon dispersion relation always lies to the right of the free-space dispersion curve. Nevertheless, this can be overcome by coupling of photons into SPPs using a coupling medium such as a prism to match the photon and surface plasmon wave vectors. As shown in Fig. 1.3, a prism can be positioned in contact with a thin metal film in the Kretschmann configuration [18] or very close to the metal surface in the Otto configuration [19]. This prism coupling approach allows back-side illumination through a prism with a higher permittivity  $\epsilon_p$  (higher refractive index  $n_p = \sqrt{\epsilon_p}$ ), thus the light inside the prism has a larger wave vector  $k_0\sqrt{\epsilon_p}$ . Thus, the wave vector along the metal/prism interface is sufficient to tunnel through the thin metal film to excite SPPs at the metal/dielectric interface:

$$k_x = k_0\sqrt{\epsilon_p}\sin\theta = k_{spp} \quad (1.12)$$

here assuming the dielectric to be air. Kretschmann couplers are commonly used in experiments, but are limited to very thin films such that the high- $k$  photons are able to tunnel through the film and couple to the surface plasmons on the lower-index surface.

Another approach to launching surface plasmons with light is by patterning the metal surface with a shallow grating of grooves holes with lattice constant  $a$  (Fig. 1.4), that are designed to match the wave vectors by increasing the parallel wave vector component by an amount related to the grating period

$$k_{spp} = k_0\sin\theta + gM \quad (1.13)$$

where  $g = \frac{2\pi}{a}$  is the reciprocal vector of the grating, and  $M(= \pm 1, \pm 2, \dots)$  the diffraction order. This method, although less frequently used, is desirable when direct contact with the metal surface is unnecessary, for instance for understanding the effect of surface roughness. Besides, simple isolated surface defects such as a slit, a groove or a corrugation on a planar surface serves as a coupler where free space radiation and SPs can exchange energy and hence couple.

SPPs can also be excited by other methods such as through the evanescent field of the guided light within an optical waveguide (Fig. 1.5). In this method, the SPPs are launched when the effective

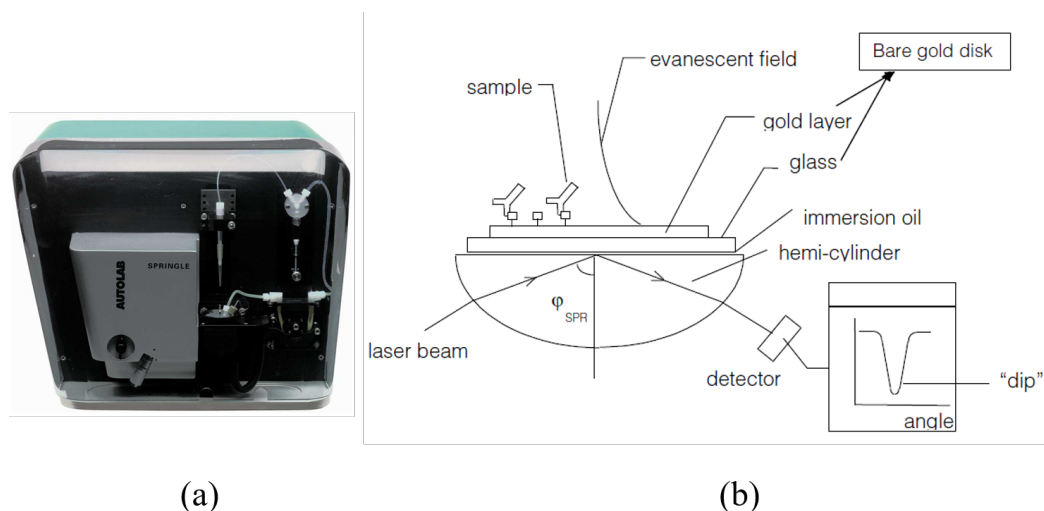


Figure 1.6: (a) The original SPR machine: Autolab SPRINGLE. (b) operation schematic of the machine: Kretschmann configuration

propagation index of the guided mode ( $N$ ) matches that of the SPPs.

### SPR sensors

Due to the strong localization of electromagnetic field in the dielectric side at the metal-prism interface, the SPR condition is very sensitive to the variations in the optical property of the dielectric. These variations can be detected by measuring the optical quantities of the system. Therefore, different detection approaches have been developed in SPR sensors based on different measured quantities:

1. Intensity interrogation by measuring the intensity of the light near the resonance [20–22],
2. Angular [23–26] or wavelength [27–29] interrogation by measuring the resonant shift  $\Delta\theta$  or  $\Delta\lambda$ ,
3. Phase [30, 31] and polarization [32–34] interrogation by measuring phase difference between the p- and s-polarization light.

The detection approaches have a significant effect on the sensitivity defined as the change of the measured signal per refractive index change.

The SPR machine at IRI (Fig. 1.6) can provide two detection methods, one is angular interrogation measuring the resonant angle shift, and the other one is intensity interrogation measuring the signal intensity (reflectivity) change at a specific angle. Let us first introduce the operating principle of the SPR machine. According to Eq. (1.12), the wave vector matching occurs at particular angle where the surface plasmon resonance is excited. The SPR is detected as a sharp dip in the reflectivity as a function of the angle of incidence, using a p-polarized laser beam with a fixed wavelength. The

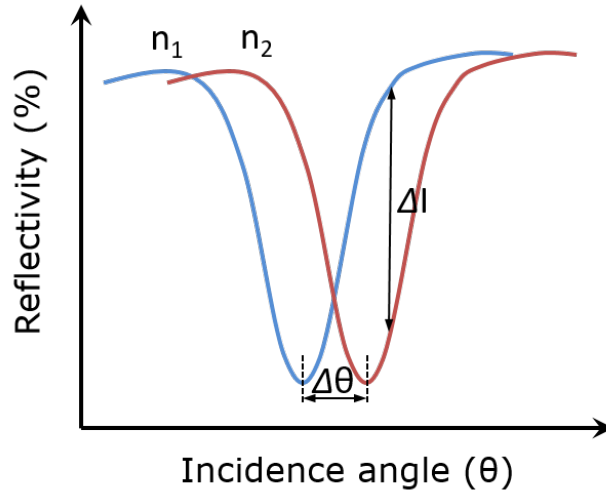


Figure 1.7: Reflectivity as a function of angle of incidence. Angular shift happens when the refractive index changes.

reflectivity minimum locates at a specific incident angle  $\theta$  where  $k_x$  matches  $k_{spp}$ . When there is a change in the dielectric environment from  $\epsilon_0$  to  $\epsilon_d$  for example, (1.12) will become

$$k_0 \sqrt{\epsilon_p} \sin \theta = \sqrt{\epsilon_d} k_{spp} \quad (1.14)$$

which means a larger incidence angle is required to meet the matching condition, resulting a red-shift on the reflectivity curve, as shown in Fig. 1.7. As the refractive index changes  $\Delta n$ , there arises a resonant angle shift  $\Delta \theta$  as in the angular interrogation, or a reflectivity change at a fixed angle as in the intensity interrogation. Thus, the sensitivity of the two methods is defined as:

$$S_{angular} = \frac{\Delta \theta}{\Delta n}, S_{intensity} = \frac{\Delta I}{\Delta n} \quad (1.15)$$

The first SPR-based biosensing application was demonstrated by Liedberg *et al* [35]. Since then the prism coupling method has been established as one of the standard techniques for label free biosensing [36].

### 1.1.3 LSPs in nanoparticles

The second fundamental excitation of plasmonics is the localized surface plasmons. Different from propagating SPPs being dispersive electromagnetic waves coupled to the electron plasma of a conductor at a dielectric interface [3], LSPs are electron density oscillations confined to metallic nanostructures (Fig. 1.8a). Excitation of LSPs by the incidence light where resonance occurs gives rise to strong light scattering, in the appearance of intense surface plasmon absorption bands (Fig. 1.8b),

and an enhancement of the local electromagnetic field (Fig. 1.8c). The resonance wavelength and intensity of SP absorption bands are dependent on the size, size distribution and shape of the nanostructures, as well as the refractive index of surrounding environment.

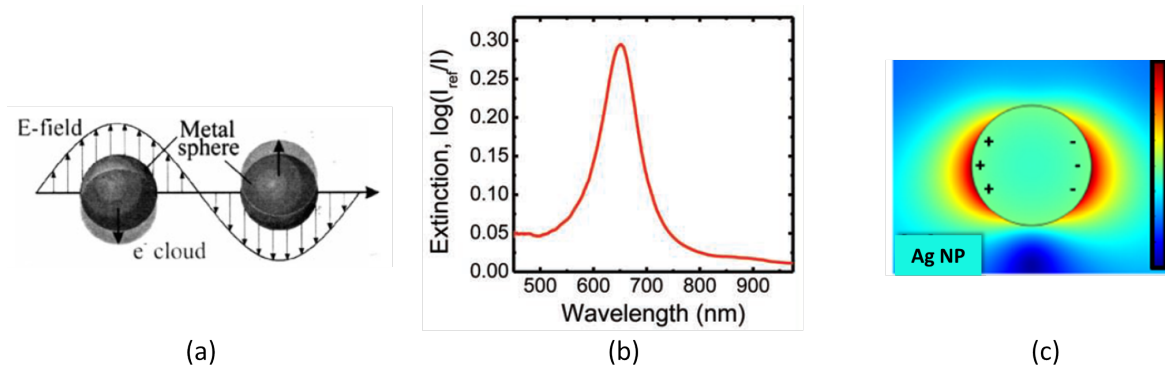


Figure 1.8: (a) Schematic of charge oscillations for a metallic nanosphere [37]. (b) Absorption spectrum of Au nanodisks (120 nm diameter, 40 nm height). (c) Calculated electric field distribution of an Ag NP with  $R = 25$  nm in air [38].

### Quasi-static approximation

The optical properties of a metallic nanoparticle (NP) are significantly distinctive from those of bulk structures. When a particle is illuminated by a plane wave, the conduction electrons are driven by the oscillating electromagnetic field. The curved surface, at the same time, causes a restoring force on the driven electrons in such a way that a resonance can appear. This leads to an enhancement of field both inside and in the near-field outside the particle. This resonance is called the localized surface plasmon resonance. Moreover, the curved surface produces another effect that LSP can be excited directly by light illumination, unlike the SPPs where the need of phase-matching should be fulfilled.

To arrive at the resonance condition, we explore the interaction of a particle with the electromagnetic field using some assumptions, which is elaborated in [3]. Here we take a brief review. Firstly, we use the quasi-static approximation assuming that the particle size  $d$  is much smaller than the light wavelength  $\lambda$ . In this way the phase of the time-varying electromagnetic field can be treated as constant over the particle volume, i.e. no spatial retardation effects. Secondly, we employ the simplest geometry for analytical treatment: the particle is a homogeneous, isotropic sphere of radius  $a$  and the surrounding environment is isotropic, non-absorbing medium with dielectric constant  $\epsilon_d$ . The metallic sphere can be described by bulk complex dielectric function  $\epsilon(\omega) = \epsilon_r(\omega) + i\epsilon_i(\omega)$ , which in the following sections we will take a simpler form  $\epsilon = \epsilon_r + i\epsilon_i$ .

We start on the ground of electrostatics solving the Laplace equation  $\nabla^2\Phi = 0$  for the potential,

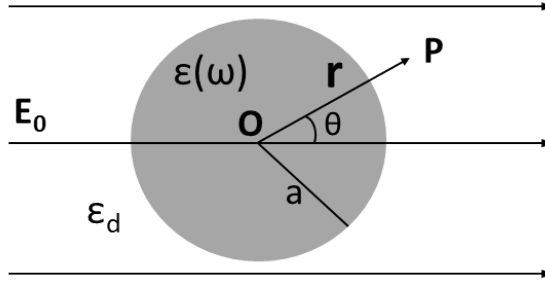


Figure 1.9: A homogeneous, isotropic sphere immersed in an isotropic, non-absorbing ambient with an electrostatic field.

then we will be able to obtain the electric field distribution via  $\mathbf{E} = -\nabla\Phi$ . The general solutions for the potentials inside and outside the sphere are

$$\Phi_{\text{in}} = -\frac{3\varepsilon_d}{\varepsilon + 2\varepsilon_d} |\mathbf{E}_0| r \cos\theta \quad (1.16a)$$

$$\Phi_{\text{out}} = -|\mathbf{E}_0| r \cos\theta + \frac{\varepsilon - \varepsilon_d}{\varepsilon + 2\varepsilon_d} |\mathbf{E}_0| a^3 \frac{\cos\theta}{r^2} \quad (1.16b)$$

being  $\theta$  the angle between the position vector  $\mathbf{r}$  at point P and the electric field  $\mathbf{E}_0$  (Fig. 1.9).  $\Phi_{\text{out}}$  can be interpreted to the superposition of the external field and the field of a dipole located at the particle center. By use of the dipole moment  $\mathbf{p}$  we rewrite  $\Phi_{\text{out}}$  as

$$\Phi_{\text{out}} = -|\mathbf{E}_0| r \cos\theta + \frac{\mathbf{p} \cdot \mathbf{r}}{4\pi\varepsilon_0\varepsilon_d r^3} \quad (1.17a)$$

$$\mathbf{p} = 4\pi\varepsilon_0\varepsilon_d a^3 \frac{\varepsilon - \varepsilon_d}{\varepsilon + 2\varepsilon_d} |\mathbf{E}_0| \quad (1.17b)$$

From above we can infer that the applied field induces a dipole moment whose magnitude is proportional to  $|\mathbf{E}_0|$ . Then we introduce the polarizability defined via  $\mathbf{p} = \varepsilon_0\varepsilon_d\alpha\mathbf{E}_0$ , where

$$\alpha = 4\pi a^3 \frac{\varepsilon - \varepsilon_d}{\varepsilon + 2\varepsilon_d} \quad (1.18)$$

This is the polarizability of a sub-wavelength metallic sphere satisfying the Drude model (1.9). It can be deduced from (1.18) that the polarizability reaches maximum when  $|\varepsilon + 2\varepsilon_d|$  is a minimum. In other words, the polarizability undergoes a resonance when

$$\text{Re}[\varepsilon(\omega)] = -2\varepsilon_d \quad (1.19)$$

in the situation where there is a slow-varying  $\text{Im}[\varepsilon]$  around the resonance. This resonance condition (1.19) is called Fröhlich condition and corresponding mode the dipole surface plasmon.

The electric field  $\mathbf{E} = -\nabla\Phi$  then can be decided from Eq. (1.16). As can be concluded, both internal and dipolar fields also experience a resonant enhancement under the same condition as the  $\alpha$  resonates. It is this field enhancement at the plasmon resonance that many applications of metal nanoparticles including sensors and optical devices rely on.

Moving from electrostatics to electromagnetics, we focus on the radiated fields of a sub-wavelength sphere illuminated by a plane wave  $\mathbf{E}(\mathbf{r}, t) = \mathbf{E}_0 e^{-i\omega t}$ . The electric field leads to an oscillating dipole moment  $\mathbf{p}(t) = \varepsilon_0 \varepsilon_d \alpha \mathbf{E}_0 e^{-i\omega t}$ , with  $\alpha$  provided by (1.18). This oscillating, radiative dipole induces scattering of the plane wave by the particle. This can be treated as a dipolar radiation problem where the electromagnetic fields associated with an oscillating electric dipole can be expressed as [3]

$$\mathbf{E} = \frac{1}{4\pi\varepsilon_0\varepsilon_d} \left\{ k^2 (\mathbf{n} \times \mathbf{p}) \times \mathbf{n} \frac{e^{ikr}}{r} + [3\mathbf{n}(\mathbf{n} \cdot \mathbf{p}) - \mathbf{p}] \left( \frac{1}{r^3} - \frac{ik}{r^2} \right) e^{ikr} \right\} \quad (1.20a)$$

$$\mathbf{H} = \frac{ck^2}{4\pi} (\mathbf{n} \times \mathbf{p}) \frac{e^{ikr}}{r} \left( 1 - \frac{1}{ikr} \right) \quad (1.20b)$$

where  $k = 2\pi/\lambda$  and  $\mathbf{n}$  is the unit vector along the direction of point P. Particularly in optics, we are interested in the effect that the resonantly enhanced polarizability  $\alpha$  has on the scattering and absorption efficiency of a metal nanosphere. Their respective cross sections can be calculated from the Poynting vector determined by (1.20) [39]:

$$\sigma_{\text{sca}} = \frac{k^4}{6\pi} |\alpha|^2 = \frac{8\pi}{3} k^4 a^6 \left| \frac{\varepsilon - \varepsilon_d}{\varepsilon + 2\varepsilon_d} \right|^2 \quad (1.21a)$$

$$\sigma_{\text{abs}} = k \text{Im}[\alpha] = 4\pi k a^3 \text{Im} \left[ \frac{\varepsilon - \varepsilon_d}{\varepsilon + 2\varepsilon_d} \right] \quad (1.21b)$$

(1.21) shows that both scattering and absorption are also resonantly enhanced under the condition (1.19) where dipole surface plasmon resonance occurs. Furthermore, the extinction cross section for a nanosphere can be expressed as [40]

$$\sigma_{\text{ext}} = \sigma_{\text{sca}} + \sigma_{\text{abs}} = \frac{24\pi^2 a^3 \varepsilon_d^{3/2}}{\lambda} \frac{\varepsilon_i}{(\varepsilon_r + 2\varepsilon_d)^2 + \varepsilon_i^2} \quad (1.22)$$

We now relax the assumption of a spherical nanoparticle shape. For an arbitrarily shaped particle, the polarizability (1.18) can be expanded as [41]

$$\alpha = (1 + \chi) \varepsilon_0 V \frac{\varepsilon - \varepsilon_d}{\varepsilon + \chi \varepsilon_d} \quad (1.23)$$

and extinction cross section as

$$\sigma_{\text{ext}} = \frac{24\pi^2 a^3 \varepsilon_d^{3/2}}{\lambda} \frac{\varepsilon_i}{(\varepsilon_r + \chi \varepsilon_d)^2 + \varepsilon_i^2} \quad (1.24)$$

where  $V$  is the volume of the particle,  $\chi$  accounts for the geometrical factor of the particle and is assigned a value of 2 for the above case of sphere particle and can be as large as 20 for some shapes like nanorods [42]. Various shapes of NP have been modeled to make LSPR absorption fall in the range from visible to infrared frequencies, shown in Fig. 1.10. It can be noted that spectra exhibit red-shifted peaks with the trend of increased sharpness or edges of the NP due to larger charge separation resulting in weakened restoring force, while symmetric shapes produce increases of LSPR intensity. Also the number of LSPR peaks depends on the number of modes where a given NP can be polarized [43–45]. Therefore, nonspherical NP tend to have red-shifted, multiple peaks with respect to spherical particles.

### Mie theory

We have obtained a resonantly enhanced polarizability (1.18) when the Fröhlich condition (1.19) is met for a small sphere. In this case, the NP acts as an ideal electric dipole having enhanced absorption and scattering cross-sections, as well as a field enhancement in close vicinity of the NP surface. This dipolar mode of surface plasmon resonance exists only for vanishing particles, theoretically; in practice, however, we can have good approximation for particles whose dimensions are less than 100 nm using the theory above.

Nevertheless, for particles with larger dimensions, the quasi-static approximation loses its effectiveness due to phase difference of the driving field over the particle volume. Thus, a rigorous electrodynamic approach is needed. In a seminal paper, Mie in 1908 developed a complete theory of the scattering and absorption of electromagnetic radiation by a sphere, in order to understand the colors of colloidal gold particles in solution. The approach is now known as Mie theory is to expand the internal and scattered fields into a set of normal modes described by vector harmonics. The quasi-static results valid for sub-wavelength spheres are then recovered by a power series expansion of the absorption and scattering coefficients and retaining only the first term [3].

### LSPR sensors

In the experiments, LSPR is detected as a resonant peak in the absorption or extinction spectra as shown in Fig. 1.10. The spectra are recorded usually using a spectrophotometer with UV-vis wavelength range and at a fixed incident angle typically at normal incidence. The absorption peak will experience a spectral shift with fluctuating dielectric constant of the environment, which we can call spectral interrogation in a similar way as its counterpart in SPR sensors. The magnitude of the spectral shift of LSPR extinction for small NPs can be described by the following relationship [46, 47]:

$$\Delta\lambda_{max} = m\Delta n \left[ 1 - \exp\left(\frac{-2d}{l_d}\right) \right] \quad (1.25)$$

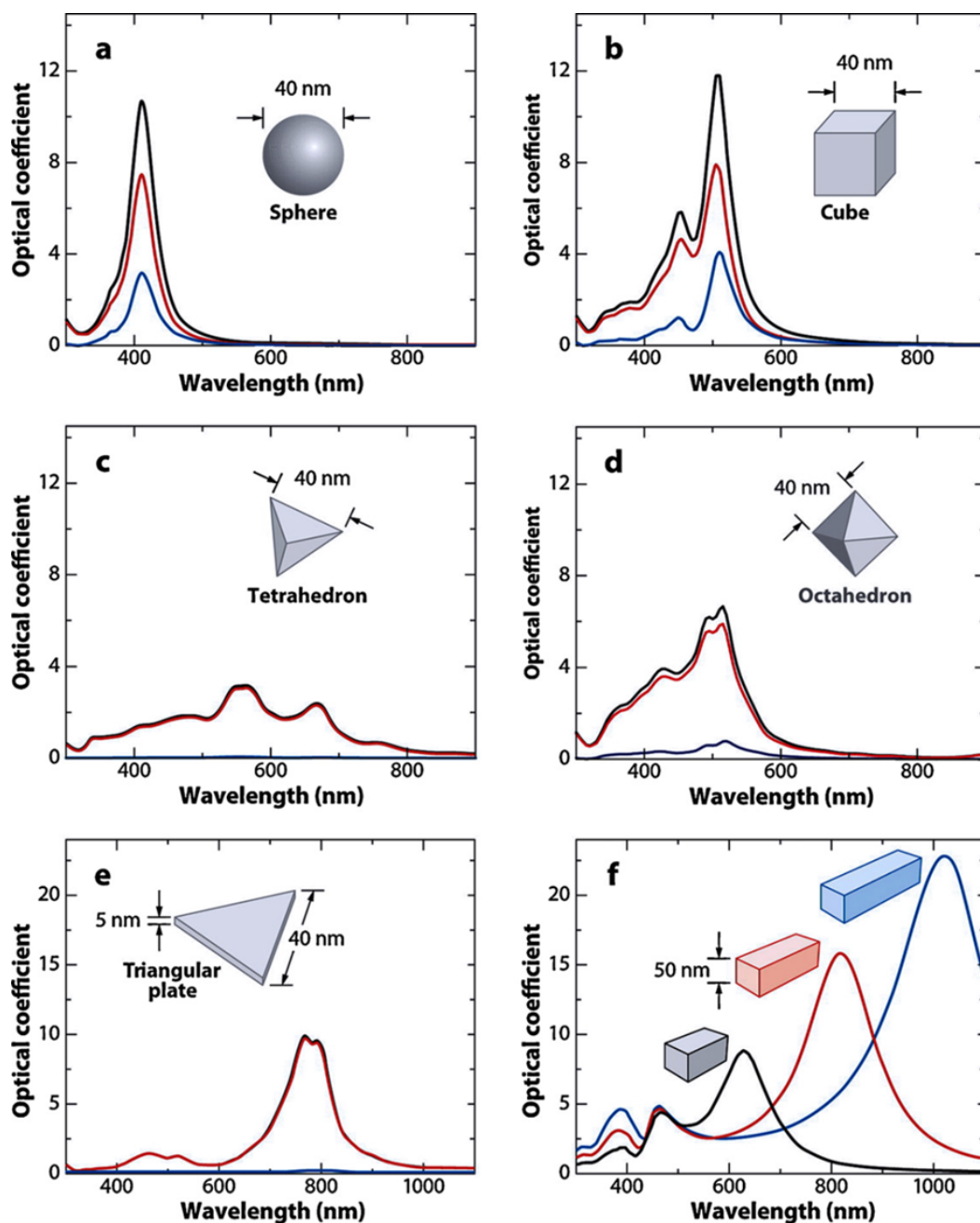


Figure 1.10: Extinction (black), absorption (red), and scattering (blue) spectra calculated for Ag nanoparticles of different shapes: (a) a sphere, (b) a cube, (c) a tetrahedron, (d) an octahedron, and (e) a triangular plate. (f) Extinction spectra of rectangular bars with aspect ratios of 2 (black), 3 (red), and 4 (blue). Figure taken from [44]

where  $m$  is local slope over a small range on the response curve of the LSPR wavelength versus bulk refractive index (in nm/RIU),  $\Delta n$  is the change in refractive index (in RIU),  $d$  is the effective thickness of the adsorbed layer (in nm) and  $l_d$  is the characteristic EM field decay length (in nm). Here we refer to 'refractive index unit' or 'RIU' as the unit of refractive index, although the refractive index is actually unitless. The expression given in Eq. (1.25) serves as the sensing principle for LSPR sensors. Likewise, the sensitivity of LSPR sensors is defined as the ratio of resonant wavelength shift  $\Delta\lambda$  to the change of ambient refractive index  $\Delta n$ :

$$S = \frac{\Delta\lambda}{\Delta n} \quad (1.26)$$

$S$  is usually expressed in nm/RIU. Another parameter used to evaluate the performance of a LSPR sensor is the figure of merit (FOM), defined as the sensitivity  $S$  divided by full width at half maximum (FWHM) of the resonance:

$$FOM = \frac{S}{FWHM} \quad (1.27)$$

As compared to SPR sensors having drawbacks in applications due to its bulky nature and low resolution [48, 49], LSPR sensors show advantages in optimizing sensing performance by tailoring various size and shapes of nanoparticles, to obtain absorption spectra with sharper peak and higher intensity. This will yield a better FOM quality and allow detection of extremely low concentrations of molecules with surface-enhanced Raman scattering [50, 51]. The sensitivity of LSPR sensors needs yet to be improved. Great efforts have been devoted to ameliorate sensitivity, FOM and spectral resolution of LSPR sensors by designing varied nanostructures: using inter-coupling between spherical nanoparticles [52], employing multipolar resonance in nanostructures such as nanodisks, nanocrescents [53, 54], and the use of plasmon hybridization of individual nanostructures, for instance, nanorings, nano-shells, nano-stars and nano-pillars [55–58].

## 1.2 Magnetoplasmonic structures to enhance the sensing

Although SPR and LSPR sensors have already shown a high sensitivity, even been commercialized by several companies, there are still great demands of sensors with ultra-high sensitivity for direct detection of low concentrations of tiny molecules. For this reason, it would be valuable to improve the sensing performance whilst preserving the advantages of SPR nature. It is well known that modulation technique can increase the signal-to-noise ration (SNR) and enhance the detection limits of any kind of sensor [59]. Therefore different modulation methods have been proposed during the last decades to carry out active SPR modulation based on different controlling ways: thermal [60], electric [61] and photonic [62]. In particular, the field called *magnetoplasmonics* combines magnetic field

and SPR to explore new phenomena in material science [1] such as the enhancement of magneto-optical activity in various magnetoplasmonic structures, active control of the propagating of surface plasmons using external magnetic field. The interaction between magnetic field and SPR allows devising bio- and chemical sensors, which we call the magnetoplasmonic sensors. They are based on the magneto-optical (MO) activity of the magnetoplasmonic structures, mainly the magneto-optical Kerr effect (MOKE). There are also two kinds of sensors according to the surface plasmon type: MO-SPR sensors and MOLSPR sensors.

### 1.2.1 Magneto-optical Kerr effect (MOKE)

Magnetoplasmonics are basically magneto-optics because the commonly used materials for plasmonics are silver and gold whose plasmon resonance falls in the range of optical frequencies. Therefore, concepts about the magneto-optics should be discussed beforehand. The modifications of the optical properties of materials induced by magnetic field, i.e. the magneto-optical (MO) effects, were first discovered by M. Faraday in 1845 and J. Kerr in 1878. They observed a change in the polarization state of the transmitted light or reflected light when an external magnetic field was applied to a glass or a ferromagnetic metal, which are called the Faraday effect or Kerr effect, respectively. Ever since then, magneto-optics have been used to develop information storage, as well as optical devices such as modulators, isolators or sensors. Let us take the Kerr effect as the example to introduce the basic concepts in magneto-optics. Under the presence of a magnetic field, the optical constants of an isotropic material becomes non-diagonal, represented by a generalized dielectric tensor:

$$\boldsymbol{\varepsilon} = \varepsilon \begin{bmatrix} 1 & -iQ_V m_z & iQ_V m_y \\ iQ_V m_z & 1 & -iQ_V m_x \\ -iQ_V m_y & iQ_V m_x & 1 \end{bmatrix} \quad (1.28)$$

where  $m_i (i = x, y, z)$  are the components of the unit vector magnetization  $\mathbf{m} = \mathbf{M}/M_s$  ( $M_s$ =saturation magnetization) along  $x, y, z$  directions.  $Q_V$  is the magneto-optical coupling constant (Voigt constant). The complex off diagonal components in dielectric tensor are responsible for the change of the polarization state of light. The polarization change can be rigorously derived from (1.28), Maxwell's equations, and the proper boundary conditions. The symmetry of the solutions can also be described by simple arguments using the concept of a Lorentz force acting on light agitated electrons [63].

We assume the magnetic field is oriented perpendicular to the surface (Fig. 1.11a). Then a linearly p-polarized light incident upon the material will excite electrons to oscillate parallel to the plane of the electric field  $E$ . This gives rise to a regularly reflected light which is polarized in the same

plane as the incident light. We call this the normal component  $\mathbf{R}_N$  of the reflected light. At the same time, the Lorentz force induces a small component of vibrational motion perpendicular to both the primary motion (normal component) and the direction of magnetization. This additional motion, which is proportional to  $v_{\text{Lor}} = -m \times E$ , generates a secondary Kerr component  $\mathbf{R}_K$ . Generally, the two components are not in-phase and it is the superposition of these two components that gives rise to an elliptically polarized reflected field featuring a Kerr rotation  $\theta$  and ellipticity  $\epsilon$ .

There are three types of MOKE geometries depending on the orientation of magnetization with respect to the incidence plane, as illustrated in Fig. 1.11. In the polar configuration (PMOKE) (Fig. 1.11a), the magnetization is aligned along the surface normal. When a linear p-polarized (s-polarized) field is reflected from the surface, a small component of s-polarized (p-polarized) field arises in the reflected light. It should be noted that at normal incidence ( $\vartheta = 0^\circ$ ), this effect is strongest and the same for all polarization directions of incident light.

Similar effects can be observed in longitudinal configuration (LMOKE) (Fig. 1.11b) where magnetization is parallel to both the sample surface and incidence plane. However, the incident light has to be inclined relative to the sample surface ( $\vartheta \neq 0^\circ$ ). In addition, the effects exist for both p-polarized and s-polarized incident light, and are opposite concerning the sense of rotation in these two cases.

On the contrary, a different situation occurs for transverse configuration (TMOKE) in which the magnetization is perpendicular to the plane of incidence. In this configuration, p-polarized light will generate a Kerr component in the reflected beam, while s-polarized light will experience no variation because the cross-product of Lorentz force is zero. The transverse configuration therefore causes no polarization rotation or ellipticity but a change in the reflected intensity of the p-polarized light (See Fig. 1.11c).

## 1.2.2 MOSPR sensors based on magnetoplasmonic thin films

One of the concepts of magnetoplasmonics is involving the control of surface plasmons properties using magnetic field. The magnetic field effects on plasmonic properties were initially analyzed on structures made from degenerate semiconductors, where surface plasmons occur in the far-infrared region. It was shown that depending on the relative orientation of the surface plasmon wave vector and the applied magnetic field, the magnetic field could control properties of surface plasmons such as, for example, propagation or localization. Since then, the magnetic field modulation effects on surface plasmons have found applications in optical isolation, acousto-magnetoplasmonics or plasmon-mediated MO transparency [64, 65]. A recent interest has been stimulated towards ultrafast

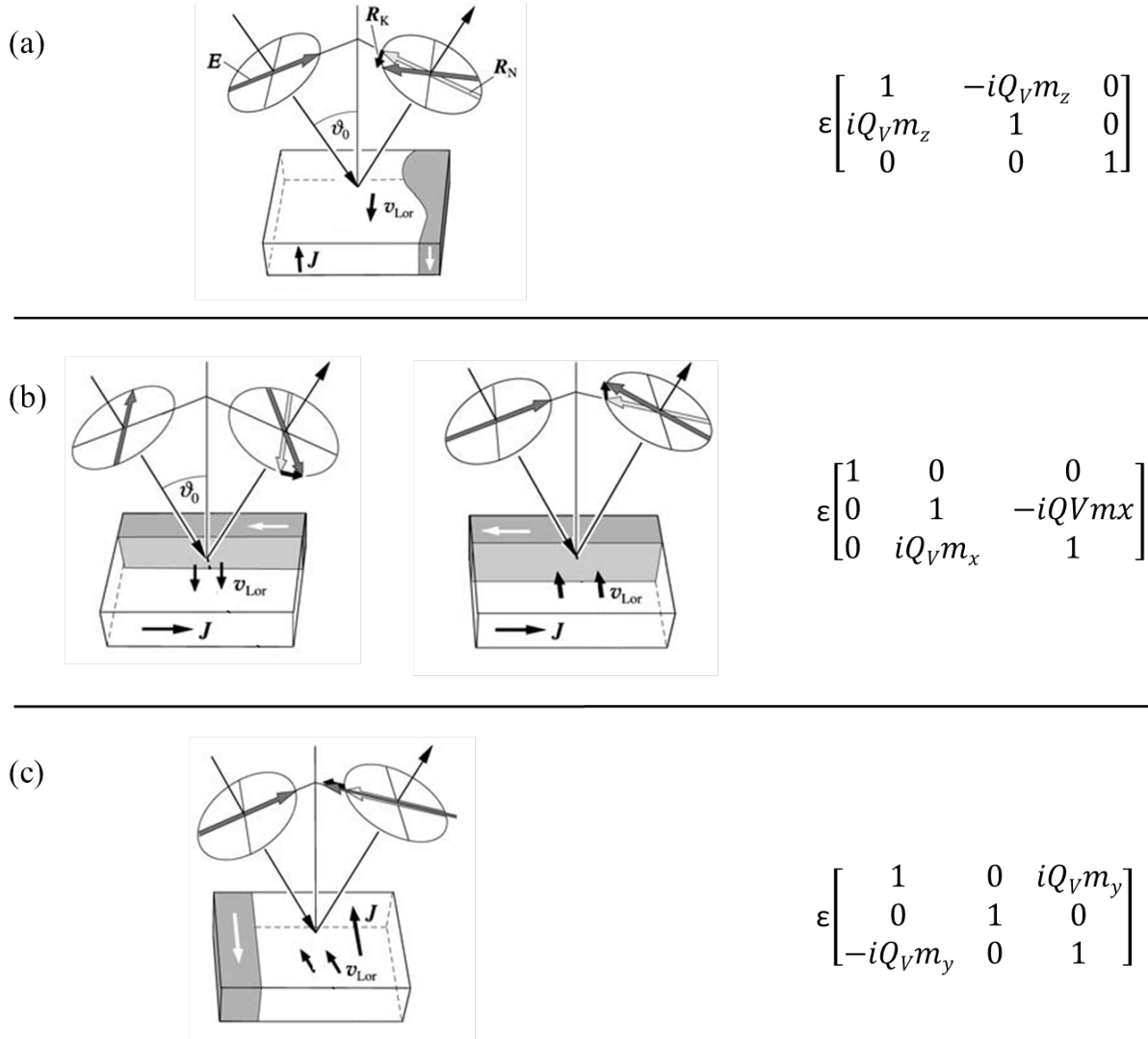


Figure 1.11: Three configurations for magneto-optical Kerr effect, defined according to the relative orientation between the magnetic field and the plane of incidence. The three rows indicate respectively the configurations of PMOKE, LMOKE and TMOKE and their respective dielectric tensors. Figure extracted from [63]

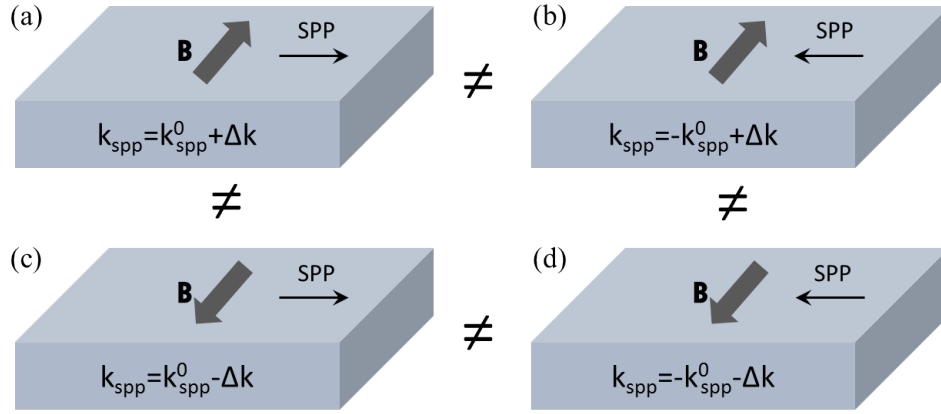


Figure 1.12: SPP non-reciprocity effect induced by magnetic field. For a given propagating direction of a SPP, the sign of the wave vector change  $\Delta k$  is reversed when the direction of magnetic field is switched. Likewise, the wave vector of a SPP along one direction is different from that of a SPP propagating in the opposite direction under the same external magnetic field.

magnetoplasmonics with hybrid plasmon–ferromagnet thin films systems for the eventual on-chip control of light [66]. One of the most promising application is biosensing and molecule detection. It is worth mentioning that for localized surface plasmons, magnetic modulation effects are too small to be observed in an actual system under moderate strength of magnetic field.

The magnetic field induced modulation of SPPs were analyzed with all the three MOKE configurations for the most common geometry of an interface between two semi-infinite media [67–69]. Specifically, when the MOKE configuration is either polar or longitudinal, it induces a TE component in the originally pure TM surface wave. On the other hand, the transverse configuration preserves the TM nature of the SPPs, i.e. there is no polarization conversion and only induces a linear modification in the value of wave vector  $k_{spp}$ , which can be expressed by:

$$k_{spp} = k_{spp}^0 + \Delta k \quad (1.29)$$

where  $k_{spp}^0$  is the SPP wave vector without magnetic field and  $\Delta k$  the wave vector variation induced by applied magnetic field or magnetization. The magnetic field also introduces another fascinating effect called non-reciprocity as shown in Fig. 1.12, an effect that serves the foundation of MOSPR sensing.

In actual demonstrations of MOSPR sensors, the SPP traveling direction is kept unchanged while switching the magnetic field (Fig. 1.12a and c). Combining Eq. (1.12) and (1.29), we can get the

following expressions when reversing the direction of magnetization:

$$\begin{aligned} k_{spp} &= k_{spp}^0 + \Delta k = nk_0 \sin\theta_1 \\ k'_{spp} &= k_{spp}^0 - \Delta k = nk_0 \sin\theta_2 \end{aligned} \quad (1.30)$$

This angle shift caused by the non-reciprocity manifests itself in the SPR reflectivity curves shown in Fig. 1.14a. Although magnetic field induced modulation of SPP wave vector is very appealing for the development of sensors, however, for pure noble metals their MO constants are very small [70, 71], the magnetic field required to achieve proper control of SPPs is extremely high for practical applications. To reduce this magnetic field, hybrid structures made from the combination of ferromagnetic materials and noble metals have been proposed. Ferromagnetic metals are known for their large MO constants, roughly three orders of magnitude larger than those of noble metals [72]. Thus the ferromagnetic material brings the high MO activity while the noble metals allow surface plasmons excitation. Another advantage of this combination lies in the good compromise of optical loss for both materials, which in the end determines the quality of plasmon response. Noble metals are distinguished for their low optical loss and well-defined plasmon resonance, in contrast with ferromagnetic metals exhibiting high loss and quite broad plasmon resonance [39, 73, 74]. Therefore various magnetoplasmonic systems can be proposed by intertwining the two kinds of materials in proper ways, to develop chemical and biosensing platforms.

B. Sepúlveda *et al* [75] first proposed a highly sensitive magneto-optical surface plasmon resonance (MOSPR) sensor based Co/Au multilayer. The performance of the MOSPR sensor is characterized by evaluating the MO Kerr effect of a p-polarized laser using transverse Kretschmann configuration. The MO effect is sharply enhanced in the reflectivity by formulating a difference signal  $\delta$ :

$$\delta = \frac{\Delta R_{pp}}{R_{pp}} = \frac{R_{pp}(H) - R_{pp}(0)}{R_{pp}(0)} \quad (1.31)$$

where  $R_{pp}(H)$  and  $R_{pp}(0)$  are the reflectivity of the p-polarized light, with and without magnetic field  $H$  respectively. As can be observed in Fig. 1.13a, the experimental results are in good agreement with the theoretical calculation for the  $\delta$  signal. More importantly, the sensitivity of MOSPR sensor is approximately three times higher than that of a SPR sensor (Fig. 1.13b).

A different structure using Au/Fe/Au trilayer as transducers of the MOSPR sensor was proposed [59]. In this case, the magnetization can be reversed by an external (ac) magnetic field, allowing modulating the SPP excitation condition. Thus the  $\delta$  signal becomes:

$$\delta = \frac{\Delta R_{pp}}{R_{pp}} = \frac{R_{pp}(H+) - R_{pp}(H-)}{R_{pp}(0)} \quad (1.32)$$

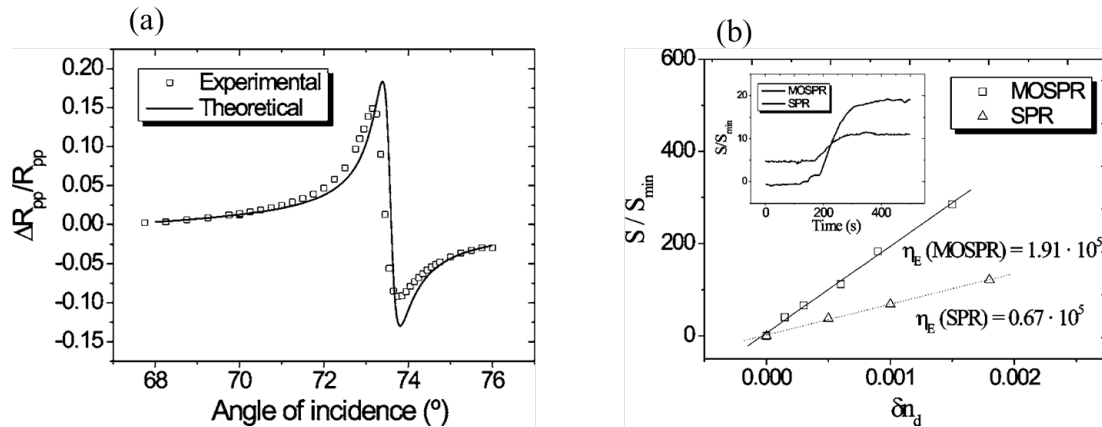


Figure 1.13: (a) Experimental and theoretical curves of  $\delta$  signal of Cr/Co/Cr/Au multilayer as function of incident angle. Such structure has the most sensitive MO effects and Cr is used for better adhesion and stability. (b) Comparison of experimental sensitivities of SPR and MOSPR sensors. Inset is the normalized signal of the detection of the physical absorption of bovine serum albumin proteins. Extracted from [75]

where  $R_{pp}(H+)$  and  $R_{pp}(H-)$  represent the reflectance with opposite orientation of magnetic field.  $\delta$  is greatly enhanced when the SPP is excited (Fig. 1.14b). Different from the intensity interrogation SPR sensor measuring the change of  $R_{pp}$ , the MOSPR sensor evaluates the variations in the magnified  $\delta$  signal induced by SPP excitation (Fig. 1.14c). This yields an experimental twofold increase in the MOSPR sensitivity under a lower magnetic field (20 Oe).

Kämpf *et al* theoretically evaluated a similar MOSPR sensor of Au/Co/Au trilayer system using transfer matrix method [76]. The calculation results show that, in comparison with SPR sensor, the higher sensitivity ( $S = \Delta I/\Delta n$ ) of the MOPSR sensor is dominated by the larger change of intensity per angle ( $S = \Delta I/\Delta A$ ), albeit smaller angle shift per refractive index ( $S = \Delta A/\Delta n$ ). Additionally it has been demonstrated in this work that the maximum MOSPR signal  $\delta$  depends on the thickness of each metallic layer, and for different dielectric matrix, the optimal thickness combinations are different, which allows the best design of the layer thickness to satisfy the specific sensing needs. Similar efforts in the thickness optimization have also been made in [77, 78].

A modified MOSPR sensor was proposed by S. David *et al* [79], containing a thin layer of Co-Au alloy capped with a layer of Au. This alloy not only exhibits both plasmonic and magnetic properties, but also brings increased structural stability in (saline) liquid surroundings, that common MOSPR sensors (successive layers of homogeneous metals) are not able to provide, because the Co-Au alloy has more physical and biochemical stability.

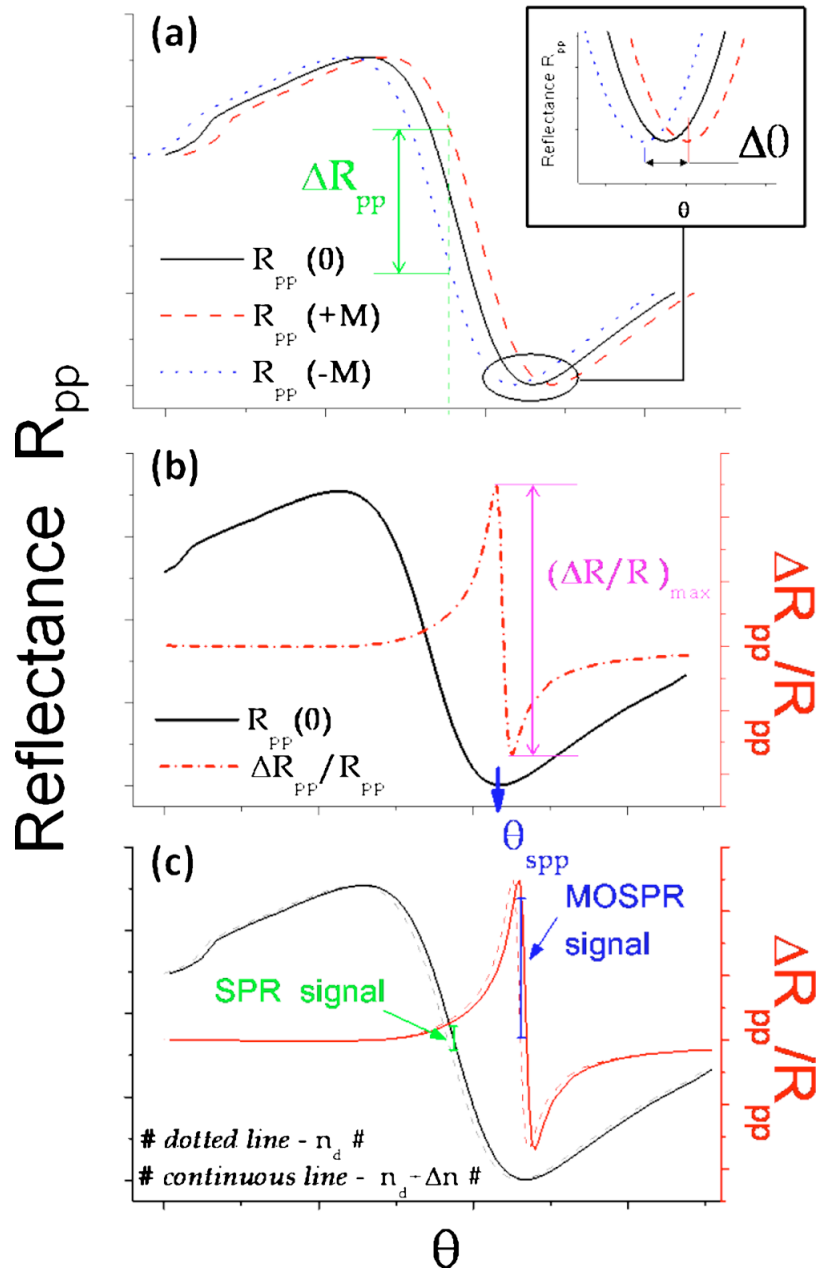


Figure 1.14: (a) modulation of SPP excitation condition by alternating magnetic field, resulting in angle shift. (b)  $\delta$  signal enhancement at SPP excitation condition. (c) response of SPR and MOSPR sensors to the same refractive change ( $\Delta n$ ). Extracted from [59]

### 1.2.3 MOLSPR sensors based on magnetoplasmonic nanodots

On the other hand, the interests of the magnetoplasmonics have been increasingly focused on the LSP-based systems with magnetic nanostructures and hybrid magnetic-nanoplasmonic structures, although not as extensive as the ones based on SPPs. Opposite to SPP-based magnetoplasmonic nanostructures where the magnetic field introduces modulations on plasmonic properties, for systems bearing LSP natures, it is the plasmons that exert strong effects on magneto-optical activity by inducing phase modification of the reflected or transmitted light. The enhancement of MO effects [80] and the large tunability of the magneto-optical response [81] due to LSP excitation are achieved. In practice, these effects start to play a prominent role in the design of next-generation magnetic recording media [82], and magnetoplasmonic sensors that we are concerned about in this dissertation, which we call the MOLPSR sensors.

The MO activity of the MOLSPR systems can be evaluated by calculating the full reflectivity Jones matrix:

$$r = \begin{pmatrix} r_{ss} & r_{sp} \\ r_{ps} & r_{pp} \end{pmatrix} \quad (1.33)$$

where  $s$  and  $p$  represent the two polarizations. Then the complex Kerr rotation is defined as:

$$\Phi = \theta + i\epsilon = \frac{r_{ps}}{r_{pp}} \quad (1.34)$$

where  $\theta$  is the Kerr rotation and  $\epsilon$  is the Kerr ellipticity.  $r_{ps}$  is the polarization conversion that only occurs in polar and longitudinal MOKE configurations. The magneto-optical Kerr spectroscopy is used to record the Kerr rotation spectra and ellipticity spectra, and the plasmonic property is analyzed by conventional UV-vis absorption/extinction spectroscopy. In MOLSPR systems, the optical and MO properties are greatly associated with LSPR spectra, and can be tuned by adjusting the nanostructure. Moreover, the MO properties are considerably enhanced due to LSPR effect. This SPR enhancement effect on MO activity has been studied theoretically since Hui and Stroud predicted large Faraday effect in nanoparticle suspensions at the surface plasmon frequency of the particles [83, 84]. Real structures with different materials have subsequently been proposed.

Purely ferromagnetic metallic nanoparticles have been recently studied to demonstrate the LSPR effects on the MO activity. Admittedly, so far, the use of LSPs in pure ferromagnetic nanostructures has been limited due to the high Ohmic loss of these materials. However, having simultaneous ferromagnetic and plasmonic natures makes these structures suitable for exploring the plasmon-manipulated MO response. González-Díaz fabricated arrays of Ni nanowires and observed an enhancement in the Kerr rotation spectra around the frequency where the LSPR peak appears [85]. Similar to the

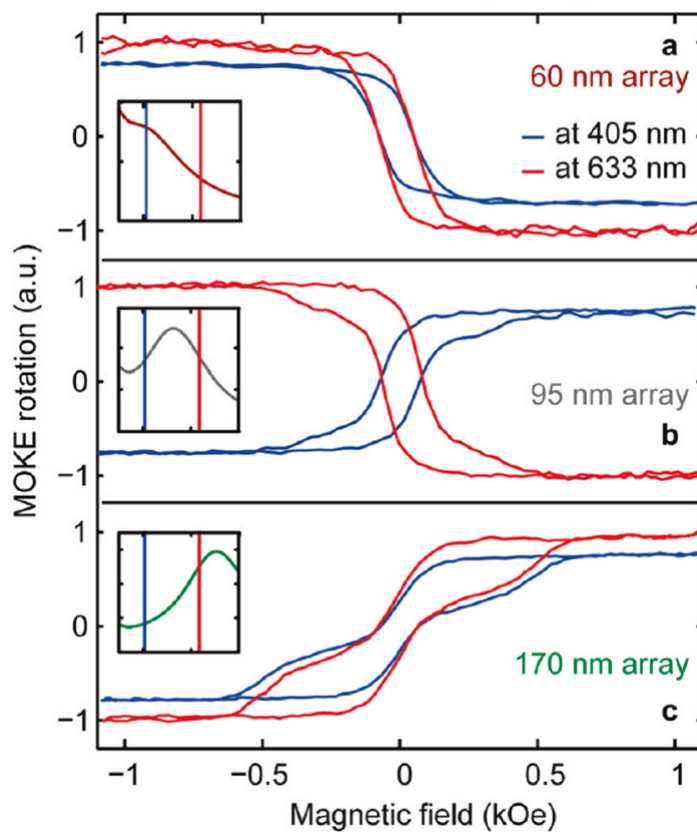


Figure 1.15: Normalized hysteresis loops of Ni nanodisks of 60 (a), 95 (b) and 170nm (c) using LMOKE configuration with p-polarized incident light. Wavelength is 405 nm (blue curves) and 633nm (red curves). The insets sketch the relative position between the LSPR peak of extinction spectra and the two excitation wavelengths. Extracted from [81]

nanowires case, Ni nanodisks also show LSPR effects on their MO properties [81, 86], where the inverse of MO rotation is observed (see Fig. 1.15). Even purely plasmonic nanostructure Au nanodisks can exhibit a sizable MO activity under magnetic field of the order of 1 T. MOLSPR systems have also been reported in nanostructures that combine both plasmonic and ferromagnetic components, mainly in noble metal - ferromagnet nanodisks. The first demonstration of such structures - a Au/Co/Au nanosandwich arrays - was given using polar MOKE configuration [87]. The varied diameter of the nanodisk gives rise to the spectral shift of LSPR peak, and then results in a similar shift trend in the corresponding spectra of Kerr rotation and ellipticity. Later, Meneses-Rodríguez [88] studied the MO properties of Au/Co/Au nanodisks by changing vertically the position of Co layer as a way to probe the electromagnetic (EM) field distribution inside the nanodisks, since the MO activity is proportional to the EM field inside the MO active material [78, 89]. It is shown that EM field upon LSPR excitation has maximum values with Co layer near the top and bottom surface, and a minimum value in the middle. Moreover, Banthí *et al* [80] presented an approach to further redistribute the EM field by inserting a dielectric ( $\text{SiO}_2$ ) layer into Au/Co/Au nanosandwiches. Large MO activity and low optical loss can be simultaneously obtained in a way that the ( $\text{SiO}_2$ ) layer is inserted at proper positions.

Among those, the magnetoplasmonic Ni nanoferrromagnets not only show the ability to actively control the MO response by use of the phase of LSPs [90, 91], but also allow design of ultrasensitive and molecular level sensing devices. Bonanni *et al* [81] proposed a refractive index (RI) sensor using Ni nanoferrromagnets. Since there is zero-crossing point in spectroscopic Kerr rotation  $\theta$ , the inverse value  $1/\theta$  can be defined so that a resonance is produced. The zero-crossing point has a red-shift in response to the change of surrounding RI, similar to that of extinction peak position shift in conventional LSPR sensors. The resonance in  $1/\theta$  has the same sensitivity to the RI change, but with an infinite FOM (infinitesimal FWHM of resonance).

A more precise method using Kerr ellipticity zero-crossing point was proposed by Maccaferri [90], based on the similar structure. The ellipticity variation  $\Delta\epsilon$  was measured at each wavelength  $\lambda$  by switching back and forth the saturating field  $H$ . The null point wavelength  $\lambda_c$  can be found on the spectrum curve (Fig 1.16b), and can be desirably obtained by tuning the relative phase of two excited LSPs through engineering size of the nanodisks. Therefore the zero-crossing point is also employed to build an inverse value to devise a MOLSPR sensor: sensitivity to RI changes is similar to that of other types of sensors, but with an unrivaled figure of merit.

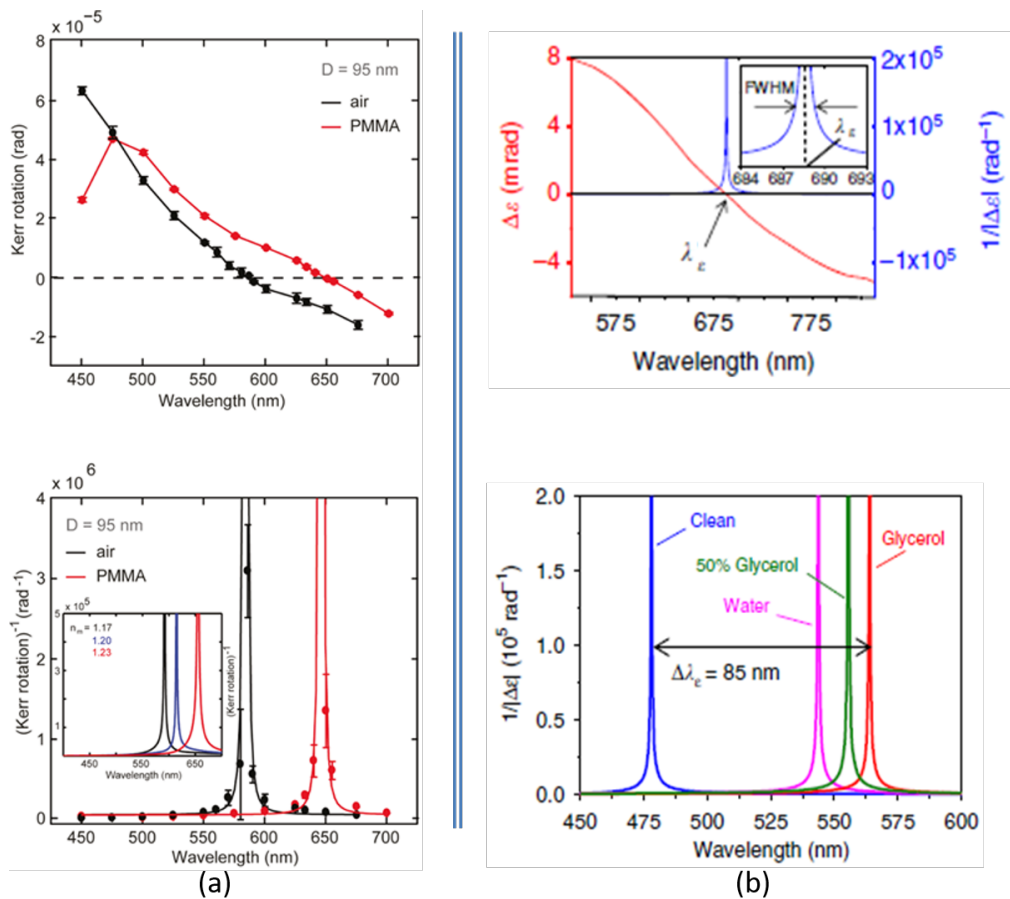


Figure 1.16: (a) Spectral curves of Kerr rotation (top) and its inverse (Kerr rotation) $^{-1}$  (bottom) in response to the RI change from air to PMMA. (b) Spectral curves of  $\Delta\epsilon$ ,  $(|\Delta\epsilon|)^{-1}$  and its resonance at  $\lambda_e$  (top). Shift of  $(|\Delta\epsilon|)^{-1}$  in response to the RI change (bottom). Extracted from [81, 90]

### 1.3 RIfS in nanoporous structures

The development of sensing devices using nanoporous materials has received a great deal of attention in the very recent years due to their unique physical and chemical properties. Porous silicon (Si) and oxidized porous silicon (SiO<sub>2</sub>) with large surface area have been exploited to achieve label-free biosensing and immunosensing [92, 93]. Another highly-ordered structure anodic aluminum oxide (AAO) has also been extensively studied and used in biosensors. This structure consisting of porous alumina (Al<sub>2</sub>O<sub>3</sub>) on aluminum (Al) substrate is formed by self ordering synthesis based on electrochemical anodization. Compared to sensing devices fabricated using high-cost and time-consuming lithography technique, AAO-based sensors have numerous advantages including simple, cheap fabrication, controllable pore parameters, large surface area allowing large-scale bio-interaction [94]. In addition, AAO demonstrates greater thermal and chemical stability and biocompatibility and has other unique optical, mechanical, and electrical properties that make it a competitive candidate for high-sensitivity devices [95].

Unlike other kinds of sensors based on optical methods such as surface plasmon resonance, enhanced Roman scattering, wave guiding and photonic band-gaps, AAO sensors rely on another highly sensitive optical sensing technique called reflective interference spectroscopy (RIfS), which is based on the interaction of white light with thin films. When light is reflected from AAO film, it generates an spectral pattern with fringes and well-resolved peaks, as a result of Fabry-Perot interference of light reflected from the air-Al<sub>2</sub>O<sub>3</sub> interface and Al<sub>2</sub>O<sub>3</sub>-Al interface (Fig. 1.17a). The expression of Fabry-Perot relationship is given by:

$$m\lambda = 2nL \quad (1.35)$$

where  $m$  is the order of the spectral fringe and  $n$  is the effective refractive index of AAO layer and its contents at the corresponding wavelength  $\lambda$ .  $L$  is the geometric thickness of porous layer, whereas  $2nL$  is referred as the optical thickness (OT) that can be obtained by Fourier transform of the RIfS signal. It can be straightforwardly concluded from Eq. (1.35) that any modification in refractive index or thickness of porous layer will result in a shift of the pattern.

The pioneering work by Pan et al. showed the capability of the RIfS-AAO system for label-free detection of complementary DNA [95, 96]. The real-time measurement of protein binding with AAO system was firstly demonstrated by Alvarez [97]. The detection method in this citation, however, is measuring the change in the OT ( $= 2nL$ ) which has a characteristic single peak (Fig. 1.17b).

Surface modification by deposition of Au was achieved by Yeom [98]. The Au coating brings an enhancement in the reflected intensity of RIfS signal due to the more reflective property of Au than

bare AAO. More importantly, Au introduces plasmonic properties to enhance the sensitivity through giving additional spectral shift caused by LSPR. (See Fig. 1.17)

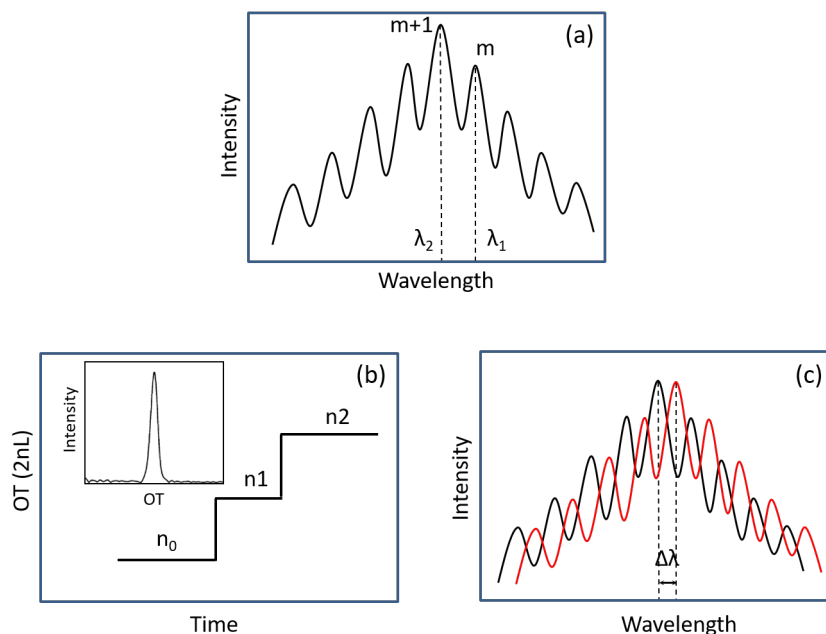


Figure 1.17: (a) Schematic of interference spectral pattern (RIFS signal). The wavelength corresponding to each peak in the spectrum is governed by the Fabry-Perot relationship. (b) Real-time monitoring of optical thickness (OT) signal by changing the surrounding refractive index. Inset is the Fourier transform of RIFS signal, featuring a single peak whose position along the x-axis corresponds to the OT. (c) Direct observation of wavelength shift of interference spectrum.  $\Delta\lambda$  for Au-coated AAO is greater than that for bare AAO due to the contributions from LSPR.

Song *et al* studied periodic nanoporous Ag/CoFeB/Ag structures fabricated using a monolayer nanosphere template, and found an synergistic influence of Ag layer and nanopores on the magnetic properties and magneto-optical properties [99]. Strongly enhanced ferromagnetic characters including coercivity  $H_c$ , exchange bias  $H_e$  and squareness (remanence/saturation magnetization:  $M_r/M_s$ ) are achieved as a result of the added Ag layer and existence of pores. The non-linearity of the magnetic field dependent reflected intensity of light is also enhanced due to local magnetism in the pores and the LSPR of Ag component. This opens exciting opportunities to develop multi-functional sensing devices by combining different techniques of RIFS, SPR and magnetic effects in one single structure.

## 1.4 Conclusion

In this chapter we gave the underlying physical principles that allow the use of the surface plasmon resonance for sensing purpose, since the plasmonic resonance is very sensitive to the changes of the refractive index. We have described the two kinds of plasmons that can be used: the surface plasmon polaritons (SPPs) and the localized surface plasmons (LSPs).

Then we explained how the use of magnetic materials can lead to the improvement of the sensitivity to the refractive index change through the service of Magneto-Optical (MO) properties. In MO-enhanced SPP sensors, the change of the direction of the magnetic field applied to the magnetic structure induces a shift in the SPP wave vector. Using an alternative magnetic field, a modulation technique can enhance the detection of the plasmon resonance shift. In MO-enhanced LSP sensors, the plasmonic resonance affects the MO response of the device, which can also be utilized as an efficient method to detect its shift.

Finally, we also have introduced the nanoporous anodic aluminum oxide (AAO) that is also sensitive to the refractive index changes. Although the MO effect has not been evidenced, the coupling of AAO porous structures and magneto-plasmonic layers seemed promising to enhance the sensitivity.

Up to date, only simple magnetic materials like Co, Fe or Ni have been used as the magnetic components in magneto-plasmonic structures. But other elements possess interesting magnetic properties, and as it has been demonstrated in the past decades, advances in nanotechnology allow the creation of nano-composites with tailored properties. Therefore, in this thesis we will explore the influence that new nanostructured magnetic materials including elements such as rare earth alloys with large magneto-optical effect can have on the properties of magneto-plasmonic structures. Through a proper nanostructuration we seek to obtain the MO enhancement and examine the possibilities of them being used in sensing applications.

In Chapter 2, magnetoplasmonic sensors based on SPPs with tailored magnetic properties in nanostructured FeCo/TbCo<sub>2</sub> layers will be studied and discussed in details.

In Chapter 3, we will propose a nanostructure with LSPR property of nanoparticle arrays and try to introduce continuous magnetic layers to find magneto-optical enhancement effects. Some preliminary results will be presented in this chapter.

Chapter 4 will present the studies on magnetoplasmonic devices with Ag/ITO/CoFeB/ITO/Ag multilayers deposited on nanoporously structured AAO substrates. Magnetic, optical and magneto-optical properties of the devices will be characterized.



## Chapter 2

# Thin-film magnetoplasmonic sensors with tailored magnetic properties

In the magnetoplasmonic sensors based on noble metal/magnetic material/noble metal thin-film structures reviewed in Chapter 1, the commonly used magnetic material is Co [75, 76]. Some other works are carried out with Fe, Ni [59], or with Au-Co alloy that gives better stability [79].

However, it is well known that the nanostructuring of magnetic layers allows the control of magnetic properties such as remanence, anisotropy, saturation magnetization, magnetostriction and so on. Kubler et al explored the properties of a Co layer biased with an IrMn layer [100], but no significant impact was shown on the plasmonic properties.

In this chapter we will investigate the replacement of the Co layer by nanostructured magnetic layers with controlled magnetic anisotropy. The complex refractive index of the nanostructured magnetic layers will be measured and applied in SPR calculation to obtain the thickness of individual layers. Different combinations of the magnetic layers will be designed to build different magnetoplasmonic structures. Then the fabrication of these devices will be realized accordingly. We will characterize the magnetic properties of these magnetoplasmonic structures, and look into how the magnetic uni-axial anisotropy of the nanostructured magnetic layers will affect the plasmonic properties in magnetoplasmonic sensors by performing magneto-optical SPR measurements.

## 2.1 Nanostructured magnetic layers

### 2.1.1 Introduction

The nanostructured magnetic multilayer used in the magnetoplasmonic sensors are originally developed in the AIMAN-FILMS group of IEMN for their magneto-elastic properties [101, 102]. The magnetostrictive coefficient of compounds such as  $\text{TbFe}_2$  known as Terfenol, and  $\text{TbCo}_2$ , is very high, but requires very high magnetic field to be fully saturated. For this reason, they are designed to be stacked together with Fe, Co or their alloys, who have a lower magnetostriction but also much lower saturation fields. In this so-called 'spring magnet' geometry, for a bilayer period of the order of less than 10 nm, the Heisenberg exchange interaction will strongly couple the magnetic moments of the 'hard' and 'soft' layers, giving rise to an averaging of their properties. In such multilayers, a suitable magnetostriction can be obtained with reduced saturation magnetic field, rendering them satisfactory for applications in the micro sensors and actuators domain.

### 2.1.2 Multilayers with controlled uni-axial anisotropy

The multilayer  $N \times (\text{TbFe}_2 \text{ or } \text{TbCo}_2 \ x \text{ nm} / \text{Fe or Co or FeCo } y \text{ nm})$  are deposited by the RF sputtering method in a Leybold Z550 equipment in the IEMN clean room facilities (Fig. 2.1). Base vacuum prior deposition is approximately  $3 \times 10^{-7}$  mbar. In order to induce a preferential orientation for the magnetic moments in the films, or 'uni-axial anisotropy', a magnetic field is applied on the substrate during the deposition.

The magnetic characterization is carried out using vibrating sample magnetometer (VSM). As can be seen in Fig. 2.2, even if an uni-axial anisotropy can be achieved in single  $\text{TbCo}_2$  layers, its characteristic is not perfect, and the anisotropy field  $H_A$  (saturation field along the hard axis) is quite high for practical applications. On the contrary, sputtering a single FeCo layer under magnetic field does not give rise to any uni-axial anisotropy. In the multilayer system  $10 \times (\text{TbCo}_2 \ 5 \text{ nm}/\text{FeCo } 5.6 \text{ nm})$ , however, a clear uni-axial behavior is obtained with a reasonable anisotropy field of about 1 kOe (0.1 Tesla).

## 2.2 Magnetoplasmonic sensors

In order to understand how the magnetic uni-axial behavior interacts with surface plasmons, we fabricated different types of magnetoplasmonic structures: one with the most conventional Au/Co/Au

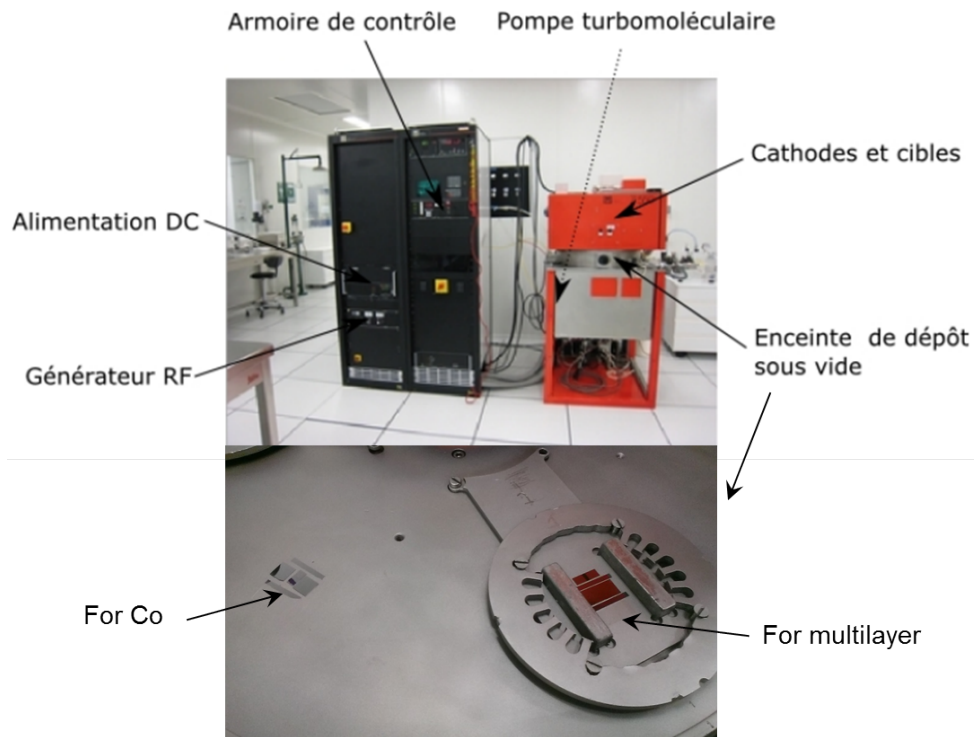


Figure 2.1: RF sputtering machine Leybold Z550 used for deposition of anisotropic magnetostrictive multilayer, as well as Co. Figures taken from [103]

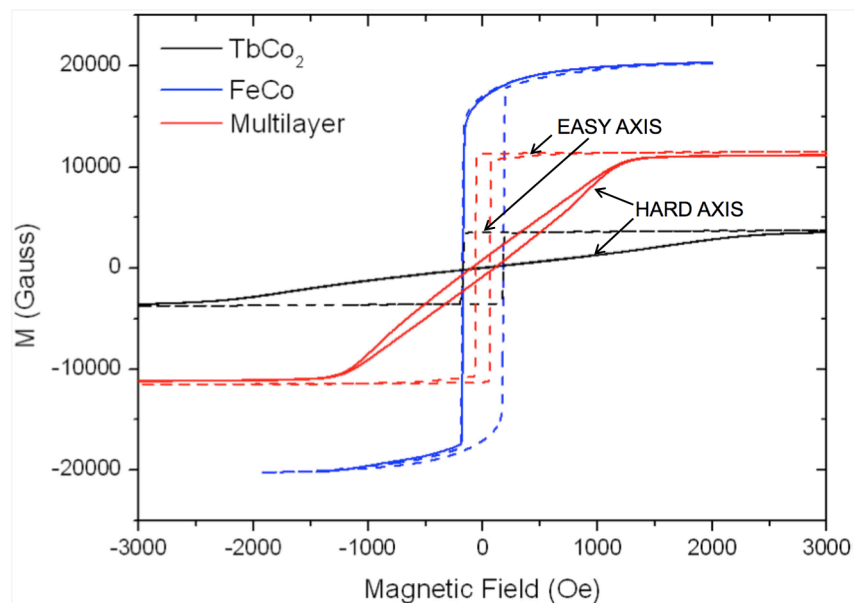


Figure 2.2: Magnetization loops measured by VSM for layers deposited under magnetic field. Single layers of  $TbCo_2$  and  $FeCo$ , and  $10 \times (TbCo_2 \text{ 5 nm}/FeCo \text{ 5.6 nm})$

structure serving as a control experiment, and the others with Co layer replaced by nanostructured magnetic stacks with uni-axial anisotropy, that is, Au/Multilayer/Au structure. We will investigate magnetic field induced effects on the plasmonic property by carrying out the magneto-optical SPR (MOSPR) measurements on these structures, and explore their capabilities of being developed for sensing applications.

### 2.2.1 Calculations for thicknesses of individual layers

Since the MOSPR measurements are made on an Autolab SPRINGLE machine available at IRI, the calculations should be done according to some specifications of the machine. The wavelength of the p-polarized laser is 670 nm. Also the offset of SPR angle by spindle is from  $62^\circ$  to  $78^\circ$ , and detected dynamic range of angle is  $4000 \text{ m}^\circ$ .

The other indispensable inputs for the calculation should be the complex refractive index of the constituent metals. Optical constants for Titanium, Gold and Cobalt can be found in literature [104, 105], but there is no existing data available for our magnetic multilayer so far. As a first approach, the complex refractive index as a function of wavelength in the UV-vis range has been measured for a  $10 \times (\text{TbCo}_2 \text{ 4 nm/FeCo 4 nm})$  uni-axial multilayer on a spectroscopic ellipsometer (HORIBA Jobin Yvon company), shown in Fig. 2.3. So at the laser wavelength 670 nm, the refractive index for all metallic layers used in the sensors are summarized in Table 2.1.

Table 2.1: Refractive index  $n$  and  $k$  at 670nm wavelength for all metals in magnetoplasmonic sensors

	<b>Ti</b>	<b>Au</b>	<b>Co</b>	<b>Multilayer</b>
<b>n</b>	2.78	0.14	2.26	2.62
<b>k</b>	3.87	3.79	4.31	3.67

With all the necessary information, we are able to perform the SPR calculations with the open source program WinSpall. Fig. 2.4 shows the calculated thickness for each layer in those structures.

Concerning the Au/Multilayer/Au structure, the sandwiched magnetic multilayer will use two kinds of combinations: FeCo/TbCo<sub>2</sub>/FeCo and FeCo/TbCo<sub>2</sub>/FeCo/TbCo<sub>2</sub>/FeCo. In the calculation we use the refractive index of  $10 \times (\text{TbCo}_2 \text{ 4 nm/FeCo 4 nm})$ , and the resulting thickness of 'Multilayer' is 5 nm. On one hand, we want more layers to be closer to 'homogeneous' material. On the other hand, given the magnetic multilayer thickness is only 5 nm, it is difficult to make too many layers because in that case the roughness between ultra-thin individual layers will disappear, ending up with

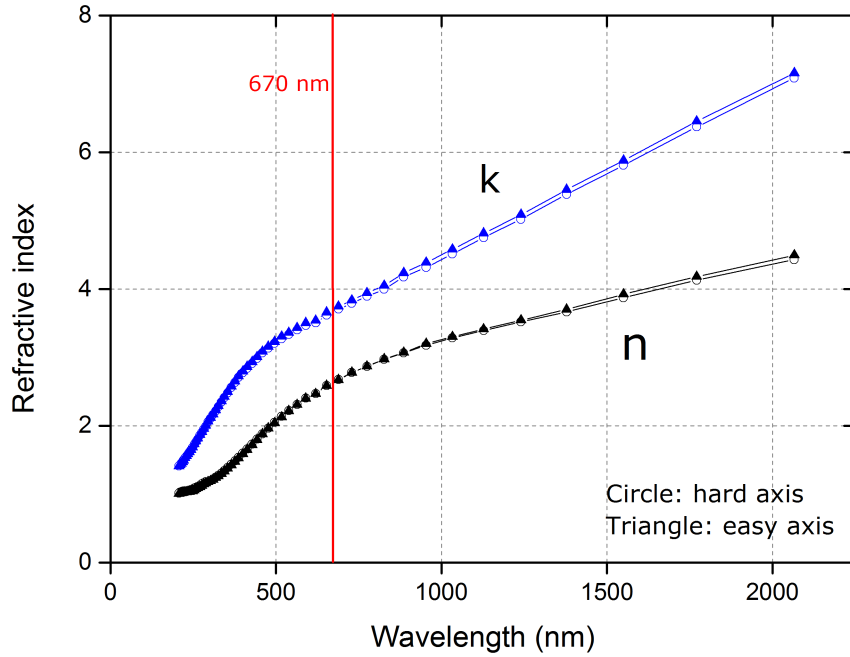


Figure 2.3:  $n$ - and  $k$ - spectra for the magnetic multilayer  $10 \times (\text{TbCo}_2 4 \text{ nm}/\text{FeCo} 4 \text{ nm})$  along hard axis and easy axis.

Table 2.2: Thickness for the 3-layer and 5-layer combinations of the magnetic multilayer

Multilayer	Thickness (nm)
FeCo / TbCo <sub>2</sub> / FeCo	1.25 / 2.5 / 1.25
FeCo / TbCo <sub>2</sub> / FeCo / TbCo <sub>2</sub> / FeCo	0.8 / 1.3 / 0.8 / 1.3 / 0.8

alloys. So we compromised to make two reasonable combinations with 3-layer and 5-layer magnetic materials FeCo/TbCo<sub>2</sub>. Their thickness allocation is shown in Table 2.2. Hence we will prepare three kinds of structures: Au/Co/Au, Au/FeCo-TbCo<sub>2</sub>-FeCo/Au and Au/FeCo-TbCo<sub>2</sub>-FeCo-TbCo<sub>2</sub>-FeCo/Au.

## 2.2.2 Sample realization

All the samples are prepared on the BK7 glass substrates with the following fabrication protocol:

1. Cleaning glass slides: prepare the piranha solution with great care by adding hydrogen peroxide (H<sub>2</sub>O<sub>2</sub>) to sulfuric acid (H<sub>2</sub>SO<sub>4</sub>) slowly. Immerse the slides into the solution for 5 minutes, then rinse with deionized water and dry with nitrogen.

2. A layer of Ti of several nanometers is thermally evaporated onto the glass substrate prior to the

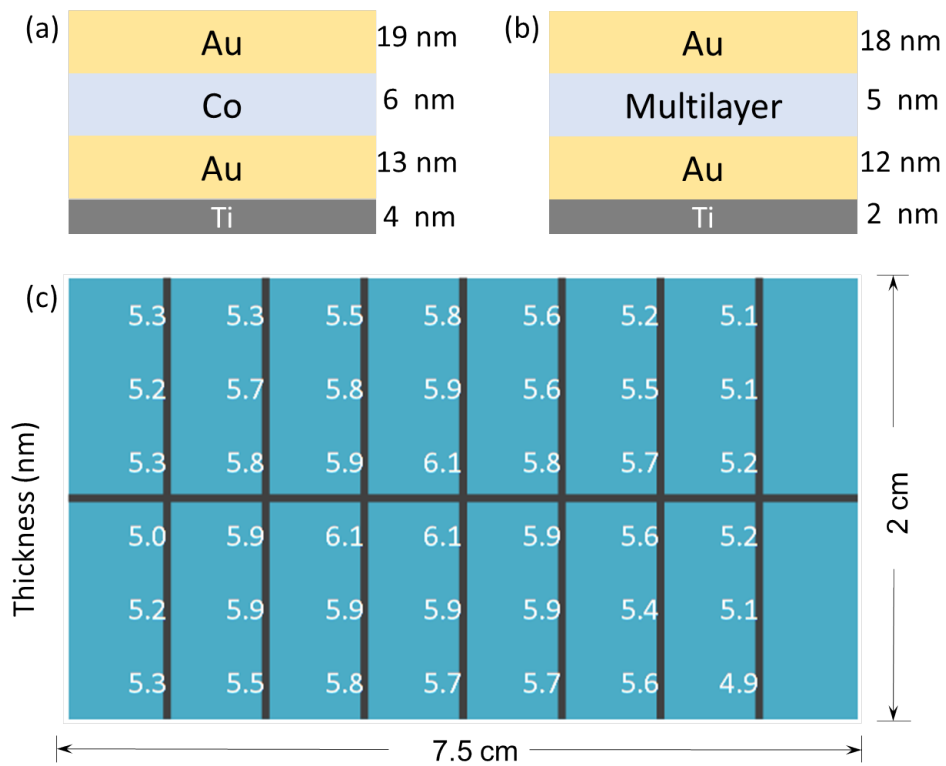


Figure 2.4: Calculated thickness for each metallic layer in Au/Co/Au (a) and Au/Multilayer/Au (b) structures. (c) Schematic of calibrated thickness for Co layer on the whole slide surface. The nominal targeted thickness was 6 nm.

Au layer so as to improve the adherence of Au layer to the glass surface. Then the required thickness of the first Au layer is deposited also by thermal evaporation.

3. The subsequent magnetic layers are deposited by RF sputtering at their respectively calibrated speed. Cobalt layer was deposited with no applied magnetic field on the sample whereas the multilayers were deposited using the magnetic holder shown in Fig. 2.1 in order to induce the uni-axial anisotropy.

4. Immediate thermal evaporation of the second Au layer is made right after the sputtering step to avoid too much oxidation of magnetic layers.

It should be noted that the thickness of RF sputtered magnetic layers is not homogeneous due to the unusually large substrate ( $2\text{ cm} \times 7.5\text{ cm}$ ) for the sputtering machine. So the calibration procedure is made by drawing a map on the glass slide. Fig. 2.4 (c) shows the measured thickness distribution of Co layer.

### 2.2.3 Magnetic characterization

The magnetic behaviors of the three types of samples are characterized by VSM. The magnetic properties of these magnetoplasmonic sensors are indeed strongly correlated to the properties of ferromagnetic layers inside.

Fig. 2.5a shows the magnetization loops of the Co-based structure. Although it was not deposited under magnetic field, it is not completely isotropic in the plane. The difference between the X and Y axis is not clear, but this could be due to the presence of the magnetic sample holder in the sputtering chamber. For these layers, the coercive field is about 45 Oe, but the saturation is not fully reached before more than 200 Oe of applied field. Upon removal of the field, magnetic domains appear in the layer leading to a remanent magnetization  $M_r$  which is lower than  $M_s$  but not zero.

As shown in Fig. 2.5b and c, the multilayer-based structures clearly exhibit a uni-axial behavior. Along the easy axis, the tri-layer structure almost exhibits a perfect squareness with a coercive field of about 31 Oe, and after reversal, saturation is fully reached for 70 Oe. The 5-layer structure has an even squarer magnetization loop with a coercive field of about 27 Oe and saturation is reached immediately after reversal for less than 50 Oe. From this point of view, the multilayer structure shows an enhancement compared to Cobalt: it can allow a reduction of the required magnetic field to control the magnetization. Along the hard axis, both multilayers exhibit similar characteristics with a slightly higher anisotropy field  $H_A$  for the 5-layer structure than 3-layer structure:  $H_{A3}$  is about 120

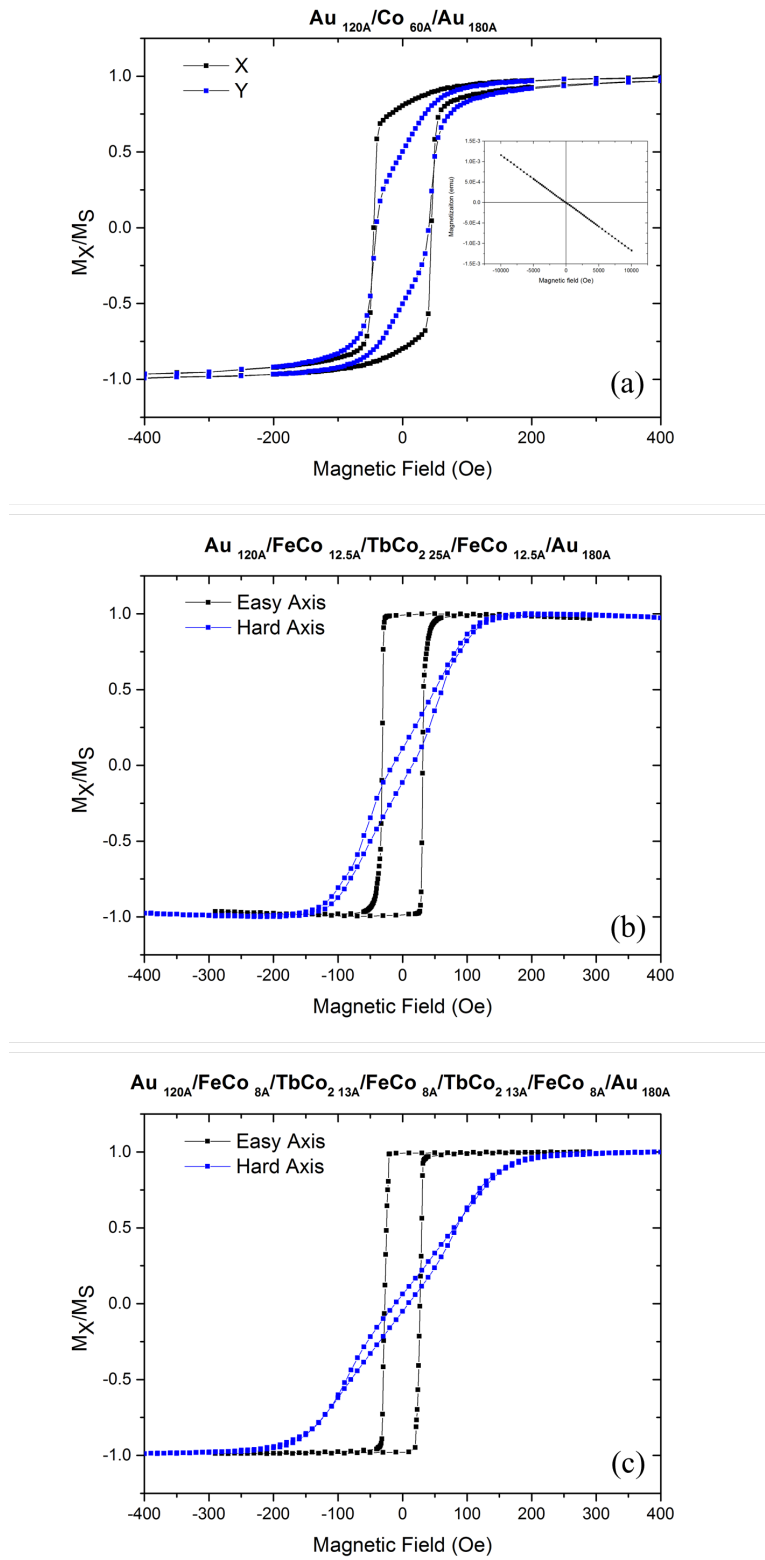


Figure 2.5: Magnetic behaviors of three magnetoplasmonic structures with magnetic layers to be Co, Multi-3 and Multi-5. Inset in (a) shows the VSM curve of bilayer Ti/Au with diamagnetic property, meaning that the ferromagnetic property only come from the magnetic layers.

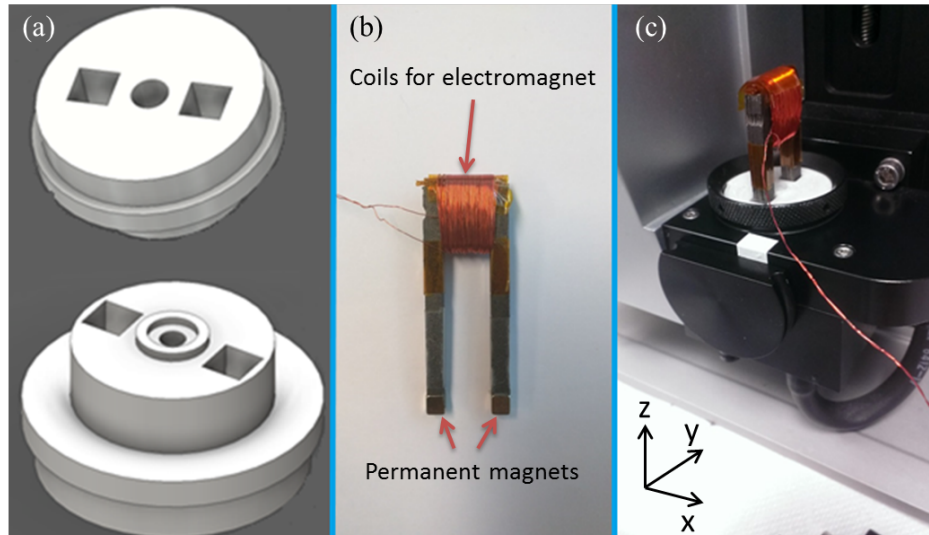


Figure 2.6: Home-customized components to introduce magnetic effect: (a) Schematic model of the holder for 3D-printing; (b) U-shape frame with permanent magnets or copper coils for electromagnet; (c) Plastic holder with inserted magnetic parts fitting into the machine.

Oe, whereas  $H_A5$  is about 150 Oe. Contrary to the easy axis, the behavior is not perfect on the hard axis and the remanent magnetization is not zero. One has to be cautious since the shape of the loops along the hard axis is usually quite sensitive to the alignment of the applied magnetic field.

#### 2.2.4 Magneto-optical SPR (MOSPR) measurements

The machine is originally designed to make the characterization of conventional SPR sensors. In order to implement magnetic effect, we need to adapt the machine to be able to characterize the magnetoplasmonic sensors. Firstly, we 3D-printed a specially designed holder for permanent magnets or electromagnet. Then we fashioned a U-shape iron frame to situate the permanent magnets at two ends, or to make an electromagnet as an alternative by winding a coil around the cross bar. In this way we built a magnetic part and are able to switch the orientation of the magnetic field, which allows the change of the SPR condition. Finally we fit the holder into the machine and perform the magneto-optical experiments (see Fig. 2.6).

Before everything starts, we want to find the right angle as the reference by applying DI water droplet on the surface of a single Au layer without magnetic field so that we have the same reference for all the following experiments. Then we performed the MOSPR characterization by applying the magnetic field and also DI water for the three structures

To facilitate the discussions, we use the terms Co sensor, Multi-3 sensor and Multi-5 sensor to

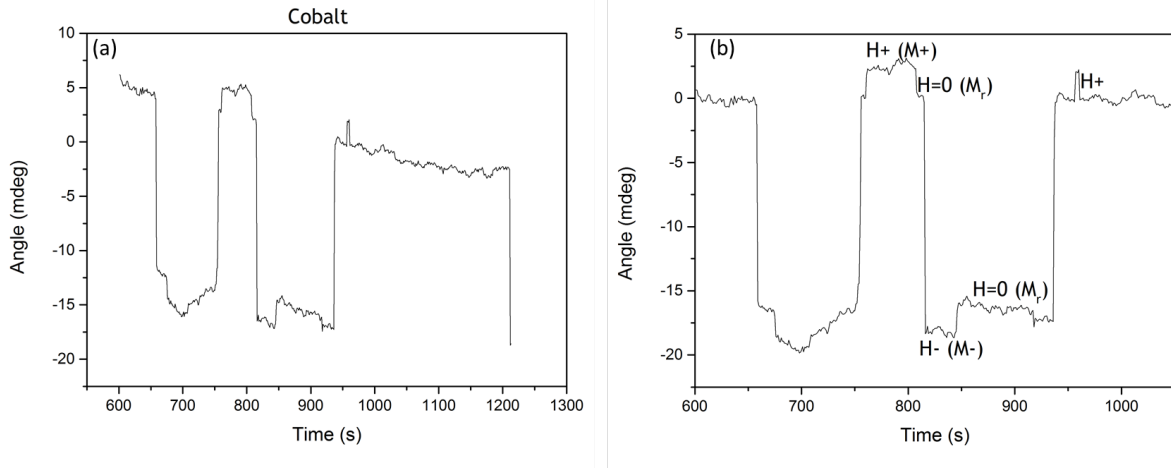


Figure 2.7: Binding curve for Co sensor: (a) Original binding curve. (b) Drift-removed binding curve, where the magnetic field states (magnetization) are noted.

represent the three types of sensors that are made up of the magnetoplasmonic structures Au/Co/Au, Au/FeCo-TbCo<sub>2</sub>-FeCo/Au and Au/FeCo-TbCo<sub>2</sub>-FeCo-TbCo<sub>2</sub>-FeCo/Au, respectively.

#### 2.2.4.1 Co sensor

Upon applying DI water droplet, the minimum reflectivity reaches to 18%. Then the direction of magnetic field  $H$  is manually turned back and forth by switching the magnetic piece to monitor the binding process. The process is demonstrated in a binding curve showing the evolution of the SPR angle over time when conditions of SPR excitation change. All the recorded binding curves in our MOSPR measurements have a slow drift, which is shown in Fig. 2.7a for the representative Co sensor. The reason for this drift is not confirmed yet but it can be due to either the pressure of the holder on the glass slide / prism, or the oil left on the prism surface when changing the samples. This drift can be manually removed to make the curve more explicit, meanwhile keeping the correctness of the data unaffected. It will be fitted with appropriate polynomial functions and subtracted for the binding curves of all the following sensors, just as the one for Co sensor in Fig. 2.7b.

SPR curves are recorded at different moments corresponding to different states of the applied magnetic field  $H$ . Based on the coordinate system in Fig 2.6c, we apply the magnetic field in such a way that the field is firstly applied perpendicular to the plane of incidence in the  $+y$  direction ( $H+$ ), then field is removed ( $H=0$ ); next the field is applied along the opposite direction  $-y$  ( $H-$ ), then field is removed again ( $H=0$ ). From the magnetization point of view, the states are  $M+$ ,  $M_r^+$  and  $M-$ ,  $M_r^-$ , respectively. As it will be discussed later, there is a 'remanence' in the binding curve that is consistent with the magnetization remanence of the Co layer shown in Fig. 2.5a.

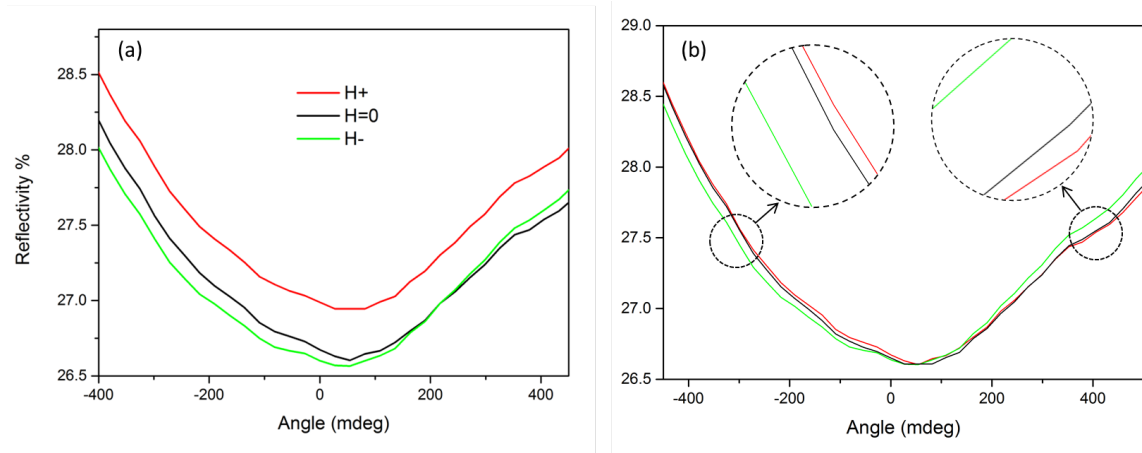


Figure 2.8: (a) SPR curves for Co sensor recorded at three magnetic field states H+, H=0, and H-. (b) Reflectivity minima of H+ and H- are moved to the same position as that of H=0.

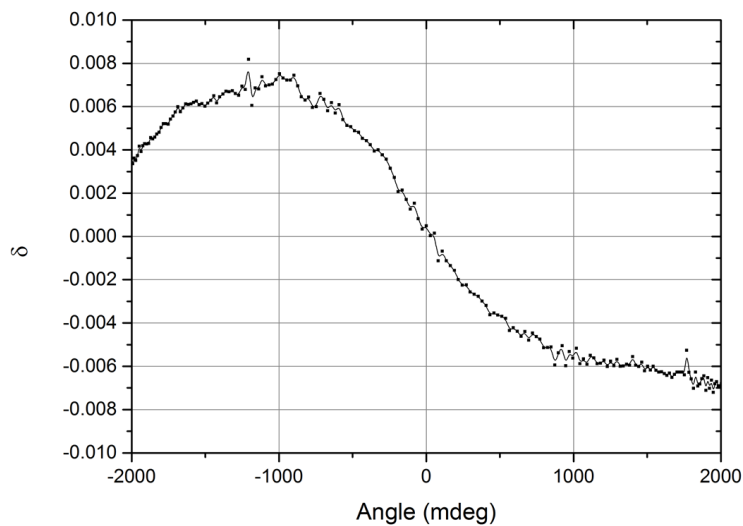


Figure 2.9:  $\delta$  signal for Co sensor

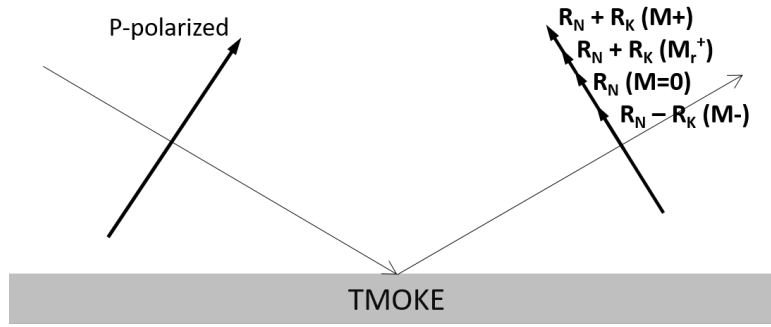


Figure 2.10: Schematic of reflectivity depending on the magnetization in T-MOKE configuration.

We zoom in and look into the dip area of three SPR curves recorded at three consecutive magnetic states of  $H+$ ,  $H=0$  and  $H-$ . Although a  $18\text{ m}^\circ$  shift of angle due to switching magnetic field can be observed from the binding curve, this shift is difficult to recognize in the SPR curves (Fig. 2.8a) since the curves recorded by the software have one point every  $25\text{ m}^\circ$  step, which is too huge for a shift to be observed. The vertical variations of reflectivity curves make it even harder to observe the angle shift. So we shifted the curves so that they have the same minimum amplitude as for  $H=0$ . Despite that the angle shift is still not clear in the dip area, the slope clearly shows the shift responding to the magnetic events (Fig. 2.8b).

It is necessary that the slight difference in the reflectivity amplitude of the three SPR curves be explained. As it has been discussed in Section 1.2.1, for the transverse MOKE configuration, the p-polarized light will generate a Kerr component  $R_K$  in the reflected light. Its polarization is in the same plane as that of the normally reflected component  $R_N$ , and its amplitude vector is proportional to the magnetization  $m$ . So the total reflected intensity is the sum of the two vectorial components, which is shown in Fig.2.10. When the magnetization is  $M+$ , the reflected light has the maximum reflectivity since  $R_K(M+)$  is in the same direction as  $R_N$ . The  $R_K(M_r^+)$  stays in the same direction but with a smaller amplitude than  $R_K(M+)$ . When magnetization reverses, the induced  $R_K(M_r^-)$  has the same magnitude as  $R_K(M_r^+)$  but opposite direction. This could account for the difference of reflectivity in the SPR curves.

Similarly to what was explained in section 1.2.2, we calculate:

$$\delta = \frac{R(H+) - R(H-)}{R(H = 0)} \quad (2.1)$$

in order to enhance the sensitivity of the measurement. The result is shown in Fig. 2.9. The MO effect is strongly amplified when SPPs are excited, which is reflected in an enhancement of  $\delta$ . This is similar to what is presented in literature. As mentioned above, because the data acquisition of the

software does not provide high precision (one point per  $25 \text{ m}^\circ$ ), the enhancement of  $\delta$  signal is not perfectly revealed. In future experiments, the analog signal of the reflected beam intensity will be directly acquired from the rear of the SPR machine.

Next we will investigate the sensors with nanostructured magnetic multilayer. Since these structures have remarkable anisotropy, we measured their MOSPR response along both easy axis and hard axis.

First, it is worth mentioning that although the calculations of thickness of the Au/Multilayer/Au structure have been done with an averaged value of the complex refractive index measured on a  $10 \times$  (TbCo<sub>2</sub> 4 nm/FeCo 4 nm) multilayer, both the 3-layer and 5-layer based structures exhibited a plasmonic resonance, and showed an absorption comparable to the Co based structure.

#### 2.2.4.2 Multi-3 sensor

##### Hard axis

Since the drift in binding curves is always present, we still need to remove it. Fig. 2.11a shows the binding curve for Multi-3 sensor along hard axis, drift removed with polynomial function:  $0.000013x^2 - 0.02306x + 189$ . It can be clearly observed that whenever magnetic field turns to  $H=0$ , a jump of the SPR angle occurs. This jump also exists on the binding curve of Co sensor, albeit in a not quite obvious way. Then according to the binding curve, we select three consecutive numbers that indicate the three magnetic moments  $H+$ ,  $H=0$  and  $H-$  when SPR curves are recorded. In Fig. 2.11b we present the chosen 3-4-5 SPR curves where the minimum of the reflectivity has been levelled. It is still difficult to find the precise minimum position due to too few points on the curves, but on the slopes adjacent to the dip we can notice that curves shift in a similar way as the curves in Co sensor. Again we still can apply the  $\delta = (R(H+) - R(H-))/R(H = 0)$  formula, and this time on four groups of curves shown in Fig. 2.11c. The shape is similar to the one calculated for the Co-sensor. Unfortunately, it is noisier and with a reduced amplitude.

##### Easy axis

Then we made the measurements along the easy axis of the Multi-3 sensor. The binding curve is shown in Fig. 2.12a with drift removed by fitting function:  $-0.0508x + 1960/x - 82.86$ . It is obviously different from the one measured along hard axis. The curve for easy axis exhibits no angle jump whenever the magnetic field turns to  $H=0$  from either  $H+$  or  $H-$ . SPR curves recorded at successive magnetic states and their  $\delta$  signal are also presented here (see Fig. 2.12). The amplitude of the  $\delta$  signal

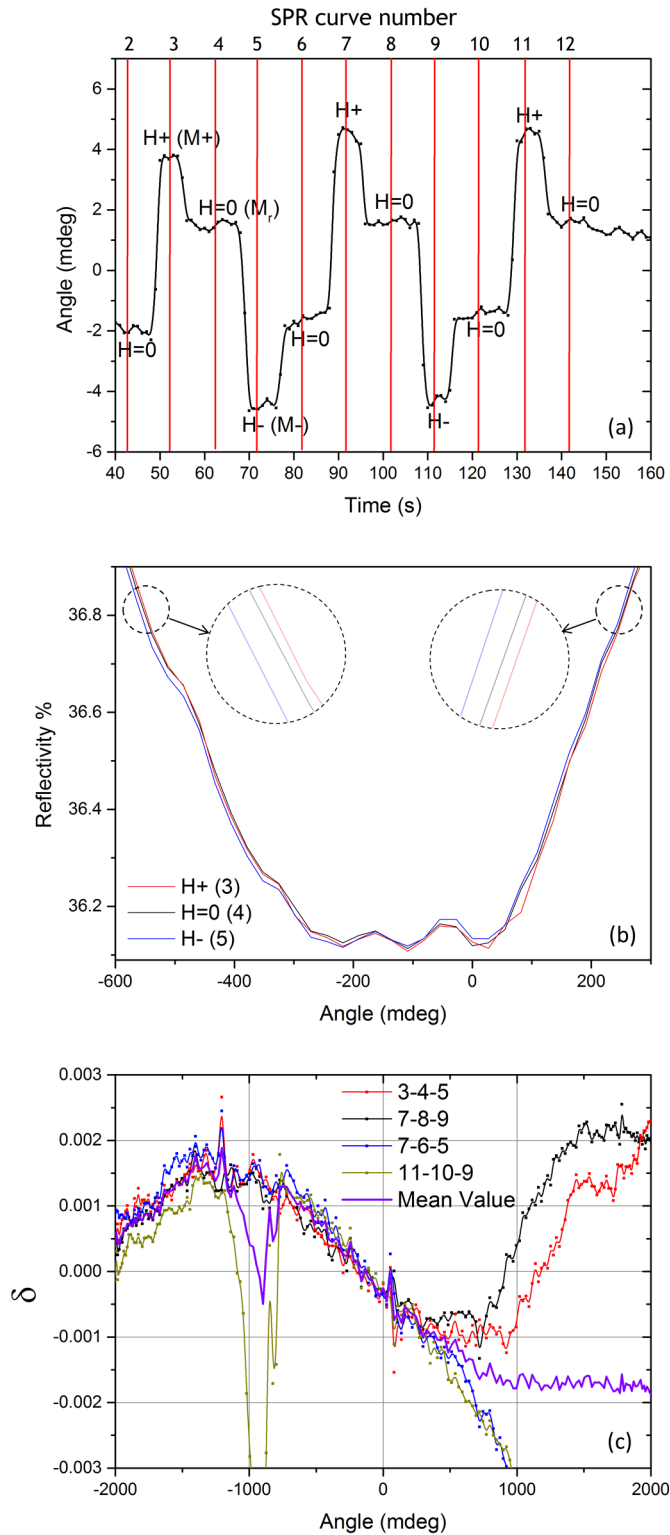


Figure 2.11: Experimental results for Multi-3 sensor along hard axis: (a) Binding curve with drift removed. Numbers on top axis stand for the numbers of recorded SPR curves, corresponding to respective magnetic states. (b) SPR curves of group 3-4-5 with SPR dips moved to the same position. (c)  $\delta$ -signal for 4 groups of SPR curves: 3-4-5, 7-8-9, 7-6-5 and 11-10-9.

is close to the one found on the hard axis.

### 2.2.4.3 Multi-5 sensor

#### Hard axis

The binding curve for Multi-5 sensor along hard axis after removing the drift with function  $0.07418x - 3.478/x + 96.134$  is shown in Fig. 2.13. This time, there is almost no remanence in the binding curve, which is also consistent with a lower magnetization remanence  $M_r$  along the hard axis for this sensor (Fig. 2.5c). (See discussion later).

Again we take 4 groups of SPR curves to apply the formula  $\delta = (R(H+) - R(H-)) / R(H = 0)$ , which is shown in Fig. 2.14. Interestingly, the amplitude is comparable to what was found in the Co-sensor.

#### Easy axis

The binding curve for Multi-5 sensor along easy axis with drift subtracted by the polynomial function  $0.042848x - 137.6/x + 48.245$  is presented in Fig. 2.15a. The behavior is very similar to the Multi-3 sensor along the easy axis. Again, after saturation, the minimum reflectivity angle stays the same when magnetic field is removed.

The calculated value of  $\delta$  for 5 groups of SPR curves is shown in Fig. 2.15c. However, the formula is going to be slightly different from the one used for the Co-sensor or hard axis of the Multi-sensors, due to the fact that there is only two states for the magnetization, and therefore, two states of SPR curves. So the expression becomes

$$\delta = \frac{R(H+) - R(H-)}{R(H+)} \quad (2.2)$$

We can notice that the excursion of  $\delta$  is the same as for the hard axis, and comparable to the Co-sensor.

### 2.2.4.4 Discussion

As evidenced by the binding curves of all these samples, the behavior of the plasmonic response seems to be governed by the magnetization in the magnetic layer according to the phenomenon described in Section 1.2.2, which is the magnetic field induced non-reciprocity effect. As illustrated in Fig. 2.16, if a SPP is propagating along the  $x$  direction, the application of a magnetic field in the  $+y$  direction will cause a shift  $+\Delta k$  in the wave vector ( $k_{spp} = k_{spp}^0 + \Delta k$ ), leading to a shift in the angle of minimum reflectivity in the SPR curve. The reversal of the magnetic field provokes the inversion of the shift:  $k_{spp} = k_{spp}^0 - \Delta k$ ; and thus the opposite shift for the SPR angle.

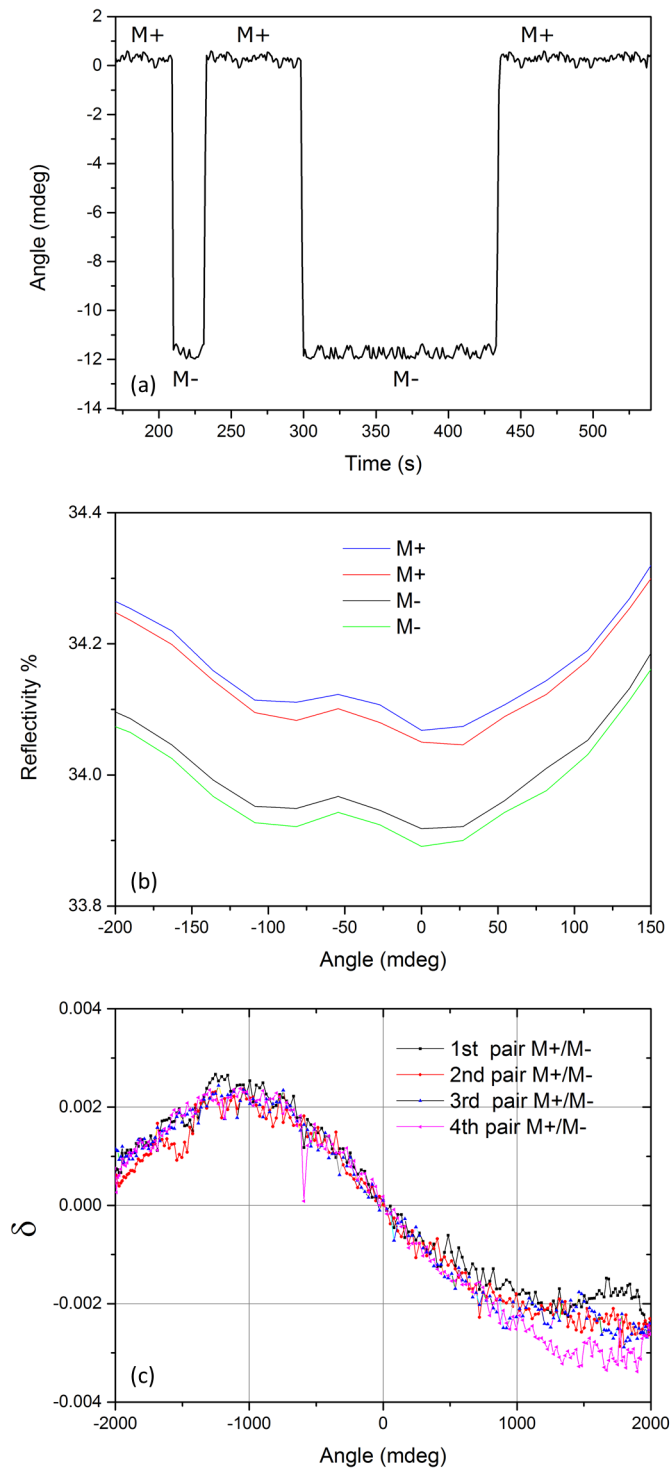


Figure 2.12: Experimental results for Multi-3 sensor along easy axis: (a) Binding curve with drift removed. States of magnetization M+ and M- are indicated. (b) SPR curves corresponding to magnetization M+ and M-. (c)  $\delta$ -signal for 4 pairs of M+/M-.

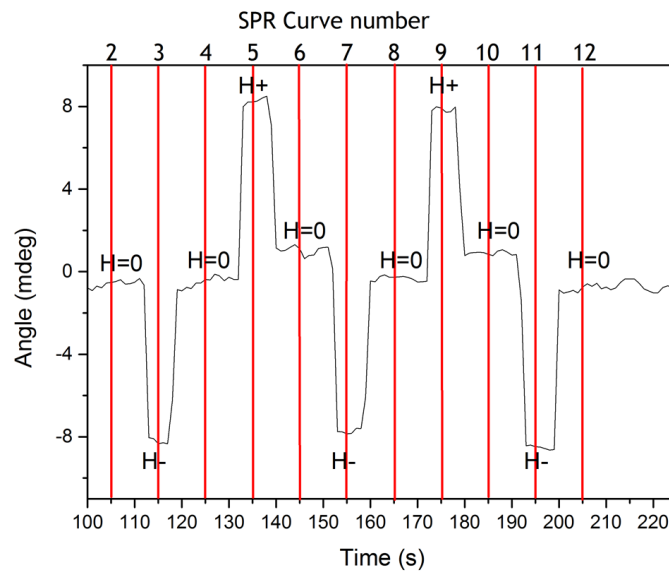


Figure 2.13: Binding curve with drift removed for Multi-5 sensor along hard axis

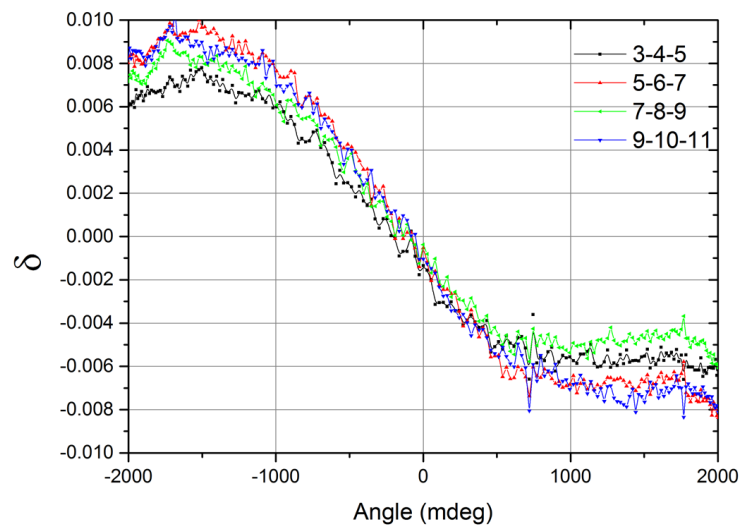


Figure 2.14:  $\delta$  signal for Multi-5 sensor along hard axis.

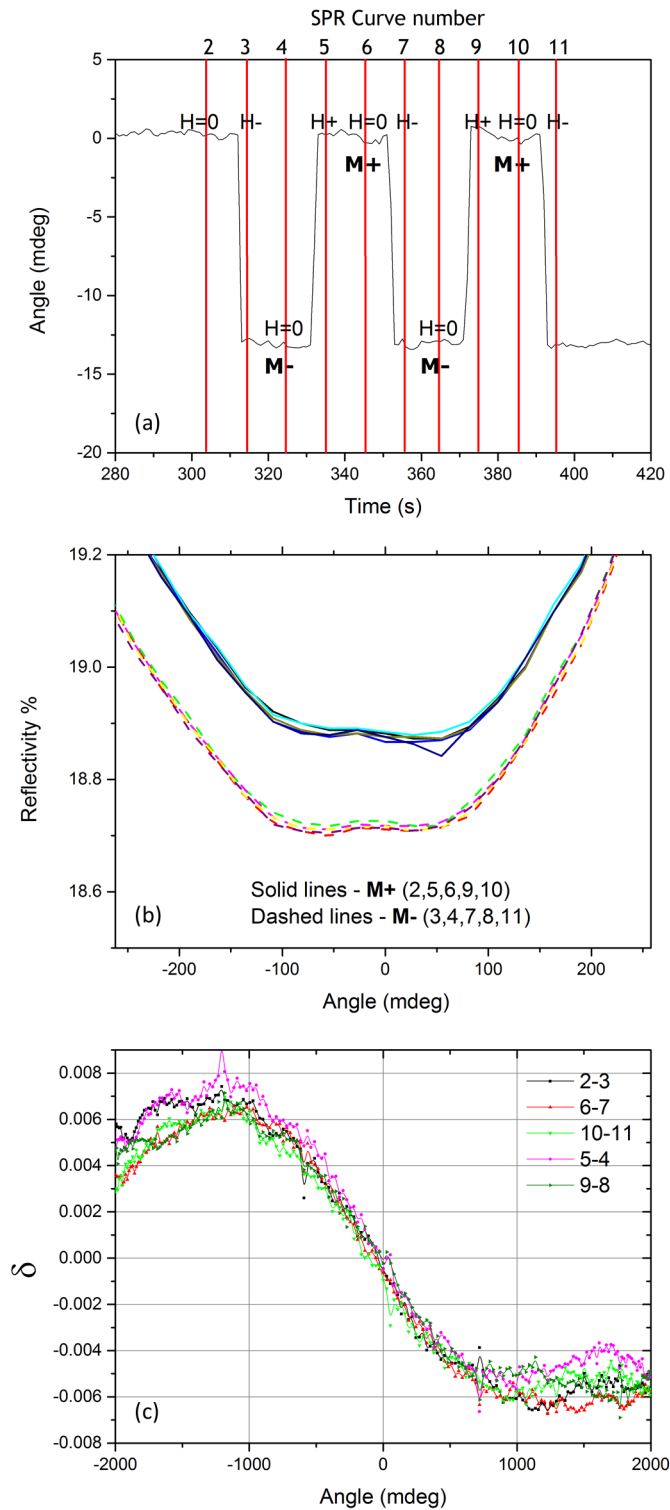


Figure 2.15: Experimental results for Multi-5 sensor along easy axis: (a) Binding curve with drift removed. Magnetic field events and the corresponding states of magnetization  $M+$  and  $M-$  are indicated. (b) SPR curves corresponding to magnetization  $M+$  and  $M-$ . (c)  $\delta$ -signal for 5 groups of  $M+/M-$ .

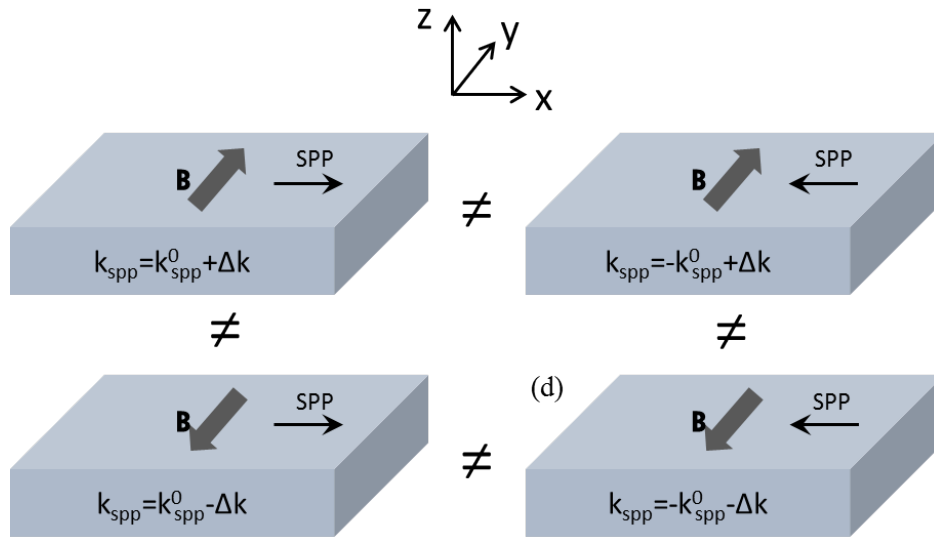


Figure 2.16: SPP non-reciprocity effect induced by magnetic field.

It is actually precise to state that the shift of SPR angle is caused by the change of the magnetization  $M$ , rather than magnetic field  $H$ . From Eq. 1.30, this shift is related to the magnetic field induced modulation of the SPP wave-vector  $\Delta k$ .  $\Delta k$  depends on the off-diagonal (MO) component of the dielectric tensor [1], while the MO component depends on the magnetization  $M$  in Eq. 1.28. So the angle shift is determined by both the magnitude and direction of the magnetization vector  $M$ , more precisely by the magnitude of the  $y$ -component of the magnetization  $M_{ry}$ . This is why, for Co sensor and hard axis of Multilayer sensors, there is a jump of SPR angle on their bindings curve when magnetic field is removed ( $H=0$ ) because there is a change of magnetization in the magnetic materials. This also explains the behaviors in the binding curve of easy axis where there is no jump when magnetic field goes to  $H=0$  since there is no change of magnetization (see Fig. 2.5).

The behavior in case where the magnetic field applied along the easy axis is summed up in Fig. 2.17. When applying the field  $H$ , magnetization  $M$  is saturated along the  $y$  axis, leading to a  $\Delta k_s$  shift. As evidenced by the magnetization loops in Fig. 2.5,  $M$  stays along the  $y$  axis when  $H$  is removed. As it has already been observed in the easy axis of Multi-3 sensor, there is no angle jump in the binding curve when magnetic field turns to  $H=0$ . This can be easily interpreted by the fact that there is only two states of magnetization,  $M+$  and  $M-$ , since  $M_r$  equals to  $M_s$  when  $H=0$ . Thus there are only two values of SPR angles, which can also be proved by the SPR curves. Fig. 2.15b clearly shows that having only two states of magnetization also gives rise to two states of reflectivity, being the  $H+$  with all the  $H=0$  coming from  $H+$  in one state and the  $H-$  with all the  $H=0$  coming from  $H-$  in the other.

When the field is applied along the hard axis, the configuration is the one shown in Fig. 2.18. In

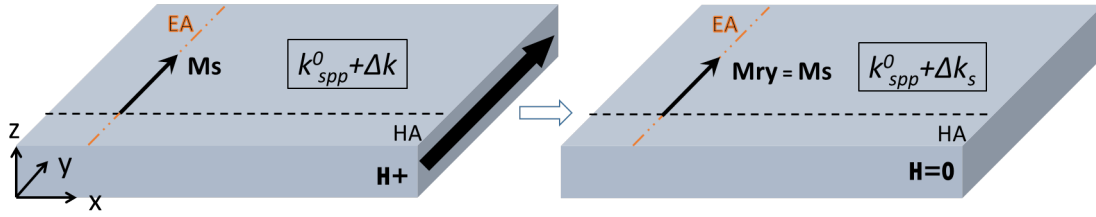


Figure 2.17: Schematic of magnetization configuration when magnetic field is applied along the easy axis.

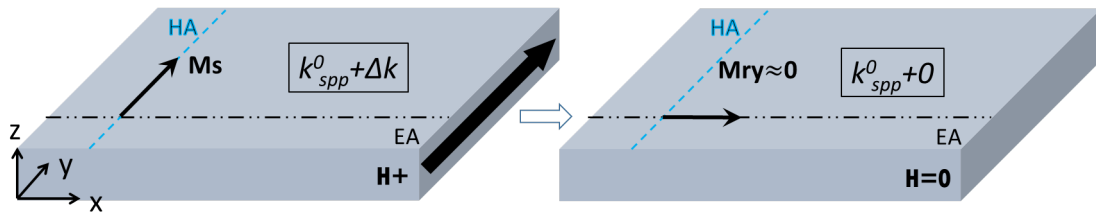


Figure 2.18: Schematic of magnetization configuration when magnetic field is applied along the hard axis.

this case, when the field is removed after saturation, the magnetization rotates back towards the easy axis, leading to no effect on the wave vector  $k_{spp}^0$ . For the Multi-5 sensor, this can be clearly observed from in Fig. 2.13 where the SPR angles at  $H=0$  after  $H+$  or  $H-$  are very close. This is consistent with the very low remanence along the hard axis that was measured in Fig. 2.5c. For the Multi-3 sensor, however, since the easy axis anisotropy is not perfect, the magnetization is not perfectly rotated towards the easy axis when  $H=0$ , leading to a remanent shift in the angle.

This leads us to the third case with Cobalt where there is no easy axis. After saturation, and when  $H$  is removed, a magnetization domain structure takes place in the Co layer, leading to a remanent magnetization  $M_r$  projected along the  $y$  direction (Fig. 2.19).  $M_r$  is lower than  $M_s$ , which leads to an intermediate value of the SPR angles, as it can be seen in Fig. 2.7.

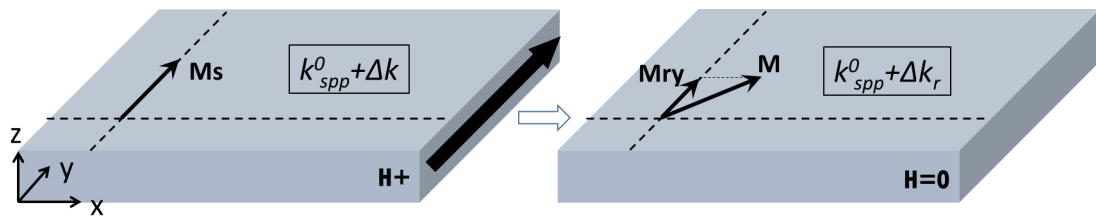


Figure 2.19: Schematic of magnetization configuration for Co-sensor where there is no easy axis anisotropy.

## 2.3 Conclusion

In this chapter, the effects of anisotropic magnetic multilayers on the plasmonic properties were investigated in structures of magnetoplasmonic sensors.

A  $10 \times (\text{TbCo}_2 \text{ 4 nm/FeCo 4 nm})$  multilayer was deposited and its complex refractive index was characterized. Using these data, optimal thicknesses of  $\text{Au/FeCo-TbCo}_2\text{-FeCo/Au}$  and  $\text{Au/FeCo-TbCo}_2\text{-FeCo-TbCo}_2\text{-FeCo/Au}$  SPR structures were calculated. An  $\text{Au/Co/Au}$  structure was also designed for comparison purposes. All the three systems were realized in the IEMN clean room facilities, and the anisotropic character of the magnetic multilayers was evidenced in VSM magnetization loops.

A conventional SPR measurement setup was customized as to be able to apply a magnetic field during SPR measurements. The main results of the MOSPR measurements are:

- It was possible to obtain a surface plasmon resonance in the magnetic Multilayer-based sensors, and they exhibited similar MOSPR signals as the Co-based sensor.
- The uni-axial anisotropic properties of the multilayered magnetic materials were reflected on the plasmonic properties of the sensors.
- There has been an enhancement of MOSPR the signal with the use of  $\delta$ . For the Multi-5 sensor, results were similar to Co-based sensor.

Furthermore, in uni-axial magnetic layers, it has been shown by the AIMAN-FILM group that it is possible to induce a magnetic instability of the Spin Reorientation Transition (SRT) type leading to a huge increase in magnetic field sensibility as well as non-linear effect [106–109]. Following those demonstrations, the possibilities offered by SRT in magnetoplasmonic devices will be studied in the future.

We have seen in this chapter the magnetoplasmonic structures with propagating plasmons, next we will design another magnetoplasmonic structure with localized plasmons.



## Chapter 3

# Plasmonic gold nanoparticles combined with continuous magnetic thin films

In the previous chapter, we have investigated magnetoplasmonic sensing devices with propagating type plasmons (SPPs). In the present chapter, we are now interested in devices having localized type plasmons (LSPs) provided by nanoparticle arrays. Localized surface plasmons can bring about great enhancement of the electromagnetic field in the local vicinity of nanoparticles. In addition, in nanoparticle arrays, the coupling between neighbored dipole plasmons can further increase the field enhancement. This property has been employed to regulate the magneto-optical (MO) activity in nanostructures made out of noble metals and ferromagnetic materials. In these structures, the enhancement of electromagnetic field due to the excitation of LSP has improved the magneto-optical response of the complex system: the ferromagnetic materials provide the MO property, and the noble metals allow the excitation of non-lossy plasmons which enhance the electric field within the ferromagnetic material, therefore resulting in the enhancement of MO activity [110].

Even though measurable MO activity has been demonstrated in nanosized gold disks, it comes at the cost of high applied magnetic field (of the order of 1 T) [110]. However, most systems have been using the combined ferromagnets and noble metals. An enhanced MO activity occurs in a system where arrays of Au nanodisks are fabricated on top of continuous Au/Co/Au trilayers, as a result of the increased intensity of electric field inside Co layer caused by LSP excitation [111]. Au/Co/Au magnetoplasmonic nanodisks have also shown high MO activity and simultaneous low optical loss by the redistribution of electric field inside the nanodisks [80].

In this chapter, a magnetoplasmonic structure consisting of Au nanoparticles and continuous magnetic layers is proposed. We will introduce how the structure will be fabricated, why it is impor-

tant to put a dielectric spacer between the Au nanoparticles and the magnetic layers. We will also measure the effects of the magnetic layers on the plasmonic resonance absorption.

### 3.1 Fabrication of Au nanoparticles

Nanoparticles are prepared on the BK7 glass slides, so first of all, the glass substrates must be cleaned with great care since the particles are at nanoscale. The 7 mm × 20 mm substrates were treated in ultrasound with dichloromethane, acetone and isopropanol, respectively for 5 minutes, followed by the cleaning process with deionized water. Secondly, a Au thin film of 4 nm was deposited onto the glass substrates using thermal evaporation which is preferred compared to e-beam evaporation, as it is more controllable for such a thin layer as 4 nm with thermal evaporation. Finally, rapid thermal annealing (RTA) was carried out at 500°C for two minutes to form the nanoparticles, the SEM image of which is shown in Figure 3.1. The diameters of the particles assembled by the RTA method are clearly not uniform. The distribution histogram shows that the diameters of the particles mostly fall in the range of 20 nm - 25 nm.

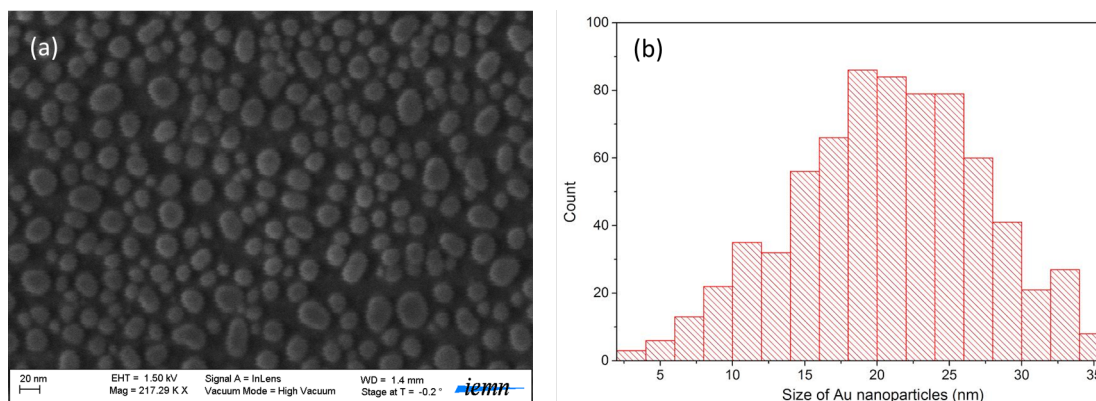


Figure 3.1: (a) SEM image of Au nanoparticles formed by RTA. (b) Size distribution of Au nanoparticles.

### 3.2 Plasmonic properties of Au nanoparticles

The characterization of plasmonic property of Au nanoparticles was performed with ultraviolet-visible (UV-vis) spectroscopy. The equipment used in our characterization is the Lambda 950 UV/Vis/NIR spectrophotometer (PekinElmer Inc.). The spectrophotometer consists of a light source, a diffraction grating in a monochromator or a prism to separate the different wavelengths of light, a holder for the sample, and a detector (Fig. 3.2). It measures the intensity of light passing through a sample ( $I$ ), and compares it to the intensity of light before it passes through the sample ( $I_0$ ). The ratio

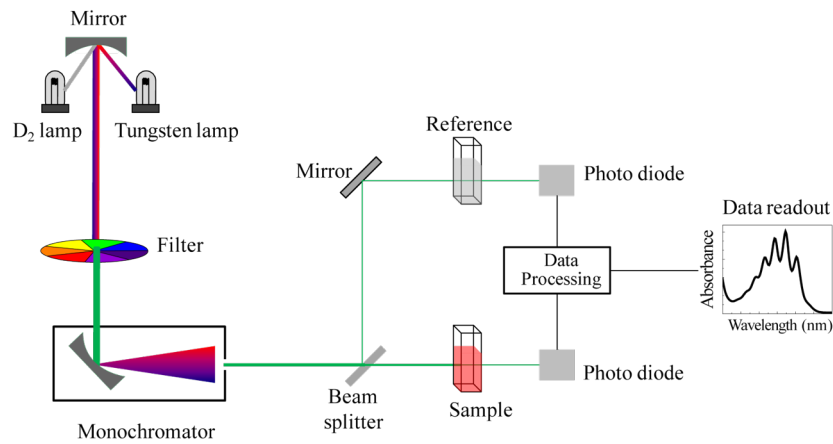


Figure 3.2: Schematic of UV-vis spectrophotometer

$I/I_0$  is called the transmittance  $T$ . The absorbance,  $A$ , is based on the transmittance:  $A = -\log T$ . The UV-vis spectrophotometer can also be configured to measure the reflectance of opaque samples, where the spectrophotometer measures the intensity of light reflected from a sample ( $I$ ), and compares it to the intensity of light reflected from a reference material ( $I_0$ ). The ratio  $I/I_0$  is called the reflectance  $R$ . Both absorbance and reflectance are usually expressed as percentage %. Here for the Au nanoparticles on glass substrates, we measure the absorbance instead of reflectance as the samples are transparent.

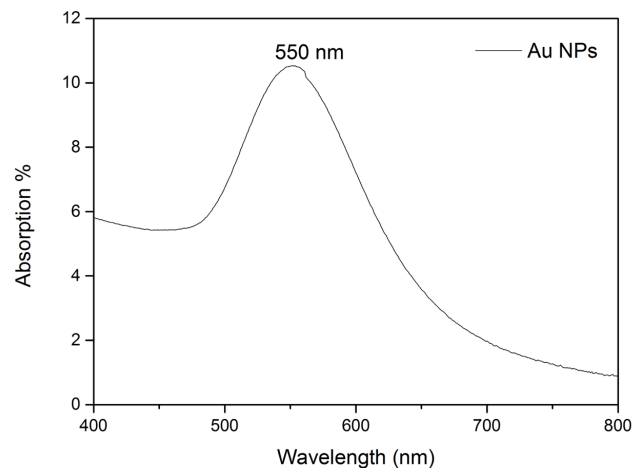


Figure 3.3: Absorption spectra of Au nanoparticles

The recorded absorption spectrum of Au nanoparticles is shown in Fig. 3.3 where the resonance wavelengths is 550 nm. The Au nanoparticles formed by RTA method show a well-defined LSPR peak.

### 3.3 Magnetoplasmonic structures based on Au NPs

Now that we have Au nanoparticles to provide the plasmonic resonance, a simple method to construct a magnetoplasmonic structure is to put a layer of magnetic directly on top of Au NPs. The magnetic materials we want to apply are the commonly used Cobalt, and the nanostructured multilayers with tailored magnetic anisotropy as the ones used in chapter 2 in MOSPR experiments.

#### 3.3.1 Protection test

It is well known that these magnetic materials are subjected to oxidation. So a protection test was carried out because if cobalt get oxidized after a certain amount of time, we will need an extra ultra-thin Titanium layer (2~3 nm) to protect cobalt from being destroyed. The testing samples were prepared by RF sputtering using a rotary turn table in the Leybold Z550 equipment. In order to find the optimal recipe to deposit a layer of 2~3 nm Titanium, a calibration of deposition rates based on different sputtering configurations was done, as shown in Table 3.1

Table 3.1: Calibration of deposition rates of Ti based different sputtering configurations. The calibration is made at 1rpm.

Mode	Magnetic field	Position	Deposition rate
Dynamic	$H \neq 0$	1	7.5 nm/osc
	$H = 0$	2	7.5 nm/osc
Static	$H = 0$	3	1.77 nm/sec

To put such a thin layer of Ti, one has to deal with the difficulty coming from the fact that the Ti target is 6-inch in magnetron sputtering. This usually provides high sputtering speeds, which makes the ultra-thin deposition more challenging. Therefore we need to investigate both the static and dynamic modes of the sputtering machine to find the best option. According to the calibration table, for the static mode, it takes about 2 seconds to obtain the expected thickness of Ti. But it is demanding to manipulate the sputtering machine to deposit the required thickness in such a short time period. The dynamic mode, however, provides better precision in controlling the sputtering. Accordingly, the dynamic (oscillatory) mode without magnetic field is employed. Since we have the rate of 7.5 nm/osc at 1rpm, substrate rotating faster will end up in thinner layers because of its proportionally reduced time under the target. Hence, a 2.5 nm thick layer deposited at 3rpm can be achieved. As for the mode with magnetic field, we utilized it to deposit layers with magnetic anisotropy. The deposition was made under a magnetic field generated by permanent magnets in order to induce a magnetic

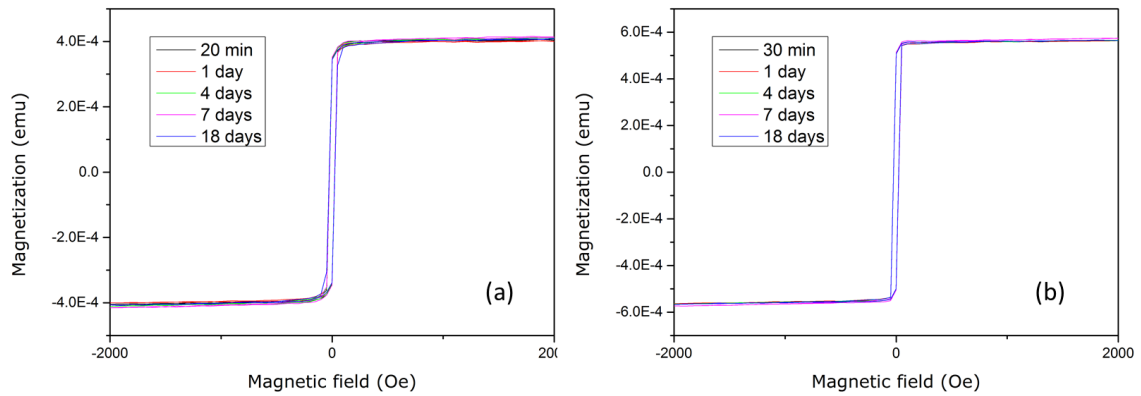


Figure 3.4: VSM measurements for Ti protection test. Five curves show the magnetization loops after 20min, 1 day, 4 days, 7 days and 18days for the sample without (a) and with (b) Ti protection, respectively.

easy axis (EA). This is for further investigation on the effect that magnetic anisotropy can have on magneto-optical activity.

Then we prepared two Co samples with and without Titanium layer on top. The VSM measurement was performed on different dates to see if there is any change in the magnetization. Thus we are able to make the comparison by studying the evolution of magnetization over time to evaluate the effectiveness of Ti protection.

For samples without protection, the VSM results of barely unchanged hysteresis loops indicate that the Co layer seems intact during 18-day exposure in air. That is because at room temperatures, it reacts very slowly with air. For samples having protection, the stable curves over time suggest that the protection is effective (Fig. 3.4). If the following characterizations can be done within 18 days, then the extra protection layer won't be necessary. If not, the Ti layer would come in handy.

### 3.3.2 Direct deposition of magnetic layers

We deposited magnetic layers directly on top of Au NPs and made the plasmonic characterization without Ti protection. We put Co layers with thickness of 5 nm, 10 nm and 15 nm, and a nanostructured FeCo/TbCo<sub>2</sub>/FeCo layer with 5 nm thickness. The absorption spectra of these magnetoplasmonic structures are shown in Fig. 3.5, where the plasmonic resonance disappears.

This can be explained by Fröhlich condition (Eq. 1.19). The resonance occurs only under the condition  $\text{Re}[\varepsilon(\omega)] = -2\varepsilon_d$ , where  $\text{Re}[\varepsilon(\omega)]$  is the real part of the Au permittivity and  $\varepsilon_d$  is the per-

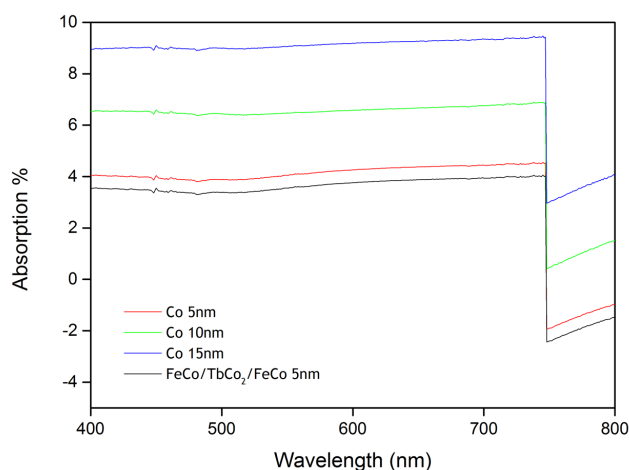


Figure 3.5: Absorption spectra of magnetoplasmonic structures with magnetic layers directly deposited on top of Au NPs.

mittivity of the material surrounding Au NPs. At UV-vis frequencies metals have negative real part of permittivity, so the resonance condition can not be satisfied by two adjacent metals.

### 3.3.3 Dielectric spacer

Therefore we need to put a dielectric layer between two metallic layers to bring the LSPR back because the permittivity of a dielectric is positive in optical range. The dielectric in our case is silicon oxide ( $\text{SiO}_2$ ) and we put a layer of 4 nm  $\text{SiO}_2$  on top of Au NPs.

As it has already been observed from Figure 3.5, there is no sign of plasmonic resonance when a magnetic layer was put directly on top of Au nanoparticles. After inserting a  $\text{SiO}_2$  spacer in between, however, the resonance peak appears again, together with a spectral red-shift to 565 nm due to the change in surrounding refractive index, as shown in Fig. 3.6a. This is one typical demonstration of bulk refractive index (RI) sensing based on the LSPR-type Au nanoparticles.

Then we continued to put magnetic layers on top of  $\text{SiO}_2$  layer so that the magnetoplasmonic architecture is constructed. The magnetic layers sputtered onto  $\text{SiO}_2$  are the same as the direct deposition where the thickness of Co layers are 5 nm, 10 nm and 15 nm, and the nanostructured FeCo/TbCo<sub>2</sub>/FeCo layer is 5 nm. Fig. 3.6a shows the absorption spectrum of one sample with 5 nm Co, exhibiting a further red-shift to 595 nm. This can be due to the interaction of Co layer with  $\text{SiO}_2$  layer that creates a compound dielectric environment with a higher effective refractive index. The resonance peaks of the remaining magnetoplasmonic structures are all shifted to 595 nm regardless

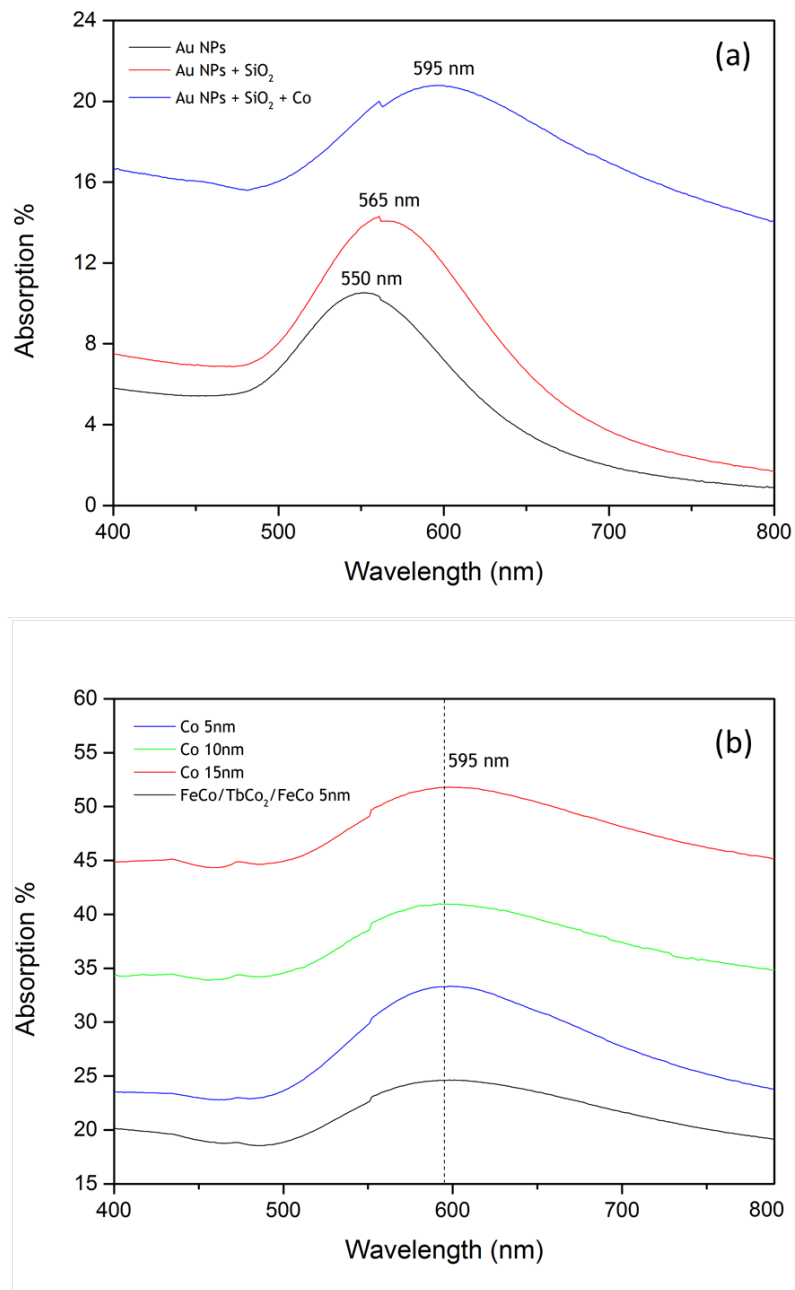


Figure 3.6: (a) Evolution of absorption spectra for Au NPs, Au NPs with SiO<sub>2</sub> layer, Au NPs with both SiO<sub>2</sub> and 5 nm Co layers. (b) Absorption spectra for structures with different thickness of Co and FeCo/TbCo<sub>2</sub>/FeCo.

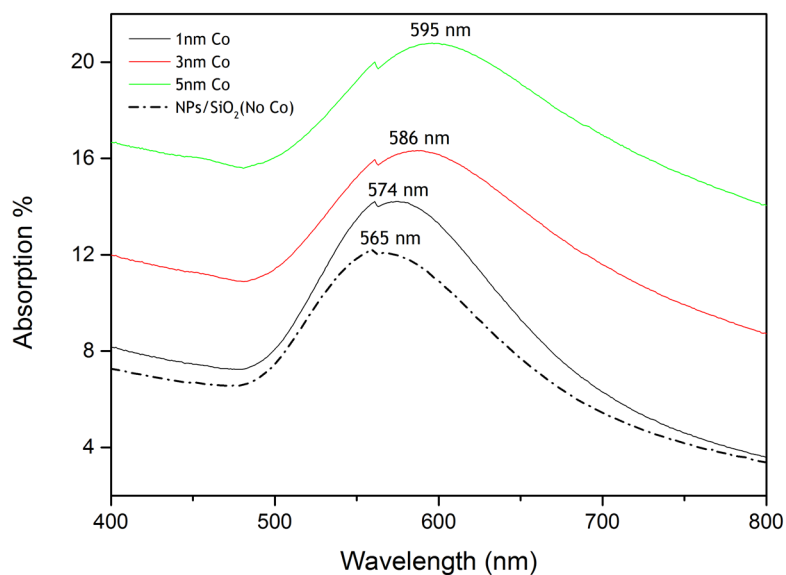


Figure 3.7: Absorption spectra of structures with Co layer thickness of 1 nm, 3 nm and 5 nm.

of the type and thickness of magnetic materials, and 5 nm is the maximum thickness for peak shifting to 595 nm (Fig. 3.6b).

Apart from the spectral red shift, another obvious evolution of the absorption spectra is that the peaks become broader as more layers are deposited on Au NPs. In particular, when magnetic layers are put on, the peak becomes significantly broader than pure Au NPs for the reason that magnetic materials have a high optical loss. Moreover, for structures with Co layers, 5 nm Co has a sharper peak than 10 nm and 15 nm, while the latter two have the same shape. The spectrum curve of 5 nm Co is more sharpened than that of the same thickness of FeCo/TbCo<sub>2</sub>/FeCo. This is because the nanostructured multilayer has more optical loss than Co.

### 3.3.4 Thickness effects of magnetic layers

For the magnetic layers, since 5 nm is the maximum thickness for spectral shift to 595 nm, it is necessary to investigate how the thickness varying within 5 nm can affect the absorption spectra. So we prepared three samples with Co layer of 1 nm, 3 nm and 5 nm, respectively and performed the UV-vis spectroscopy.

Their absorption spectra are shown in Fig. 3.7. Obviously the absorption spectra depend on the thickness of Co layer when the thickness is below 5 nm. As the thickness of Co layer increases, the

spectra exhibits red shifts. This means that the effective refractive index (permittivity) of the composite  $\text{SiO}_2$  - Co has increased. The reason for this behavior is that the optical constants of multilayers in nanoscale thickness depend on the thickness.

### 3.4 Conclusion

In this chapter, we proposed and studied a magnetoplasmonic structure consisting of Au nanoparticle arrays and continuous magnetic layers. The obtained results of the chapter can be summarized as follows:

- First, Au nanoparticle arrays were fabricated by rapid thermal annealing, a method that is proven to be very simple and low-cost technique compared to the complicate and expensive lithography process. The well-defined LSPR peak of the Au nanoparticles also proves this method very effective.
- Then we constructed magnetoplasmonic structures through the deposition of ferromagnetic layers on top of the Au nanoparticles. It has been evidenced that a dielectric layer in between Au nanoparticles and ferromagnetic layers was necessary in order to preserve the plasmonic resonance. The magnetoplasmonic structures showed the Co-thickness dependent property which therefore can be actively modified.

The next steps would be the measurements of magneto-optical spectroscopy for these structures. Although the MO spectroscopy setup is not available for now, it can be inferred that the MO effect would have an enhancement due to the excitation of LSPR. And the effect of anisotropy of nanostructured FeCo/TbCo<sub>2</sub> layers on MO activity will also be investigated in the future.



## Chapter 4

# Nanoporous alumina matrix coated by magnetoplasmonic layers

### 4.1 Introduction

Nanoporous structures based on anodic aluminum oxide (AAO) have been intensively studied on their optical response that can be tuned by modifying the AAO geometry (i.e. pore diameter and its length) [112], and their applications in sensitive and selective biosensors [97]. Song *et al* studied the properties of the porous structure Ag/CoFeB/Ag prepared by the nanosphere-assisted technique [99]. Then Pr. Song proposed another hybrid nanoporous structure by depositing magneto-plasmonic layers Ag/ITO/CoFeB/ITO/Ag onto AAO substrates.

In this chapter we will characterize the properties of this magneto-plasmonic nanoporous structure. Samples with different pore diameters will be prepared. We will investigate the magnetic property through VSM measurements. The optical property will be assessed by measuring the reflective interference spectroscopy (RIfS) signal that is unique for nanoporous structures. The magneto-optical properties will also be studied by a Kerr effect magnetometer to see how the pore size and plasmonic resonance can have an effect on the MO response, which is promising to be used in biosensing applications.

## 4.2 Fabrication and structures

The self-ordered AAO can be described as a nanoporous alumina ( $\text{Al}_2\text{O}_3$ ) matrix with arrays of periodically arranged cells containing a cylindrical pore on Al substrate. The nanopores are formed perpendicularly to the surface of underlying Al substrate. A two-step anodization process has been considered as the standard technique to prepare nanoporous AAO. The AAO substrates we used were purchased from Shangmu Technology Co. Ltd.

The nanoporous magnetoplasmonic structures consisting of noble metal (Ag), high conductive Indium Tin Oxide (ITO) and ferromagnetic material (CoFeB) are prepared by a multi-step magnetron sputtering physical vapor deposition method. The method has the advantages of having a wide deposition range, less increase of substrate temperature and a good film-to-substrate adherence. The Ag and ITO layers were sputtered in a 15 mT Ar gas atmosphere using the dc-sputtering with the power of 50 W, while CoFeB layer was deposited on in a 0.75 mT Ar environment using the rf-sputtering with the power of 100 W.

We intended to investigate a series of samples with different pore sizes as well as varying thickness of layers. Samples are divided into 4 groups according to the AAO substrates' pore diameters: 30 nm, 55 nm, 65 nm and 200 nm. Each group contains samples with varying thickness of ITO layer while the other layers keep thickness unchanged. The grouping list is shown in Table 4.1.

Table 4.1: A series of samples grouped according to 4 diameters of AAO. Each group contains samples with different layers and thickness. All units are in *nm*.

Diameters of AAO pores	Thickness of multilayers
30	Ag (5) / ITO (5) / CoFeB (10) / ITO (5) / Ag (5)
65	Ag (5) / ITO (10) / CoFeB (10) / ITO (10) / Ag (5)
200	Ag (5) / ITO (15) / CoFeB (10) / ITO (15) / Ag (5)
	Ag (5) / ITO (20) / CoFeB (10) / ITO (20) / Ag (5)
55	Ag (5) / CoFeB (10) / Ag (5)
	Ag (5) / ITO (10) / CoFeB (10) / ITO (10) / Ag (5)

To obtain the surface images of these samples, we make use of the scanning electron microscope (SEM). Fig. 4.1 presents the SEM images of surfaces of AAO substrates before and after deposition of Ag/ITO/CoFeB/ITO/Ag layers. The direct consequence that follows the deposition of multilayer is the decreasing size of nanopores. This is attributed to the accumulations of layers of material both

Table 4.2: Diameters of nanopores before and after deposition of multilayers, and the averaged distance between pores.

<b>Before deposition</b>	<b>After deposition</b>	<b>Inter-pore distance</b>
30	20	60
55	45	100
65	55	100
200	170	450

on the walls of neighbored pores and on the edges of pores. Another morphologic modification by the deposition is that the flat walls become like ridges due to the piling up. The measured diameter changes together with averaged pore-to-pore distance are listed in Table. 4.2. The unaltered inter-pore distance is understandable.

### 4.3 Characterization of samples

We made the characterizations on all the samples and we will look into the effects of pore size and layer thickness on the magnetic, optical and magneto-optical properties of these samples.

#### 4.3.1 VSM measurements

The magnetic properties of the nanoporous samples were characterized by vibrating sample magnetometer (VSM). The magnetization curve of one representative sample is shown in Fig. 4.2a. An obvious ferromagnetic property can be seen due to the existence of magnetic component CoFeB. There is no anisotropy in the surface plane as the magnetization loops along the X axis and Y axis of the rectangular sample have negligible difference.

All the samples have the same thickness of CoFeB layers (10 nm), but their surface areas ( $\text{mm}^2$ ) are slightly different from each other. So we will evaluate the "surface magnetization" which is the magnetization divided by the surface area. The surface magnetization of all samples is shown in Fig. 4.2b. Samples in the same size group have identical loops with an exception for 45 nm group because one sample in this group have no ITO layer. This suggests that ITO layer may exert an effect on the magnetic property. As for the minor disparity in group 170 nm, chances are that the deposited thickness of CoFeB layer is not perfectly equal, making the difference too trivial to be considered.

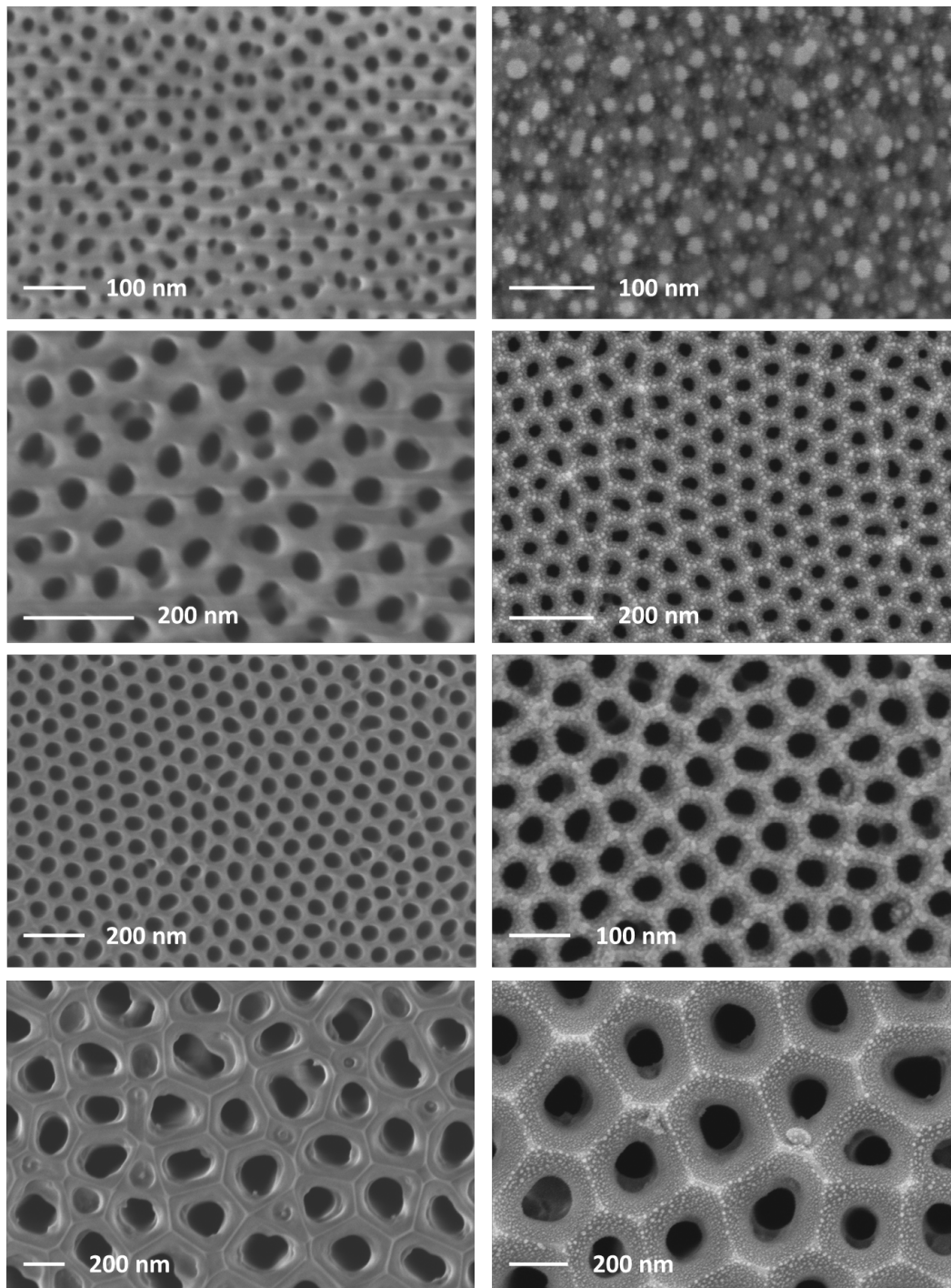


Figure 4.1: SEM images: surfaces of bare AAO substrates (left column) and surfaces after deposition of multilayer Ag/ITO/CoFeB/ITO/Ag (right column). Four rows from top to bottom correspond to four groups of different nanopore diameters.

We made the same VSM measurements after two years, and compared the results with the previous ones in Fig. 4.2c. Lower magnetization in the latest measurement can be noticed, and it is most likely due to the oxidation of the magnetic layer over time.

### 4.3.2 Reflectivity measurements

The optical characterization was performed with the universal reflectance accessory (URA) module equipped in the Lambda 950 UV/Vis/NIR spectrophotometer, which allowing accurate measurement of specular reflectance over a substantial range of angle of incidence between 8 and 68 degrees and a wide range of wavelengths from 190 to 3100 nm. We measured all the samples at 8° angle of incidence with light wavelength ranging from 200 nm to 800 nm. The schematic of URA operating at 8° is presented in Fig. 4.3.

Typical reflective interference spectroscopy (RiFS) signal with Fabry-Perot interference fringes were obtained for these hybrid nanoporous samples. It is the fringes with well-defined peaks that are useful for sensing applications where the shift of peaks is detected. The interference signal defined by the number of fringes and their intensity (amplitude) is considered to depend on pore parameters. We will discuss how the pore structures exert impact on the RiFS properties.

Fig. 4.4 presents the RiFS signals from the group of 20 nm pore diameter. A noticeable spectral red-shift is observed by increasing the thickness of ITO layer, which can be interpreted by Eq. 1.35 (see section 1.3). Under a constant refractive index, variations in porous length  $L$  will lead to  $\lambda$  spectral shift. However, the trend of red-shift due to increasing pore depth breaks off starting from the fringe around 550 nm. It is also can be seen that for an individual thickness of ITO layer the interval between adjacent fringes tends to become wide towards longer wavelengths, due to the inverse proportional relationship between  $m$  and  $\lambda$ , that is, with  $m$  equidifferently decreasing towards longer wavelengths the interval  $\Delta\lambda$  radically increases. In addition, as the ITO thickness is slightly building up, the RiFS signal experiences marginal decrease both in the intensity (amplitude) of fringes and in the relative reflectivity. This can be attributed to increased absorption by ITO and multiple reflections. The results for groups of 45 and 55 nm are similar to those of 20 nm (not shown here), whereas for group of 170 nm, interference disappears (see below).

Pore diameter also plays an important role in RiFS response. Fig. 4.5 presents RiFS patterns of 4 samples selected from each group with different pore diameters but same multilayer thickness. A significant decrease in the number of fringes is observed with increasing pore diameter. The amplitude of the fringe tends to have a tendency in a similar way. The decreased number of fringes can be

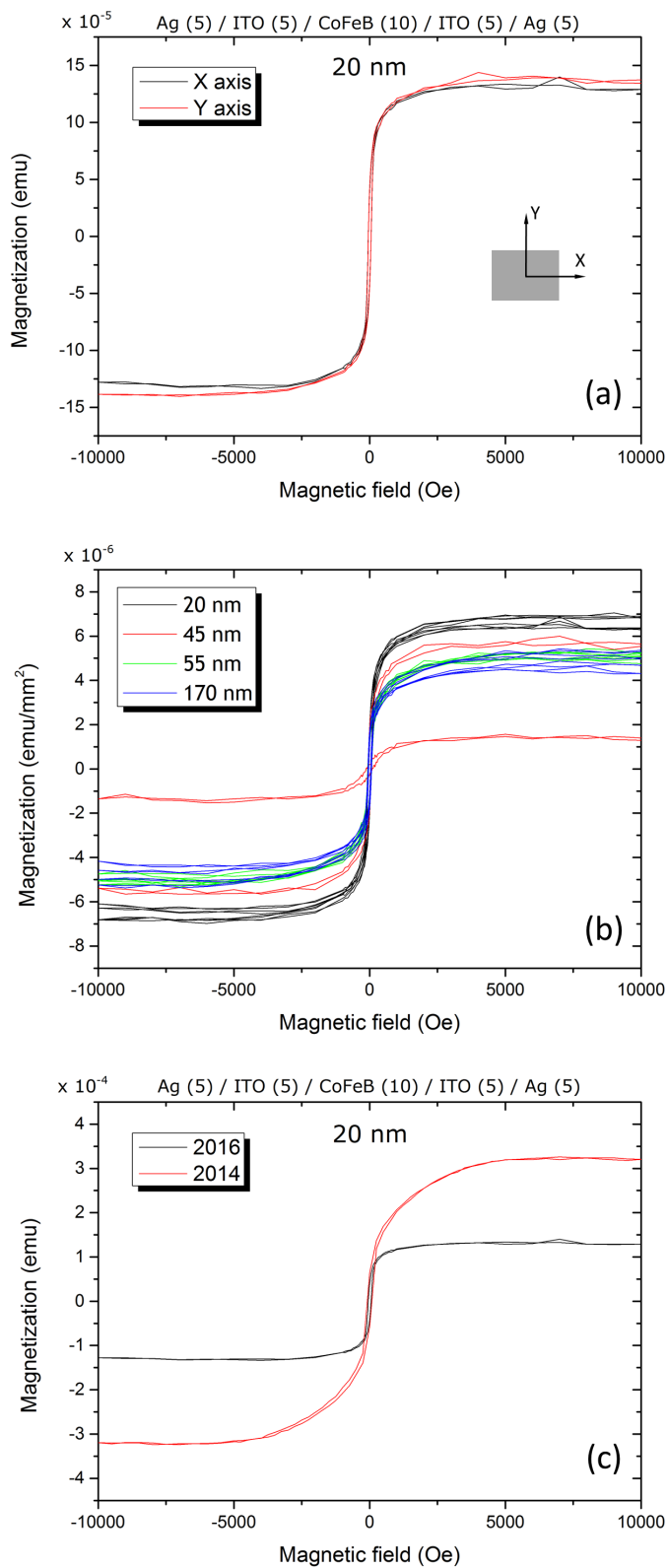


Figure 4.2: Curves of VSM measurements for nanoporous samples: (a) Magnetization loops for sample with 20 nm pore diameter and 5 nm ITO along two axis. (b) Surface magnetization loops for all samples. (c) Magnetization loops for the same sample with 20 nm pore diameter and 5 nm ITO measured in 2014 and 2106.

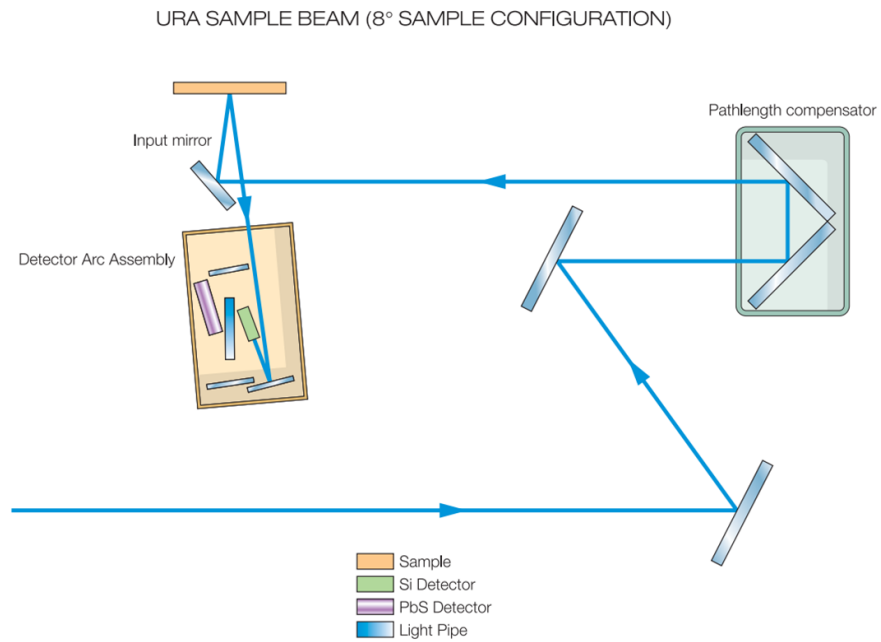


Figure 4.3: The URA sample measurement configuration at  $8^\circ$ .

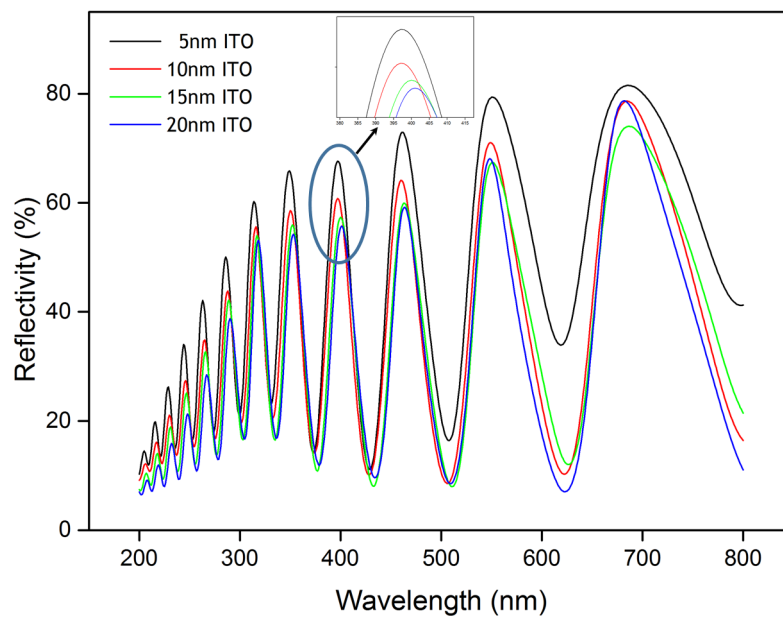


Figure 4.4: Fabry-Perot interference spectrum for 20 nm-pore-diameter samples with different thickness of ITO layer. Inset: spectral shift and change in relative reflectivity of RIFS signal for one specific order of fringe.

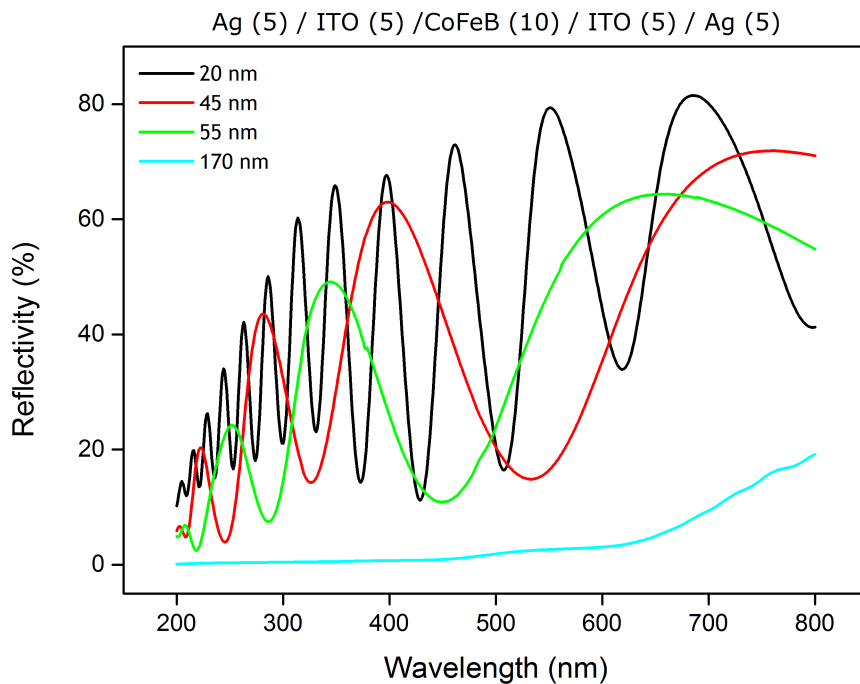


Figure 4.5: Fabry-Perot interference spectrum for different-pore-diameter samples with the same multilayer components.

explained by the decrease in the number of light rays reflected at two interfaces that give rise to the interference. From sensing point of view, the intensity of the fringes is more crucial than the number of them. A higher spectral shift in the RfS signal thus giving a higher sensitivity is anticipated for refractive index sensing by nanopores with smaller diameters than those with larger diameters. The sharper fringes produced by smaller nanopores also give them major advantages to get good sensing performance. As mentioned above, a fringeless spectrum appears for 170 nm pore diameter in the wavelength range of 200 nm - 800 nm. Also, the reflectivity is very low, even goes down to zero in the range of below 500 nm.

It can be concluded that the RfS spectra of nanoporous Ag/ITO/CoFeB/ITO/Ag structure depend on both pore length (multilayer thickness) and pore diameter. But it is noteworthy that it is a synergic effect that the structural parameters have on the reflectance properties. Understanding of this will encourage us to optimize the nanoporous structures considering the combined instead of separate contribution when dealing with sensing applications.

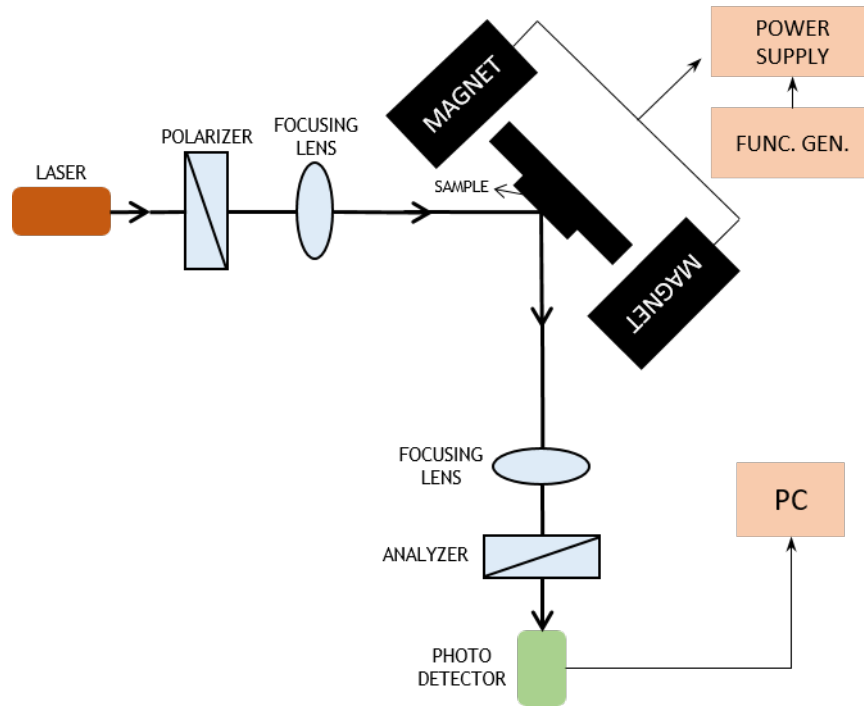


Figure 4.6: Schematic block diagram of L-MOKE magnetometer setup.

### 4.3.3 Kerr effect measurements

We studied the magneto-optical activity of these nanoporous samples using the MOKE magnetometer to collect Kerr rotation information in the form of hysteresis loops. The principles of the MOKE magnetometer based on the Kerr effect are explained in Chapter 1. Fig. 4.6 shows the schematic of the L-MOKE setup in AIMAN/FILMS. Incident light is provided by a He-Ne laser with wavelength 623 nm at an incident angle of  $45^\circ$ . The polarization of the light before reflection is controlled by a polarizer to be s-polarized, which is then focused onto the sample by a lens. The measured area of the sample depends on the size of the laser spot which is approximately 1 mm in diameter. The reflected light beam passes through an analyzer into a photo-diode detector, where the reflected intensity is measured. The pair of magnets consisting of Helmholtz coils generates the sweeping magnetic field from -600 Oe to 600 Oe. The programmed software on PC simultaneously sweep the magnetic field and recorded the reflected intensity as a function of the applied magnetic field. All components are mounted onto an anti-vibration optical table.

L-MOKE rotations for 4 groups of samples were collected by this L-MOKE magnetometer setup. As it can be observed in Fig. 4.7, the most striking phenomenon is the reverse of sign in the MOKE magnetization loops when comparing the results obtained from nanoporous magnetoplasmonic structures with different pore sizes. This result is analogue to the findings in [81] where the sign reversal of MOKE loops occurs in the Ni nanodisks structure.

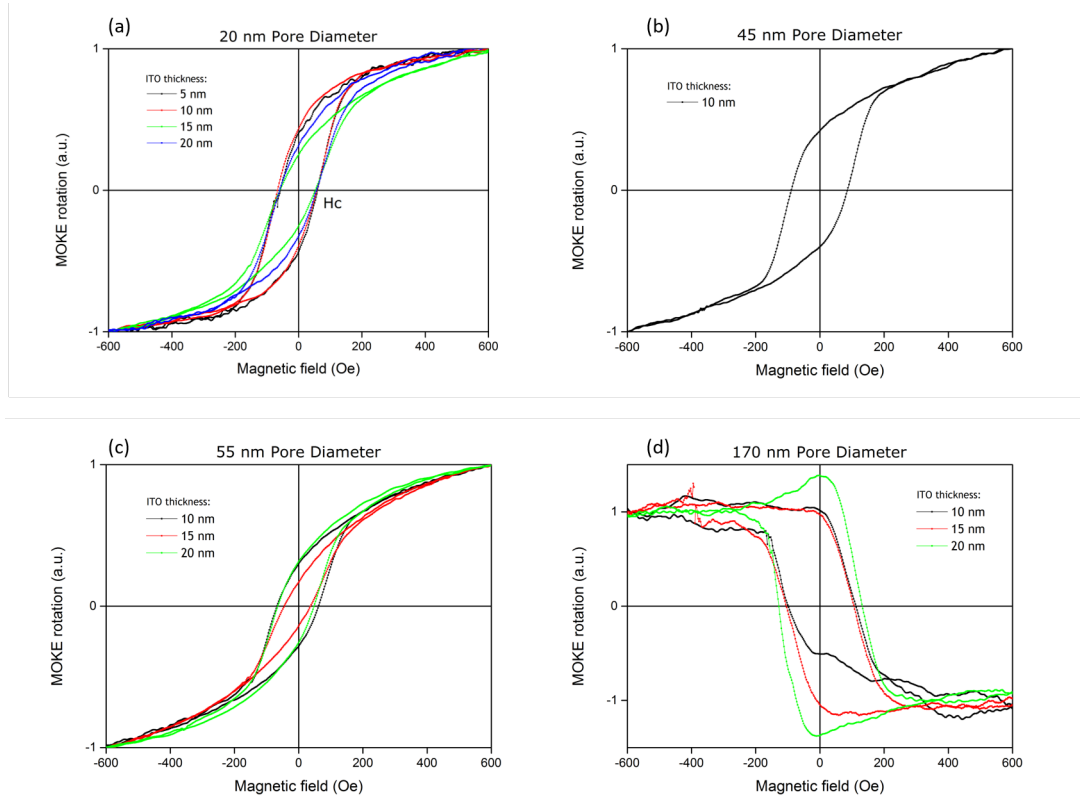


Figure 4.7: MOKE Hysteresis loops of the nanoporous Ag/ITO/CoFeB/ITO/Ag samples .

Let us introduce the physical principles for the MO response in magnetic nanodisks structures. In bulky ferromagnetic structures and continuous films, the MO response is determined by the spin-orbit interaction which is an intrinsic property of ferromagnetic materials. However, for magnetic nanodisks, the MO activity is governed by localized surface plasmons as well. We exemplify the underlying physics adopting P-MOKE configuration with normal incident electric field along  $x$  axis (Fig. 4.8a). The electric field  $E_{x0}$  in the incident light induces an electric dipole:

$$p_x = \alpha_{xx} E_{x0} \quad (4.1)$$

along the  $x$  axis, where  $\alpha_{xx}$  is the diagonal component of the electric polarizability tensor. The resulting oscillation of electrons along  $x$  direction is coupled with the magnetization aligned in  $z$  direction. This will induce another oscillation motion of electrons along the  $y$  axis (This can also be explained by Lorentz force theory discussed in Chapter 1). The corresponding electric dipole is

$$p_y = \alpha_{yx} E_{x0} = \frac{\epsilon_{yx} \alpha_{yy} \alpha_{xx}}{(\epsilon_{ii} - \epsilon_m)^2} E_{x0} \quad (4.2)$$

where  $\alpha_{yx}$  is given by the off-diagonal polarizability tensor components  $\alpha_{ij} = \epsilon_{ij} \alpha_{ii} \alpha_{jj} / (\epsilon_{ii} - \epsilon_m)^2$ ,  $i, j = x, y, z$ .  $\epsilon_{ii}$  and  $\epsilon_{ij}$  are the diagonal and off-diagonal components of the dielectric tensor, and  $\epsilon_m$  is the permittivity of the surrounding media. Therefore, when the ferromagnetic nanodisks are

subjected to external magnetic field, incident light will induce two LSPs: one is directly excited by electric field of the incident light, the other is induced perpendicularly by spin-orbit coupling. If the surface shape of nanodisks is considered to be circular, then we have  $\alpha_{xx} = \alpha_{yy}$  (two LSPs resonate at the same wavelength) and the expression for  $y$  electric dipole turns to  $p_y = \alpha_{yx}E_{x0} = [\epsilon_{yx}\alpha_{xx}^2/(\epsilon_{ii} - \epsilon_m)^2]E_{x0}$ .

As it can be seen from the expression 4.1 and 4.2, the transverse dipole  $p_y$  can be treated as being induced not directly by  $E_{x0}$  but the driven electric dipole  $p_x$  and the modulation of spin-orbit coupling:

$$p_y = \frac{\epsilon_{yx}\alpha_{yy}}{(\epsilon_{ii} - \epsilon_m)^2}\alpha_{xx}E_{x0} = \frac{\epsilon_{yx}\alpha_{yy}}{(\epsilon_{ii} - \epsilon_m)^2}p_x \quad (4.3)$$

The polarization state of the reflected electric field in the  $z$  axis can be expressed by the ratio of the two in-plane and orthogonal electric dipole, which can be described as the complex Kerr rotation angle:

$$\Phi = \frac{p_y}{p_x} = \frac{\epsilon_{yx}}{(\epsilon_{ii} - \epsilon_m)^2}\alpha_{yy} = \alpha_{MO}\alpha_{yy} \quad (4.4)$$

The complex Kerr rotation  $\Phi$  is governed by two components: the intrinsic MO property of the given material ( $\alpha_{MO}$ ) and the transversely induced LSP ( $\alpha_{yy}$ ). To be specific, the reflected light is elliptically polarized with Kerr rotation and Kerr ellipticity given by  $\theta = \text{Re}[\Phi]$  and  $\epsilon = \text{Im}[\Phi]$ , respectively. The elliptical polarization is caused by the phase difference  $\Delta\phi$  of the two orthogonally oscillating electric dipole  $p_x$  and  $p_y$ . Since the complex Kerr rotation  $\Phi \propto e^{i\Delta\phi}$ , we get  $\theta \propto \cos\Delta\phi$  and  $\epsilon \propto \sin\Delta\phi$ , where the phase difference  $\Delta\phi = \phi(\alpha_{MO}) - \phi(\alpha_{yy})$ . For a given material, the intrinsic  $\phi(\alpha_{MO})$  is fixed. Then a null point for  $\theta$  when  $\Delta\phi = \pi/2, 3\pi/2, \dots$  and for  $\epsilon$  when  $\Delta\phi = 0, \pi, 2\pi, \dots$  can be respectively achieved at particular wavelengths by tuning the  $\phi(\alpha_{yy})$ . It is also known that both the spectrum and  $\phi(\alpha_{yy})$  of the LSPR can be regulated through engineering the dimensions of the circular nanodisks [90]. Hence, the MO rotation can be affected by the size of the disks (see Fig. 4.8b). This is the explanation of how to obtain the desired polarization state in reflection for the nanodisk structures.

The nanoporous structure is considered to be a structurally complementary system with respect to the nanodisk structure [113]. The magneto-optical activity of both structures can be mirror-imaged to each other according to the MO analogue of Babinet's principle. It has been demonstrated in recent years that plasmon resonance existing in nanopores in thin metallic films exhibits a behavior complementary to that of nanodisks. For two complementary structures (disk and pore) having identical size and inter-distance, the extinction cross section for nanodisk is characterized with a distinguished peak, while a dip for nanopore emerges. Moreover, the MO Kerr rotation and ellipticity spectra of the disks are the mirror image of those of the pores. The reason for these counter behavior in magneto-optical properties for the two structures lies in the common physics. For resonant nan-

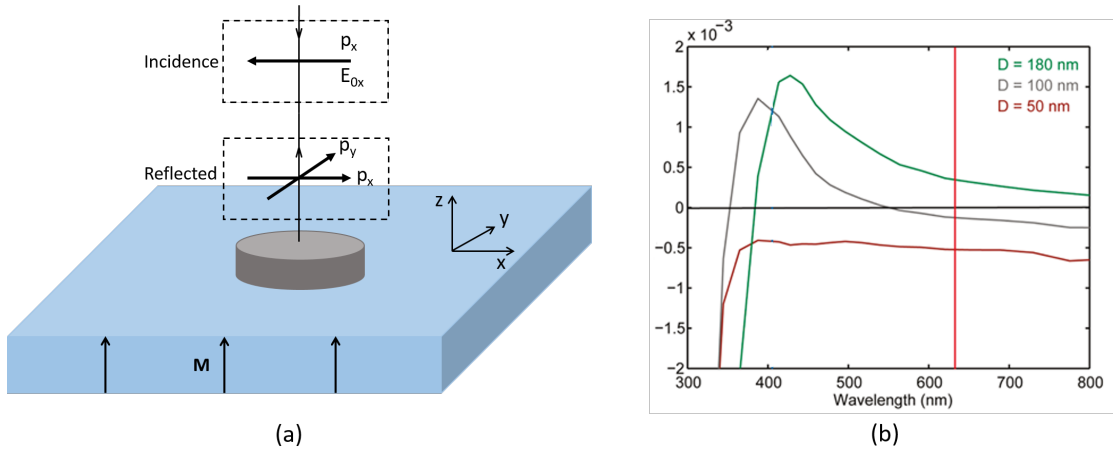


Figure 4.8: (a) Schematic of P-MOKE configuration with normal incidence. (b) Calculated Kerr rotation at 633 nm excitation wavelength for three types of Ni nanodisks with different diameters. Figure (b) extracted from [81].

odisks, the MO effect can be regarded as the applied magnetic field induced rotation of the electric dipole driven by the electric field component of the incident electromagnetic radiation. On the contrary, the nanopores react to the magnetic field component of incident light and generate induction currents surrounding the holes, giving rise to the magnetic dipole. The rotation of magnetic dipole induced by the external magnetic field arises in a way analogous to the electric counterpart of nanodisks.

Thus, it can be inferred from the analogy that the MO response of nanoporous structures can be modified by the size of the pores, that is, there is zero-crossing point in the MO spectra for one structure with fixed nanopore size, and there is also positive and negative MO value for different sizes at the same wavelength. This offers us the explanation for the sign reverse of Kerr loops we observed in the magneto-plasmonic nanoporous structures when the size of nanopores changes. In this way we will be capable of designing the sensing devices exploiting the null point in Kerr rotation spectra, not only exhibiting high sensitivity with unrivaled figure of merits (FOM), but also having advantages of low-cost fabrication, massive functioning surface and high bio-chemical stability.

## 4.4 Conclusion

In this chapter, we studied the magnetoplasmonic structure with an Ag/ITO/CoFeB/ITO/Ag multilayer deposited on a nanoporous AAO substrate. The magnetic, optical and magneto-optical properties of this structure modified by the nanoporosity were investigated. The main results are summarized below:

- The ferromagnetic character brought by the CoFeB layer in this structure was studied, and it was shown that its ferro-magnetism diminished slowly over time.
- The reflectivity measurements were made to obtain the RfS signal. The profiles (number and shift of fringes) of the RfS signal depend on the nanoporous geometry (pore length and diameter). This allows tuning the structure to produce optimal RfS signals with high-intensity fringes of a proper amount, which is useful for improving the sensing performance .
- The magneto-optical Kerr effect was also examined and a reversal of sign of the Kerr loops was discovered. The reversal, which is analogue to the one observed in the structurally complementary magnetic nanodots, is determined by the size of the nanopores. It serves as the principle of designing sensing devices with high sensitivity and theoretically infinite FOM.

It is worth noting that the discovery of Kerr loop inverse is the precursory result for our nanoporous Ag/ITO/CoFeB/ITO/Ag structure. To verify the inversion and to go into more details, the measurements for Kerr rotation spectra are indispensable in the future characterization. Another desirable investigation would be the measurement of reflectivity under magnetic field to evaluate the magnetic effect on the RfS signal.



# Conclusion

## Conclusions

In the present thesis, we were interested in magnetoplasmonic systems with non-conventional magnetic layers and novel nanostructuration, and their abilities to improve the sensitivity in sensing applications. The main goals were to propose different magnetoplasmonic structures based on different kinds of principles through nanostructuration.

In the first chapter, physical principles of three sensing techniques based on SPPs, LSPs and RfS were respectively presented. Then the use of magnetic materials to form magnetoplasmonic structures was presented to explain how to obtain an improvement in the sensitivity by virtue of MO properties. In SPPs-based structures, the change of direction of the magnetic field applied to the magnetic structure induces a shift in the SPP wave vector. Using an alternative magnetic field, a modulation technique can enhance the detection of the plasmon resonance shift. In LSPs-based structures, the plasmonic resonance enhances the MO response of the device by concentrating more electromagnetic field in the MO active materials, which can also be utilized as an efficient method to detect its shift.

In the second chapter, a nanostructured magnetic multilayer with uni-axial anisotropy was employed in the SPPs-based Au/ferromagnet/Au structure. In order to investigate the effects of anisotropic magnetic multilayers on the plasmonic properties, two combinations of anisotropic multilayers FeCo-TbCo<sub>2</sub>-FeCo (3-layer) and FeCo-TbCo<sub>2</sub>-FeCo-TbCo<sub>2</sub>-FeCo (5-layer) were designed. The anisotropic character of the magnetic multilayers was evidenced in the VSM magnetization loops. The results of MOSPR measurements showed that the uni-axial anisotropic properties of the multilayered magnetic materials were clearly reflected on the plasmonic properties of the sensors. There was also an enhancement of the MO activity by using the  $\delta$  signal modulation technique.

The third chapter presented a LSPs-based magnetoplasmonic structure consisting of a combination of Au nanoparticle arrays and continuous magnetic layers. Au nanoparticle arrays were

fabricated by rapid thermal annealing, a simple, efficient and low-cost method to obtain nanoparticles exhibiting a well-defined LSPR peak. Through deposition of ferromagnetic layers on top of Au nanoparticles, a magnetoplasmonic structure was realized. It was proven that a dielectric layer in between Au nanoparticles and ferromagnetic layers was necessary in order to preserve the plasmonic resonance. The results of the plasmonic measurements showed that the resonance is dependent on the thickness of the magnetic layers. This can be used for tuning the MO properties which is useful for the enhancement of sensitivity.

Finally, in the fourth chapter, we studied a hybrid structure with a magnetoplasmonic multi-layer Ag/ITO/CoFeB/ITO/Ag deposited on a nanoporous AAO substrate. The reflectivity spectra were obtained in the form of RfS signal. The profiles (number and shift of fringes) of the RfS signal depend on the nanoporous geometry (pore length and diameter), which allows tuning the structure to produce optimal RfS signals. The magneto-optical Kerr effect was also examined and a reversal of the sign of Kerr loops was evidenced. The reversal is caused by the phases of dipole that is determined by the size of the nanopores. Therefore the nanoporosity was proven to have a tuning effect on the optical and magneto-optical properties, which can be used to design sensing devices with a high sensitivity and a large Factor of Merit (FOM).

### **Perspectives**

The work in this dissertation has induced much ongoing research. As perspectives, there are some characterizations that need to be done in the future for each structure:

For the thin-film structure, another dielectric of a different refractive index needs to be applied on the surface in order to monitor the actual shift of  $\delta$  signal. Thus we will be able to assess the sensitivity along the hard and easy axis.

For the structure of nanoparticles, spectroscopic measurements of Kerr effects need to be done in order to find out the enhancement of MO activity brought by plasmonic resonance of Au nanoparticles. The nanostructured FeCo/TbCo<sub>2</sub> layers will also be tested to see effects of their magnetic anisotropy on the MO activity.

For the nanoporous structure, the spectra of Kerr rotation or ellipticity also need to be characterized in the future by magneto-optical Kerr spectroscopy or magneto-optical ellipsometry, so that we can evaluate the zero crossing point in the spectra, and use it to devise sensors with ultra-high FOM. In addition, the measurement of reflectivity under magnetic field to evaluate the magnetic effect on the RfS signal would also be necessary.

# Bibliography

- [1] G. Armelles, A. Cebollada, A. García-Martín, and M.-U. González, *Advanced Optical Materials* **1**, 10 (2013).
- [2] R. H. Ritchie, *Physical Review* **106**, 874 (1957).
- [3] S. A. Maier, *Plasmonics: fundamentals and applications* (Springer Science & Business Media, 2007).
- [4] E. Ozbay, *science* **311**, 189 (2006).
- [5] D. L. Jeanmaire and R. P. Van Duyne, *Journal of Electroanalytical Chemistry and Interfacial Electrochemistry* **84**, 1 (1977).
- [6] K. Kneipp, M. Moskovits, and H. Kneipp, *Surface-enhanced Raman scattering: physics and applications*, vol. 103 (Springer Science & Business Media, 2006).
- [7] S. Nie and S. R. Emory, *science* **275**, 1102 (1997).
- [8] W. Srituravanich, N. Fang, C. Sun, Q. Luo, and X. Zhang, *Nano letters* **4**, 1085 (2004).
- [9] P. G. Kik, S. A. Maier, and H. A. Atwater, in *Micromachining and Microfabrication* (International Society for Optics and Photonics, 2004), pp. 215–223.
- [10] A. Sundaramurthy, P. J. Schuck, N. R. Conley, D. P. Fromm, G. S. Kino, and W. Moerner, *Nano letters* **6**, 355 (2006).
- [11] E. Petryayeva and U. J. Krull, *Analytica chimica acta* **706**, 8 (2011).
- [12] M. E. Stewart, C. R. Anderton, L. B. Thompson, J. Maria, S. K. Gray, J. A. Rogers, and R. G. Nuzzo, *Chemical reviews* **108**, 494 (2008).
- [13] J. Pitarke, V. Silkin, E. Chulkov, and P. Echenique, *Reports on progress in physics* **70**, 1 (2007).

- [14] J. Homola, *Surface plasmon resonance based sensors*, vol. 4 (Springer Science & Business Media, 2006).
- [15] B. Sepúlveda, L. G. Carrascosa, D. Regatos, M. A. Otte, D. Farina, and L. M. Lechuga, in *SPIE NanoScience+ Engineering* (International Society for Optics and Photonics, 2009), pp. 73970Y–73970Y.
- [16] C. J. Powell and J. B. Swan, *Phys. Rev.* **115**, 869 (1959), URL <http://dx.doi.org/10.1103/PhysRev.115.869>.
- [17] C. J. Powell and J. B. Swan, *Phys. Rev.* **116**, 81 (1959), URL <http://dx.doi.org/10.1103/PhysRev.116.81>.
- [18] E. Kretschmann and H. Raether, *Zeitschrift für Naturforschung A* **23**, 2135 (1968).
- [19] A. Otto, *Zeitschrift für Physik* **216**, 398 (1968).
- [20] C. Nylander, B. Liedberg, and T. Lind, *Sensors and Actuators* **3**, 79 (1982).
- [21] C. E. Jordan, A. G. Frutos, A. J. Thiel, and R. M. Corn, *Analytical Chemistry* **69**, 4939 (1997).
- [22] K. Kihm, S. Cheon, J. Park, H. Kim, J. Lee, I. Kim, and H. Yi, *Optics and lasers in engineering* **50**, 64 (2012).
- [23] K. Matsubara, S. Kawata, and S. Minami, *Applied Optics* **27**, 1160 (1988).
- [24] B. Liedberg, I. Lundström, and E. Stenberg, *Sensors and Actuators B: Chemical* **11**, 63 (1993).
- [25] J. A. Ruemmele, M. S. Golden, Y. Gao, E. M. Cornelius, M. E. Anderson, L. Postelnicu, and R. M. Georgiadis, *Analytical chemistry* **80**, 4752 (2008).
- [26] C. Zhou, W. Jin, Y. Zhang, M. Yang, L. Xiang, Z. Wu, Q. Jin, and Y. Mu, *Analytical Methods* **5**, 2369 (2013).
- [27] R. Jorgenson and S. Yee, *Sensors and Actuators B: Chemical* **12**, 213 (1993).
- [28] P. Vukusic, G. Bryan-Brown, and J. Sambles, *Sensors and Actuators B: Chemical* **8**, 155 (1992).
- [29] C. L. Wong, G. C. K. Chen, X. Li, B. K. Ng, P. Shum, P. Chen, Z. Lin, C. Lin, and M. Olivo, *Biosensors and Bioelectronics* **47**, 545 (2013).
- [30] S. Nelson, K. S. Johnston, and S. S. Yee, *Sensors and Actuators B: Chemical* **35**, 187 (1996).

- [31] C. Wong, H. Ho, Y. Suen, S. Kong, Q. Chen, W. Yuan, and S. Wu, *Biosensors and Bioelectronics* **24**, 606 (2008).
- [32] A. Kruchinin and Y. G. Vlasov, *Sensors and Actuators B: Chemical* **30**, 77 (1996).
- [33] M. Piliarik and J. Homola, *Sensors and Actuators B: Chemical* **134**, 353 (2008).
- [34] C.-Y. Han and C.-W. Luo, *Optics Communications* **294**, 8 (2013).
- [35] B. Liedberg, C. Nylander, and I. Lunström, *Sensors and actuators* **4**, 299 (1983).
- [36] R. Kooyman, H. Kolkman, J. Van Gent, and J. Greve, *Analytica Chimica Acta* **213**, 35 (1988).
- [37] E. Hutter and J. H. Fendler, *Advanced Materials* **16**, 1685 (2004).
- [38] T. Hutter, S. R. Elliott, and S. Mahajan, *Nanotechnology* **24**, 035201 (2013).
- [39] C. F. Bohren and D. R. Huffman, *Absorption and scattering of light by small particles* (John Wiley & Sons, 2008).
- [40] G. A. Ozin, A. C. Arsenault, and L. Cademartiri, *Nanochemistry: a chemical approach to nanomaterials* (Royal Society of Chemistry, 2009).
- [41] P. K. Jain and M. A. El-Sayed, *Chemical Physics Letters* **487**, 153 (2010).
- [42] S. Link and M. A. El-Sayed, *The Journal of Physical Chemistry B* **103**, 8410 (1999).
- [43] L. M. Liz-Marzán, *Langmuir* **22**, 32 (2006).
- [44] X. Lu, M. Rycenga, S. E. Skrabalak, B. Wiley, and Y. Xia, *Annual review of physical chemistry* **60**, 167 (2009).
- [45] J. Pérez-Juste, I. Pastoriza-Santos, L. M. Liz-Marzán, and P. Mulvaney, *Coordination Chemistry Reviews* **249**, 1870 (2005), URL <http://www.sciencedirect.com/science/article/pii/S0010854505000287>.
- [46] K. A. Willets and R. P. Van Duyne, *Annu. Rev. Phys. Chem.* **58**, 267 (2007).
- [47] L. S. Jung, C. T. Campbell, T. M. Chinowsky, M. N. Mar, and S. S. Yee, *Langmuir* **14**, 5636 (1998).
- [48] B. Lee, S. Roh, and J. Park, *Optical Fiber Technology* **15**, 209 (2009).
- [49] M. Svedendahl, S. Chen, A. Dmitriev, and M. Kall, *Nano letters* **9**, 4428 (2009).
- [50] Y.-J. Oh, S.-G. Park, M.-H. Kang, J.-H. Choi, Y. Nam, and K.-H. Jeong, *Small* **7**, 184 (2011).

- [51] G. Das, F. Mecarini, F. De Angelis, M. Prasciolu, C. Liberale, M. Patrini, and E. Di Fabrizio, *Microelectronic Engineering* **85**, 1282 (2008).
- [52] T. Chung, S.-Y. Lee, E. Y. Song, H. Chun, and B. Lee, *Sensors* **11**, 10907 (2011).
- [53] R. Bukasov, T. A. Ali, P. Nordlander, and J. S. Shumaker-Parry, *Acs Nano* **4**, 6639 (2010).
- [54] P. Hanarp, M. Käll, and D. S. Sutherland, *The Journal of Physical Chemistry B* **107**, 5768 (2003).
- [55] F. Hao, C. L. Nehl, J. H. Hafner, and P. Nordlander, *Nano letters* **7**, 729 (2007).
- [56] J. B. Lassiter, J. Aizpurua, L. I. Hernandez, D. W. Brandl, I. Romero, S. Lal, J. H. Hafner, P. Nordlander, and N. J. Halas, *Nano letters* **8**, 1212 (2008).
- [57] S. L. Teo, V. K. Lin, R. Marty, N. Large, E. A. Llado, A. Arbouet, C. Girard, J. Aizpurua, S. Tripathy, and A. Mlayah, *Optics express* **18**, 22271 (2010).
- [58] W. Kubo and S. Fujikawa, *Nano letters* **11**, 8 (2010).
- [59] D. Regatos, D. Fariña, A. Calle, A. Cebollada, B. Sepúlveda, G. Armelles, and L. M. Lechuga, *Journal of Applied Physics* **108**, 054502 (2010).
- [60] T. Nikolajsen, K. Leosson, and S. I. Bozhevolnyi, *Applied Physics Letters* **85**, 5833 (2004), URL <http://scitation.aip.org/content/aip/journal/apl/85/24/10.1063/1.1835997>.
- [61] M. J. Dicken, L. A. Sweatlock, D. Pacifici, H. J. Lezec, K. Bhattacharya, and H. A. Atwater, *Nano Letters* **8**, 4048 (2008), pMID: 18847247, <http://dx.doi.org/10.1021/nl802981q>, URL <http://dx.doi.org/10.1021/nl802981q>.
- [62] D. Pacifici, H. J. Lezec, and H. A. Atwater, *Nature photonics* **1**, 402 (2007).
- [63] A. Hubert and R. Schäfer, *Magnetic domains: the analysis of magnetic microstructures* (Springer Science & Business Media, 2008).
- [64] V. V. Temnov, G. Armelles, U. Woggon, D. Guzatov, A. Cebollada, A. Garcia-Martin, J.-M. Garcia-Martin, T. Thomay, A. Leitenstorfer, and R. Bratschitsch, *Nature Photonics* **4**, 107 (2010).
- [65] V. Belotelov, I. Akimov, M. Pohl, V. Kotov, S. Kasture, A. Vengurlekar, A. V. Gopal, D. Yakovlev, A. Zvezdin, and M. Bayer, *Nature Nanotechnology* **6**, 370 (2011).
- [66] V. V. Temnov, *Nature Photonics* **6**, 728 (2012).

- [67] K. Chiu and J. Quinn, *Physical Review B* **5**, 4707 (1972).
- [68] A. Hartstein, E. Burstein, A. Maradudin, R. Brewer, and R. Wallis, *Journal of Physics C: Solid State Physics* **6**, 1266 (1973).
- [69] R. Wallis, J. Brion, E. Burstein, and A. Hartstein, *Physical Review B* **9**, 3424 (1974).
- [70] S. Schnatterly, *Physical Review* **183**, 664 (1969).
- [71] P. Haefner, E. Luck, and E. Mohler, *physica status solidi (b)* **185**, 289 (1994).
- [72] J. B. González-Díaz, B. Sepúlveda, A. García-Martín, and G. Armelles, *Applied Physics Letters* **97**, 043114 (2010).
- [73] W. L. Barnes, A. Dereux, and T. W. Ebbesen, *Nature* **424**, 824 (2003).
- [74] A. V. Zayats and I. I. Smolyaninov, *Journal of Optics A: Pure and Applied Optics* **5**, S16 (2003).
- [75] B. Sepúlveda, A. Calle, L. M. Lechuga, and G. Armelles, *Optics letters* **31**, 1085 (2006).
- [76] K. Kämpf, S. Kübler, F. W. Herberg, and A. Ehresmann, *Journal of Applied Physics* **112**, 034505 (2012).
- [77] J. B. González-Díaz, A. García-Martín, G. Armelles, J. M. García-Martín, C. Clavero, A. Cebollada, R. Lukaszew, J. Skuza, D. Kumah, and R. Clarke, *Physical Review B* **76**, 153402 (2007).
- [78] C. Clavero, K. Yang, J. Skuza, and R. Lukaszew, *Optics express* **18**, 7743 (2010).
- [79] S. David, C. Polonschii, C. Luculescu, M. Gheorghiu, S. Gáspár, and E. Gheorghiu, *Biosensors and Bioelectronics* **63**, 525 (2015).
- [80] J. C. Banthi, D. Meneses-Rodríguez, F. García, M. U. González, A. García-Martín, A. Cebollada, and G. Armelles, *Advanced Materials* **24**, OP36 (2012).
- [81] V. Bonanni, S. Bonetti, T. Pakizeh, Z. Pirzadeh, J. Chen, J. Nogués, P. Vavassori, R. Hillenbrand, J. Åkerman, and A. Dmitriev, *Nano letters* **11**, 5333 (2011).
- [82] B. C. Stipe, T. C. Strand, C. C. Poon, H. Balamane, T. D. Boone, J. A. Katine, J.-L. Li, V. Rawat, H. Nemoto, A. Hirotsune, et al., *Nature Photonics* **4**, 484 (2010).
- [83] P. Hui and D. Stroud, *Applied physics letters* **50**, 950 (1987).
- [84] T. Xia, P. Hui, and D. Stroud, *Journal of Applied Physics* **67**, 2736 (1990).

- [85] J. B. González-Díaz, A. García-Martín, G. Armelles, D. Navas, M. Vázquez, K. Nielsch, R. B. Wehrspohn, and U. Gösele, *Advanced Materials* **19**, 2643 (2007).
- [86] J. Chen, P. Albella, Z. Pirzadeh, P. Alonso-González, F. Huth, S. Bonetti, V. Bonanni, J. Åkerman, J. Nogués, P. Vavassori, et al., *Small* **7**, 2341 (2011).
- [87] J. B. González-Díaz, A. García-Martín, J. M. García-Martín, A. Cebollada, G. Armelles, B. Sepúlveda, Y. Alaverdyan, and M. Käll, *Small* **4**, 202 (2008).
- [88] D. Meneses-Rodríguez, E. Ferreira-Vila, P. Prieto, J. Anguita, M. U. González, J. M. García-Martín, A. Cebollada, A. García-Martín, and G. Armelles, *Small* **7**, 3317 (2011).
- [89] P. Bertrand, C. Hermann, G. Lampel, J. Peretti, and V. Safarov, *Physical Review B* **64**, 235421 (2001).
- [90] N. Maccaferri, A. Berger, S. Bonetti, V. Bonanni, M. Kataja, Q. H. Qin, S. Van Dijken, Z. Pirzadeh, A. Dmitriev, J. Nogués, et al., *Physical review letters* **111**, 167401 (2013).
- [91] K. Lodewijks, N. Maccaferri, T. Pakizeh, R. K. Dumas, I. Zubritskaya, J. Åkerman, P. Vavassori, and A. Dmitriev, *Nano letters* **14**, 7207 (2014).
- [92] O. Meskini, A. Abdelghani, A. Tlili, R. Mgaïeth, N. Jaffrezic-Renault, and C. Martelet, *Talanta* **71**, 1430 (2007).
- [93] M. P. Schwartz, S. D. Alvarez, and M. J. Sailor, *Analytical chemistry* **79**, 327 (2007).
- [94] R. C. Alkire, Y. Gogotsi, P. Simon, and A. Eftekhari, *Nanostructured materials in electrochemistry* (John Wiley & Sons, 2008).
- [95] A. Santos, T. Kumeria, and D. Losic, *TrAC Trends in Analytical Chemistry* **44**, 25 (2013).
- [96] S. Pan and L. J. Rothberg, *Nano letters* **3**, 811 (2003).
- [97] S. D. Alvarez, C.-P. Li, C. E. Chiang, I. K. Schuller, and M. J. Sailor, *Acs Nano* **3**, 3301 (2009).
- [98] S.-H. Yeom, O.-G. Kim, B.-H. Kang, K.-J. Kim, H. Yuan, D.-H. Kwon, H.-R. Kim, and S.-W. Kang, *Optics express* **19**, 22882 (2011).
- [99] Y. Song, W. Yin, Y.-H. Wang, J.-P. Zhang, Y. Wang, R. Wang, J. Han, W. Wang, S. V. Nair, and H. E. Ruda, *Scientific reports* **4**, 4991 (2014).
- [100] S. Kübler, N. Möglich, and A. Ehresmann, *Journal of Applied Physics* **116**, 064502 (2014).

- 
- [101] H. Le Gall, J. B. Youssef, F. Socha, N. Tiercelin, V. Preobrazhensky, and P. Pernod, *Journal of Applied Physics* **87**, 5783 (2000).
- [102] N. Tiercelin, J. B. Youssef, V. Preobrazhensky, P. Pernod, and H. Le Gall, *Journal of magnetism and magnetic materials* **249**, 519 (2002).
- [103] Y. Dusch, Theses, Ecole Centrale de Lille (2011), URL <https://tel.archives-ouvertes.fr/tel-00697174>.
- [104] P. B. Johnson and R.-W. Christy, *Physical review B* **6**, 4370 (1972).
- [105] P. Johnson and R. Christy, *Physical Review B* **9**, 5056 (1974).
- [106] N. Tiercelin, V. Preobrazhensky, P. Pernod, H. Le Gall, and J. B. Youssef, *Journal of magnetism and magnetic materials* **210**, 302 (2000).
- [107] N. Tiercelin, V. Preobrazhensky, P. Pernod, and A. Ostaschenko, *Applied Physics Letters* **92**, 062904 (2008).
- [108] N. Tiercelin, A. Talbi, V. Preobrazhensky, P. Pernod, V. Mortet, K. Haenen, and A. Soltani, *Applied Physics Letters* **93**, 162902 (2008).
- [109] A. Klimov, Y. Ignatov, N. Tiercelin, V. Preobrazhensky, P. Pernod, and S. Nikitov, *Journal of Applied Physics* **107**, 093916 (2010).
- [110] B. Sepúlveda, J. B. González-Díaz, A. García-Martín, L. M. Lechuga, and G. Armelles, *Physical review letters* **104**, 147401 (2010).
- [111] G. Armelles, J. B. González-Díaz, A. García-Martín, J. M. García-Martín, A. Cebollada, M. U. González, S. Acimovic, J. Cesario, R. Quidant, and G. Badenes, *Optics express* **16**, 16104 (2008).
- [112] T. Kumeria and D. Losic, *Nanoscale research letters* **7**, 1 (2012).
- [113] G. Armelles, B. Caballero, A. Cebollada, A. Garcia-Martin, and D. Meneses-Rodríguez, *Nano letters* **15**, 2045 (2015).



# Contrôle des propriétés magnéto-optiques de systèmes magnétoplasmoniques grâce à la nanostructuration

## RESUME

Ce travail de thèse porte sur le contrôle des propriétés de trois systèmes magnéto-plasmoniques grâce à différents types de nanostructuration. Ces structures sont basées respectivement sur la Propagation de Plasmons de Surface (SPP), les Plasmons de Surface Localisés (LSP) et la spectroscopie d'interférences en réflexion (RfS). La manipulation des propriétés magnéto-optiques (MO) pour une utilisation dans les biocapteurs et pour l'amélioration de la sensibilité est discutée.

Le premier système est une structure SPP en couche mince constituée de couches de métaux nobles et d'un matériau magnétique de type multicouche présentant une anisotropie uni-axiale contrôlée. Les propriétés d'anisotropie de la couche magnétique se reflètent clairement sur les propriétés plasmoniques du système. Une amélioration de l'activité magnéto-optique peut être mise à profit pour améliorer la sensibilité de capteurs basés sur cette structure.

Le second dispositif est basé sur une structure LSP constituée de nanoparticules d'or et d'une couche magnétique continue. Il est démontré qu'une couche diélectrique entre la couche magnétique et les nanoparticules d'or est indispensable pour préserver la résonance plasmonique. L'épaisseur de la couche magnétique a un effet sur cette dernière qui peut en principe être mise à profit pour influencer sur l'activité magnéto-optique.

La troisième approche est une structure hybride RfS composée d'un système multicouche magnéto-plasmonique Ag/ITO/CoFeB/ITO/Ag déposé sur un substrat nanoporeux d'oxyde d'aluminium anodique (AAO). Le signal RfS dépend de la taille et de la longueur des nanopores. Le diamètre des nanopores affecte également la réponse magnéto-optique en réflexion en générant une inversion du signe des cycles d'aimantation mesurés par effet Kerr.

**Mots-clefs :** Nanostructuration, Magnétoplasmonique, Anisotropie Magnétique, Nanoparticules, Nanopores, SPP, LSP, RfS, Effet Kerr magnéto-optique

## Tailoring magneto-optical properties of magnetoplasmonic systems through nanostructuration

### ABSTRACT

This PhD dissertation deals with the tuning of the properties of three different magnetoplasmonic systems by using different nanostructuration schemes. They are structures based on Surface Propagating Plasmons (SPP), Localized Surface Plasmons (LSP) and reflective interference spectroscopy (RfS), respectively. The manipulation of the magneto-optic (MO) properties to be used in biosensors and to improve the sensitivity is discussed.

The first system is a thin-film SPP structure consisting of magnetic and noble metal layers, where the magnetic part is nanostructured multilayers with controlled uni-axial anisotropy. The anisotropic properties of the magnetic layer are clearly reflected on the plasmonic properties of the system. An enhancement in the MO activity can be used to improve the sensitivity of the sensors based on this structure.

The second system is a LSP-based magnetoplasmonic structure consisting of gold nanoparticle arrays and continuous magnetic layers. It is demonstrated that a dielectric layer in between the gold nanoparticles and magnetic layers is compulsory in order to preserve the plasmonic resonance. The thickness of magnetic layers has an effect on the latter which can, in principle, be further used to tune the MO activity.

The third system is a hybrid RfS structure obtained with a magnetoplasmonic multilayer Ag/ITO/CoFeB/ITO/Ag deposited on a nanoporous Anodic Aluminium Oxide (AAO) substrate. The RfS signal depends on both the size and the length of the nanopores. The diameter of the nanopores also affects the MO response by generating a reversal in the sign of the Kerr loops.

**Key words:** Nanostructuration, Magnetoplasmonics, Magnetic anisotropy, Nanoparticles, Nanopores, SPP, LSP, RfS, Magneto-optical Kerr effect